



SPACE SCIENCE AND ENGINEERING CENTER

UNIVERSITY of WISCONSIN – MADISON
1225 West Dayton Street
Madison, Wisconsin 53706-1695

21 May 2001

Dr. Donald K. West
Code 681.0
NASA
Goddard Space Flight Center
Greenbelt, VA 20771

THE SCHWERDTFEGGER LIBRARY
1225 W. Dayton Street
Madison, WI 53706

Re: Annual Progress Report for NAG5-3524

Please find enclosed the annual technical report for the referenced grant entitled "Studies of the Hot Interstellar Medium and Halo of our Galaxy: Spatial Structure and Spectral Characteristics of the Low Energy X-ray Background". The principal investigator is Wilton T. Sanders.

We have also enclosed a budget for the fifth year of funding.

If you have any concerns or questions, please call me at (608)262-0985. Thank you for your continued support and assistance.

Sincerely,

John P. Roberts
Executive Director-Administration

Enc. (2)

Cc: Grants
ONRRO
144-GC54
4991
W. Sanders

k:\admin\4991rpt1.doc

| | | | |
|--------------------|----------------|-------------|----------------|
| Executive Director | (608) 262-0544 | Fax | (608) 262-5974 |
| Business Services | (608) 263-3037 | Information | (608) 263-6750 |

THE SCHWERDTFEGER LIBRARY
1225 W. Dayton Street
Madison, WI 53706

Annual Progress Report
for the period
15 May 2000 - 14 May 2001

for NASA Grant
NAG5-3524

Studies of the Hot Interstellar Medium and Halo of our Galaxy:
Spatial Structure and Spectral Characteristics of the Low Energy X-ray Background

Wilton T. Sanders

under NASA's Long Term Space Astrophysics Program (LTSA)

1. Project Overview

The goal of this project is to extend previous studies of the spatial structure and spectral characteristics of the X-ray background in the energy range $\sim 70 - 1000$ eV. The soft X-ray background originates from hot phases of the interstellar medium and the Galactic halo. This hot matter is not uniformly distributed, but exhibits quite different intensities and spectral ratios in different directions on the sky.

We wish to constrain the distances to the various hot interstellar regions, and to constrain their spectral emission parameters. These are necessary steps toward understanding the origin and evolution of the hot phases of the interstellar medium and their role in the evolution of our galaxy. The program uses data primarily from the ROSAT, DXS, ASCA and Chandra orbiting missions, and secondarily from the EUVE and ALEXIS missions. In addition, data are used from University of Wisconsin sounding rocket flights, and from the ground-based WIYN telescope.

2. Progress During Year Four

The paper with Steve Snowden, M. J. Freyberg, & K. D. Kuntz (Snowden et al. 2000) on a catalog of shadows in the 1/4 keV soft X-ray diffuse background was published in the May 2000 issue of the Astrophysical Journal Supplements. These shadows were identified by comparing ROSAT all-sky survey maps to DIRBE-corrected IRAS 100-micron maps. A copy of the published paper accompanies this report.

The paper presenting the DXS spectra and summarizing the analysis to date was modified according to the comments and suggestions of the referee's report from the Astrophysical Journal, and resubmitted to the Journal. Unfortunately, this process took much longer than expected, but it eventually converged and the paper was accepted for publication in the 20 June 2001 issue of the ApJ (Sanders et al. 2001). A copy of the revised manuscript of the paper accompanies this report.

Massimiliano Galeazzi has joined the effort with Snowden and Jay Lockman on analyzing the ROSAT XRT/PSPC data towards the cloud complex in Ursa Major that shows X-ray shadows. We have reduced a number of the pointed ROSAT observations and two interferometric H I observations towards those clouds. The results of the comparison of these data are being written up in year five.

Work with Keivan Stassun to reduce B, V, and R band images taken on the Kitt Peak 0.9-m telescope in January 1998 of an X-ray shadowing cloud in Ursa Major again has not progressed as I thought. The goal is to select stars suitable for use with the WIYN telescope multi-object spectrograph (MOS) to look for interstellar absorption lines that would constrain the distance to the cloud. Keivan did not immediately have more time as a post-doc but has recently resumed work on this project.

I worked further with Dan McCammon to help with his analysis of the third XQC sounding rocket data. This is a micro-calorimeter observation of the diffuse X-ray background in the 0.1 - 3 keV range from a 30° small circle around galactic coordinates $(l, b) \sim (90^\circ, +60^\circ)$. It clearly shows the O VII line, which can be used with the measurement of the O VIII line to constrain the temperature of the emitting plasma. These data do not show evidence for iron lines, however. A paper will be submitted to the Astrophysical Journal shortly.

I received data from the ACIS detector on the Chandra X-ray Observatory to study diffuse emission from face-on galaxies. NGC 3184 was observed for 40 ks in January 2000. An additional 20 ks was observed in 2000 March because a supernova occurred in this galaxy

in late 1999. Working with Mike Juda and later Mark Quigley, a preliminary analysis was completed in time for the November 2000 HEAD meeting (Juda et al. 2000, Sanders et al. 2000). We found both a general diffuse glow from the galaxy as well as a number of sources, but we have not yet determined if any of the sources are diffuse regions analogous to the Local Bubble. I used observing time on the WIYN telescope in April 2001 to obtain arc-second images of NGC 3184 with B and R broadband filters, and in the H α line and continuum. These images will be used to determine if regions of diffuse X-ray emission correlate with early-type stars or with H II regions.

3. Research Plans for Year Five

Research plans for the coming year continue to be essentially as outlined in the original proposal and described in last year's progress report. The primary activities are to focus on the ROSAT analyses, the DXS analysis, and the Chandra analysis while maintaining a modest level of effort in the ASCA analysis, and the WIYN observations. The major change is that the time originally planned for the analysis of CUBIC and Astro-E data will be used for DXS and AXAF data analysis, with small amounts distributed among the other space-based observation sets.

3.1 DXS (30%)

The analysis of DXS data will continue for determining useful spectral parameters for the diffuse background emission from the Vela and Monogem supernova remnants (Morgenthaler et al. 2001, in preparation). I will be working with D. Liedahl and R. Edgar to continue development of improved line emission models, incorporating new and improved calculations of Mg, Si, and S L-shell lines by Liedahl. The third DXS paper will deal specifically with fits using these new line calculations (Edgar et al. 2001, in preparation). We will also be collaborating with Randall Smith to fit DXS data to his models of 10^6 -year-old blast waves, which also incorporate reheated cavities, dust and varying thermal conduction. These models must be updated to include the new line calculations from Liedahl. We will also perform simultaneous fits of DXS data with overlapping ROSAT data and XQC data using the improved models when they are available.

3.2 ROSAT (30%)

I will continue the existing collaborations for this work with Jay Lockman and Steve Snowden. We will continue comparisons of ROSAT XRT/PSPC data with existing IRAS 100 micron data, H I 21-cm survey data, and the more recent interferometric data on selected clouds. The goal is to quantify how the X-ray background intensity features are related to cloud structures. The initial focus is the clouds in the Ursa Major region, but we will also analyze other clouds with shadows, and obtain upper limits to clouds with no shadows.

3.3 AXAF (20%)

I anticipate that the analysis of the Chandra data sets and the WIYN images of NGC 3184 will be completed during the upcoming year.

3.4 ASCA (8%)

In collaboration with Massimiliano Galeazzi and K. Gendreau, I plan to use ASCA data from selected deep pointings around the sky to better understand the ~ 400 eV - 1000 eV diffuse background emission. For those ASCA data that overlap ROSAT data and XQC

data, simultaneous fits will be analyzed. Reconciling the apparent differences between the diffuse background spectral parameters found by ASCA and ROSAT (Chen, Fabian, and Gendreau 1997, Miyaji et al. 1998) those found by XQC is especially critical for understanding the extragalactic background. Both ROSAT and ASCA have quite extensive archives of deep pointings, so that many targets are available for this work.

3.5 WIYN (5%)

I plan to continue to use the WIYN telescope, with its multi-object spectrograph (MOS), to determine distances to the Ursa Major low velocity cloud. I will continue existing collaborations for this work with B. Wakker and B. Savage.

3.6 Sounding Rockets (5%)

In collaboration with R. Smith, M. Juda, J. Bloch, R. J. Edgar, and D. McCammon, I plan to use existing Wisconsin sounding rocket data to perform pulse height fits to boron-window and beryllium-filter data. These data were previously analyzed only through their broad-band count rates. We will also perform simultaneous fits to overlapping DXS data. A fair amount of reprocessing of 10 - 15 year old sounding rocket data will be necessary for this. These old data will be read onto disk and reformatted so that photon extraction routines can create photon event files which can be sorted and binned for use by XSPEC.

3.7 ALEXIS/EUVE/CHIPS (2%)

I will continue my existing collaboration with J. Bloch for the ALEXIS work. A draft first ALEXIS paper has been produced without my involvement, but Jeff and I are planning to work together on a second paper. I also have had and will continue to have conversations with Mark Hurwitz and Randy Kimble about using DXS results to constrain models of the diffuse background that may be useful for analysis of the CHIPS data.

4. References

- Chen, L.-W., Fabian, A. C., Gendreau, K. C. 1997, MNRAS, 285, 449
Galeazzi, M. et al. 2000, AAS/HEAD, 32, 3227
Juda, M., Sanders, W. T., McCammon, D., & Cui, W. 2000, AAS/HEAD, 32, 1506
Miyaji, T., Ishisaki, Y., Ogasaka, Y., Ueda, Y., Freyberg, M. J., Hasinger, G., & Tanaka, T. 1998, AA, 334, L13
Sanders, W. T., Cui, W., Juda, M., & McCammon, D. 2000, AAS/HEAD, 32, 3224
Sanders, W. T., Edgar, R. J., Kraushaar, W. L., McCammon, D., Morgenthaler, J. P. 2001, "Spectra of the 1/4 keV X-ray Diffuse Background from the Diffuse X-ray Spectrometer Experiment" ApJ, 554, in press
Snowden, S. L., Kuntz, K. D., Freyberg, M. J., & Sanders, W. T. 2000, "A Catalog of Soft X-ray Shadows, and more Contemplation of the 1/4 keV Background" ApJS, 128, 171

Budget
 NAG5-3524
 NASA - Year 5
 15 May 2001 - 14 May 2002

| | <u>Hours</u> | <u>Rate</u> | <u>Cost</u> |
|--|--------------|-------------|-------------------------|
| I. Labor and Fringe Benefits | | | |
| a) PI - W. Sanders | 1,220 | \$65.77 | \$ 80,239 |
| b) Res. Associate - J. Morgenthaler | 360 | 28.91 | <u>10,408</u> |
| Subtotal | | | \$90,647 |
| II. Travel | | | |
| a) 1 trip/Pasadena/5days/AAS mtg./Jun 2001 | | | 1,500 |
| b) 1 trip/San Diego/5days/SPIE Mtg./Jul/Aug 2001 | | | 1,200 |
| c) 1trip/Washington/5days/AAS mtg./Jan. 2002 | | | <u>1,103</u> |
| Subtotal | | | 3,803 |
| III. Publications | | | |
| a) Paper 1 @10pages @\$115/page | | | 1,150 |
| b) Paper 2 @10 pages @\$115/page | | | 1,150 |
| c) Paper 3 @10 pages @\$115/page | | | <u>1,150</u> |
| Subtotal | | | 3,450 |
| IV. Computer Services | | | 1,400 |
| V. Materials | | | 700 |
| VI. University Indirect Cost at 44% | | | <u>44,000</u> |
| TOTAL | | | <u><u>\$144,000</u></u> |

k:/admin:prop850.xls

A CATALOG OF SOFT X-RAY SHADOWS, AND MORE CONTEMPLATION OF THE $\frac{1}{4}$ keV BACKGROUND

S. L. SNOWDEN,^{1,2,3} M. J. FREYBERG,² K. D. KUNTZ,⁴ AND W. T. SANDERS⁵

Received 1999 July 21; accepted 1999 December 16

ABSTRACT

This paper presents a catalog of shadows in the $\frac{1}{4}$ keV soft X-ray diffuse background (SXR) that were identified by a comparison between *ROSAT* All-Sky Survey maps and DIRBE-corrected *IRAS* 100 μ m maps. These “shadows” are the negative correlations between the surface brightness of the SXR and the column density of the Galactic interstellar medium (ISM) over limited angular regions (a few degrees in extent). We have compiled an extensive but not exhaustive set of 378 shadows in the polar regions of the Galaxy ($|b| \gtrsim 20^\circ$) and determined their foreground and background X-ray intensities (relative to the absorbing features) and the respective hardness ratios of that emission. The portion of the sky that was examined to find these shadows was restricted in general to regions where the minimum column density is $\lesssim 4 \times 10^{20}$ H cm⁻², i.e., relatively high Galactic latitudes, and to regions away from distinct extended features in the SXR such as supernova remnants and superbubbles. The results for the foreground intensities agree well with the recent results of a general analysis of the local $\frac{1}{4}$ keV emission, while the background intensities show additional, but not unexpected scatter. The results also confirm the existence of a gradient in the hardness of the local $\frac{1}{4}$ keV emission along a Galactic center/anticenter axis with a temperature that varies from $10^{6.13}$ to $10^{6.02}$ K, respectively. The average temperature of the foreground component from this analysis is $10^{6.08}$ K, compared to $10^{6.06}$ K in the previous analysis. Likewise, the average temperature for the distant component for the current and previous analyses are $10^{6.00}$ and $10^{6.02}$ K, respectively. Finally, the results for the $\frac{1}{4}$ keV halo emission are compared to the observed fluxes at $\frac{3}{4}$ keV, where the lack of correlation suggests that the Galactic halo’s $\frac{1}{4}$ and $\frac{3}{4}$ keV fluxes are likely produced by separate emission regions.

Subject headings: catalogs — Galaxy: general — ISM: general — X-rays: galaxies — X-rays: general

1. INTRODUCTION

A negative correlation between the column density distribution of a Galactic H I feature and the surface brightness of the $\frac{1}{4}$ keV soft X-ray diffuse background (SXR), a “shadow,” provides a mechanism for determining the location along the line of sight of X-ray-emitting plasmas relative to the X-ray-absorbing H I. The fundamental result of a shadowing observation is the separation of the observed X-ray flux into foreground and background components relative to the shadowing object. An “object” in this case can be either a local column-density enhancement (i.e., cloud) or a local minimum in the Galactic H I column density. With the additional information of the distance to the shadowing object, which can be determined using interstellar absorption line measurements toward stars with a range of known distances, constraints can be placed on the locations of the emission components. If a number of shadowing observations can be combined, then it becomes possible to create a three-dimensional map of the distribution of both the X-ray-emitting and -absorbing material. This process becomes particularly effective when the results are compared with the extensive mappings of the distribution of neutral material in the solar neighborhood that can be

found in the literature (e.g., Frisch & York 1983; Paresce 1984; Welsh et al. 1994; Sfeir et al. 1999).

Shadows in the general SXR (i.e., away from discrete emission features such as supernova remnants) were first unambiguously detected using the *ROSAT* observatory (Snowden et al. 1991; Burrows & Mendenhall 1991). The continuing study of such shadows has provided crucial information about the soft X-ray emission from the Galactic halo and from the Local Hot Bubble (LHB), an irregularly shaped region of $\sim 10^6$ K plasma that extends ~ 50 – 150 pc from the Sun in all directions (Cox & Snowden 1986; Cox & Reynolds 1987; Snowden et al. 1990a, 1998). For example, the relationship between the $\frac{1}{4}$ keV SXR surface brightness and the H I column density has been examined recently for a number of regions of the sky, both large and small. *ROSAT* All-Sky Survey data were used to study several regions of rather limited extent (Kerp et al. 1996, 1999), a large region in Ursa Major (Snowden et al. 1994a), the M complex of high-velocity clouds (Herbstmeier et al. 1995), the Draco Nebula (Snowden et al. 1991; Moritz et al. 1998), the Eridanus enhancement (Snowden et al. 1995a), as well as the whole sky (Wang 1997; Snowden et al. 1998; Pietz et al. 1998). *ROSAT* pointed observations were used to study the Draco Nebula (Burrows & Mendenhall 1991), MBM 12 (Snowden, McCammon, & Verter 1993), several distinct clouds (Wang & Yu 1995; Kuntz, Snowden, & Verter 1997), a region of Ursa Major (Barber & Warwick 1996), and a region of Eridanus (Guo et al. 1995).

With the aim of providing a tool with which to further studies of the small-scale geometry of the local interstellar medium and to provide information on $\frac{1}{4}$ keV emission from the Galactic halo, this paper presents a catalog of 378

¹ Code 662, NASA/Goddard Space Flight Center, Greenbelt, MD 20771.

² Max-Planck-Institut für Extraterrestrische Physik, D-85740 Garching, Germany.

³ Universities Space Research Association.

⁴ Department of Astronomy, University of Maryland, College Park, MD 20742.

⁵ Department of Physics, University of Wisconsin—Madison, 1150 University Avenue, Madison, WI 53706.

absorption/emission features in the $\frac{1}{4}$ keV soft X-ray background derived from the *ROSAT* All-Sky Survey (RASS). This analysis improves upon the general results reported in Snowden et al. (1998, hereafter Paper I) by selecting regions of the sky most likely to provide statistically significant results. These are regions with variations in absorption greater than one optical depth over a solid angle of typically $\lesssim 30$ deg² in directions of relatively low average column densities. The derived results are therefore more accurate for the sampled regions of the sky than the smoothed results of Paper I. In addition, we have slightly improved upon the analysis technique of Paper I.

The data used in this analysis are discussed in § 2, the analysis itself is described in § 3, and the results and discussion are presented in § 4. Section 5 presents the conclusions of this paper.

2. DATA

For the analysis presented here, we have used the RASS high-resolution maps of the $\frac{1}{4}$ and $\frac{3}{4}$ keV diffuse X-ray background presented in Snowden et al. (1997) and the DIRBE-corrected *IRAS* 100 μ m maps of Schlegel, Finkbeiner, & Davis (1998) scaled to represent the column density of Galactic neutral hydrogen. These are the same basic data sets (with the addition of the $\frac{3}{4}$ keV data) that were used in Paper I.

2.1. X-Ray Data

As described in detail in Snowden et al. (1995b; 1997), the X-ray data have been cleaned of periods of anomalously high noncosmic background, have had residual noncosmic background contributions subtracted (scattered solar X-rays [Snowden & Freyberg 1993], particle background [Snowden et al. 1992; Plucinsky et al. 1993], and long-term enhancements [Snowden et al. 1994b]), are exposure corrected, and have had bright point sources removed. The maps cover $\sim 98\%$ of the sky with roughly 10^6 $12' \times 12'$ pixels, and consist of count rate and count-rate uncertainty pairs in six bands. In this paper we use data from the R1 and R2 bands, and the summed R12 band ($\frac{1}{4}$ keV) and R45 band ($\frac{3}{4}$ keV). The R12 band data are formed by summing the R1 and R2 band count rates (which are statistically independent) and adding their uncertainties in quadrature. The R45 band data are formed in the same manner by adding the R4 and R5 band data. Figure 1 displays the band response functions for the four bands. The R1 and R2 bands are clearly not spectrally independent; however, the R45 band is reasonably cleanly separated from the R12 band. (The X-ray data used for the all-sky analysis of Paper I consisted of the R1 and R2 band data binned into $24' \times 24'$ pixels.)

The individual *ROSAT* bands are formed by pulse-height selection on individual events (detection of an X-ray photon), so each event is uniquely assigned to a single band providing statistical independence. The lack of spectral independence of the R1 and R2 bands is due to the poor intrinsic energy resolution of the proportional counters, which is $E/\Delta E \sim 1$ at $E \sim \frac{1}{4}$ keV. The spectral separation between the R12 band and the R45 band is provided by the carbon $K\alpha$ absorption edge of the proportional counter entrance window at 0.284 keV.

As will be addressed in § 3, the analysis presented here has been limited to approximately 10% of the sky, or roughly 10^5 pixels. Histograms of the statistical significance (count

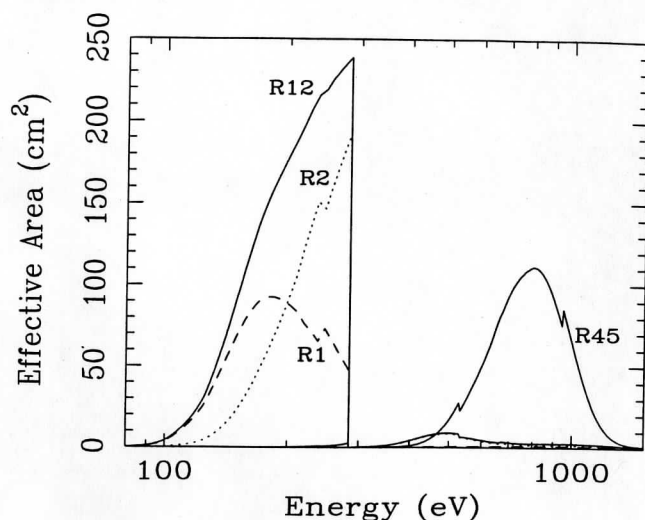


FIG. 1.—On-axis band response curves for the *ROSAT* R1 (dashed line), R2 (dotted line), R12 (solid line), and R45 (solid line) bands. The sharp break at 0.284 keV is due to the carbon $K\alpha$ absorption edge of the PSPC plastic entrance window. Other jumps in the curves are caused by the oxygen absorption edge at 0.532 keV from the window and the argon absorption edge at 0.245 keV and xenon absorption edge at 0.928 keV from the proportional counter gas. Note the very small overlap between the R45 band and the lower energy bands.

rate divided by the uncertainty in the count rate) of the individual pixels in the three $\frac{1}{4}$ keV maps used in this analysis are shown in Figure 2. While the significances are not in general as large as one would prefer, they are sufficient for this analysis, and the finer angular binning (than used in Paper I) allows an increased sampling of any fine structure in the column density of the absorbing interstellar medium.

2.2. Measure of Absorption Column Density

As in Paper I, we use the DIRBE-corrected *IRAS* 100 μ m data from Schlegel et al. (1998), cast into the same projections and pixels as the X-ray data, as a measure of absorption column density. However, they are slightly different from those used in Paper I as they are the product of the final processing used for the Schlegel et al. paper. The differences are minor and do not significantly affect the results.

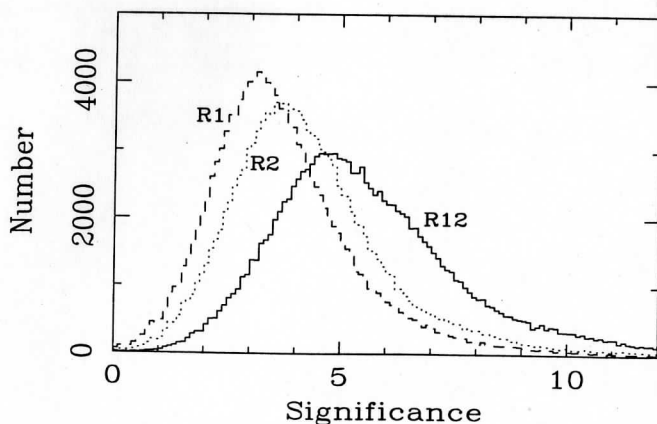


FIG. 2.—Histograms of the statistical significances (count rate divided by the uncertainty in the count rate, I/σ_I) for the $12' \times 12'$ pixels for the R1 (dashed line), R2 (dotted line), and R12 (solid line) bands.

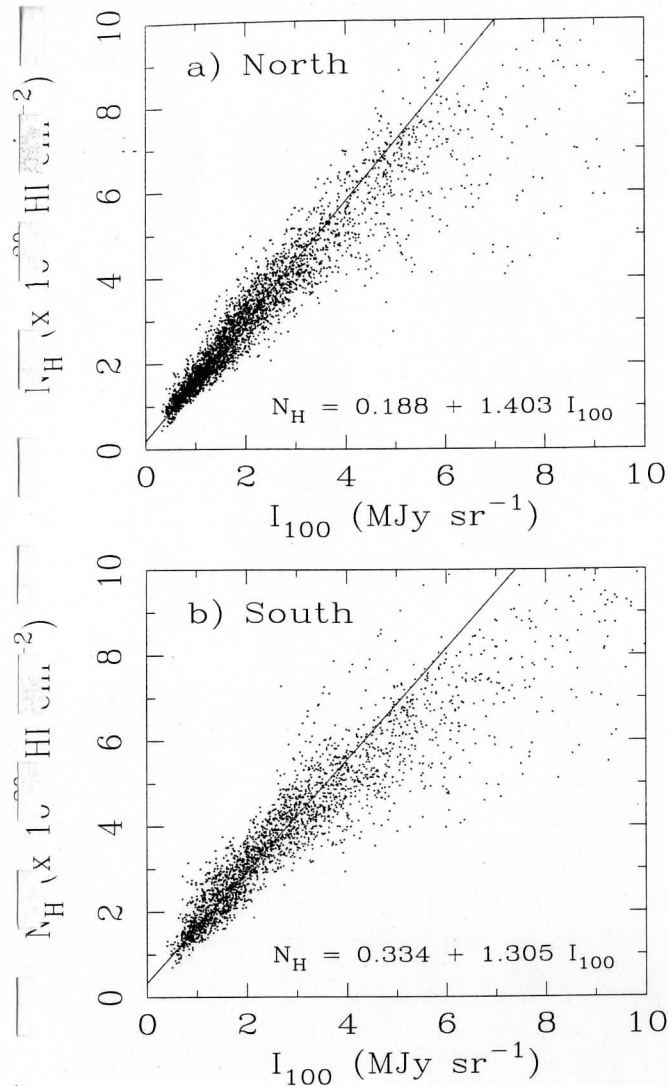


FIG. 3.—Scatter plots comparing the binned Schlegel et al. (1998) *IRAS* 100 μm data vs. the binned Hartmann & Burton (1997) N_{H} data in the (a) northern and (b) southern Galactic hemispheres (see text for details). The lines show the best-fit linear relation for H I column densities $\leq 4.0 \times 10^{20} \text{ H I cm}^{-2}$. The turnover at higher values of I_{100} is due to the presence of molecular gas.

The inherent angular resolution of the *IRAS* data ($\sim 5'$) exceeds by a factor of 5 the useful resolution of the X-ray data, which is limited by counting statistics rather than by the resolution of the detector (the angular resolution of *ROSAT* data, which is an average over the field of view, is $\sim 3'$). Using the *IRAS* data provides a major advantage over using the available H I surveys, which have at best $35'$ resolution with incomplete sky coverage. The disadvantage of the *IRAS* data is that they do not contain velocity information that would allow the straightforward separation of the X-ray-absorbing interstellar matter into distinct components, as can be done with the H I data. However, velocity information can be determined for distinct *IRAS* features by comparing the angular structure with the coarser resolution H I data (although that is beyond the scope of this paper). Another major advantage for the *IRAS* data is that they also sample molecular gas.

Since the *IRAS* data are scaled to column densities of Galactic neutral hydrogen at high Galactic latitudes, they

are an appropriate measure of X-ray-absorbing interstellar matter for this analysis (see Kuntz & Snowden [2000] for a more extensive discussion of this subject). The Schlegel et al. (1998) data were scaled to the column density of interstellar hydrogen by using the Leiden-Dwingeloo 21 cm survey of Hartmann & Burton (1997). Data in the Galactic polar regions were binned into 1.6×1.6 pixels and linear fits made to the northern and southern data separately. The range in N_{H} was limited to $\leq 4 \times 10^{20} \text{ H I cm}^{-2}$ to avoid the contribution of molecular gas to the I_{100} intensities and therefore contamination of the results. The scatter plots and fitted relations are shown in Figure 3. The fitted lines for the north and south are given by $N_{\text{H}} = 0.186 + 1.403 \times I_{100}$ and $N_{\text{H}} = 0.334 + 1.305 \times I_{100}$, respectively, where N_{H} is in units of $10^{20} \text{ H I cm}^{-2}$ and I_{100} is in units of MJy sr^{-1} . The turnover at higher values of I_{100} is due to the presence of molecular gas. The difference between the I_{100} to N_{H} scaling between the northern and southern hemispheres is not significant for our purposes. They provide similar results for low column densities where the analysis is most sensitive to systematic uncertainties (the cross-over of the curves is at $N_{\text{H}} \sim 3 \times 10^{20} \text{ cm}^{-2}$). At higher column densities where the relations diverge the column densities are optically thick.

3. ANALYSIS

3.1. Selection of Target Regions

The selection of the locations and sizes of the regions, or shadows, that were analyzed for this paper was subjective, but not arbitrary. The selection criteria were that there be an apparent absorption feature in the $\frac{1}{4}$ keV background and/or an emission feature in the N_{H} map, that there be a reasonable range in the column densities of H I in the vicinity of this feature (most of the regions have a range greater than one optical depth), and that the minimum column density of H I in the vicinity be reasonably low. These criteria select regions where the total column density is low enough for the R12 band to still be sensitive to distant emission and where the range in N_{H} is large enough to provide an acceptable lever arm for the fit. Since one optical depth for X-rays at $\frac{1}{4}$ keV is $\sim 1 \times 10^{20} \text{ H I cm}^{-2}$, regions with a minimum sampled column density $\leq 4 \times 10^{20} \text{ H I cm}^{-2}$ corresponding to a minimum optical depth ≤ 3 were used (note that optical depth is not a linear function of N_{H} , see Snowden et al. 1994b). These selection criteria limited the analysis to roughly the 40% of the sky with the lowest column density. However, the criteria were occasionally relaxed in order to better sample the local component, i.e., directions of higher column density where all observed emission can reasonably be assumed to be local in origin. For these regions the background emission is not well constrained.

Regions affected by known supernova remnants and superbubbles, specifically Loop I, the Eridanus superbubble, and the Monoceros-Gemini ring, were excluded. The studies of emission and absorption variations of such features using *ROSAT* data are certainly interesting in their own right (e.g., Loop I [Egger 1993], Eridanus [Snowden et al. 1995a; Guo et al. 1995] and Monogem [Plucinsky et al. 1996]), but are more appropriately left for detailed investigations of the specific object. The locations of the regions selected for analysis here are shown in Figure 4, where rings showing the extent of the regions are overlaid on both $\frac{1}{4}$ keV X-ray and *IRAS* maps. The radii of the target regions

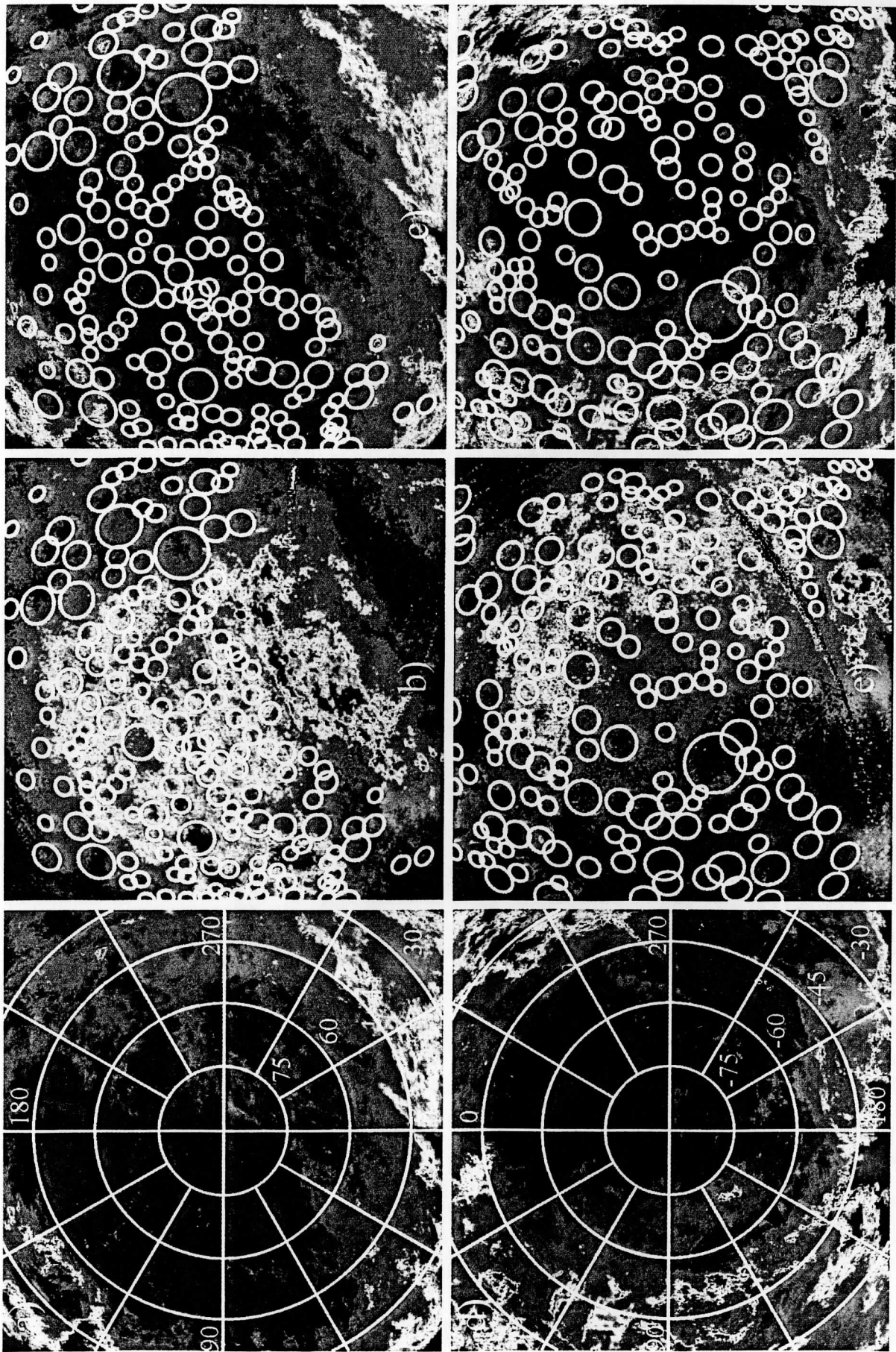


FIG. 4.—Locations and extents of the regions selected for this analysis. Panels (a) and (d) show copies of the *IRAS* 100 μm data with the Galactic coordinate grid overlaid. The data are shown using the same zenith equal area (ZEA) projection as used in Snowden et al. (1997). Panel (b) shows the northern regions overlaid on the R12 band X-ray data. The color range is $200\text{--}1500 \times 10^{-6}$ R12 band counts $\text{s}^{-1} \text{arcmin}^{-2}$. Panel (c) shows the northern regions overlaid on the scaled *IRAS* 100 μm data in the same projection. The color range is $0.2\text{--}15.0 \times 10^{30}$ H cm^{-2} in a square-root scaling. Panels (e) and (f) are the same as panels (b) and (c) except that they show the southern regions.

are determined by the angular extents of the absorption and/or emission features. In practice, all but three of the target regions are $\leq 8^\circ$ in diameter. Near some of the larger features, several smaller regions were also selected for analysis in order to independently sample different parts of the feature to test for variation in either the foreground or background X-ray intensities.

An effort was made to have the selected regions be distributed over the available lower column density parts of the sky, which occasionally required relaxing some of the selection criteria above. While the sky coverage is certainly not uniform, because the distribution of suitable targets is not uniform, the sky covered is reasonably representative of the whole at high latitudes.

3.2. Fitted Model

A physical picture similar to that used in Paper I was assumed here for the relative locations of the X-ray-emitting plasmas responsible for the bulk of the $\frac{1}{4}$ keV background and the cooler X-ray-absorbing gas in the interstellar medium. Specifically, it consists of an unabsorbed foreground X-ray emission region (the Local Hot Bubble; see Paper I), a region of neutral, X-ray-absorbing M that includes the shadowing cloud and all other Galactic H I along the line of sight, and a region of X-ray-emitting plasma in the Galactic halo that is not intermixed in the neutral ISM and that produces most of the observed $\frac{1}{4}$ keV background of distant origin (from Paper I this component has a temperature of $\sim 10^{6.0}$ K). Paper I assumed an isotropic extragalactic background power law with an index taken from Hasinger et al. (1993) of 1.96 and a normalization fixed to be consistent with extragalactic $\frac{1}{4}$ keV shadowing results (e.g., M 101 [Snowden & Pietsch 1995], NGC 55 [Barber, Roberts, & Warwick 1996], and several additional face-on galaxies [Cui et al. 1996]).

To make our current picture more physically realistic, we added the following refinement to the distant emission of Paper I model. The previous isotropic extragalactic background power law has been replaced with two components: (1) an isotropic power law ($10.5 E^{-1.46}$ photons $\text{cm}^{-2} \text{s}^{-1} \text{sr}^{-1} \text{keV}^{-1}$, the fitted power law of model A from Fabian, & Gendreau [1997]), which is the extrapolation of the extragalactic background observed above ~ 1 keV and is consistent with the observed flux in the *ROSAT* 1.2 keV band, and (2) an anisotropic $T = 10^{6.4}$ K thermal component that accounts for the observed excess of the diffuse X-ray background at $\frac{3}{4}$ keV above the extrapolation of the power law. We used the R45 band data to determine the intensity of the $10^{6.4}$ K thermal component for each shadow region individually. The sum of these two distant components, when extrapolated to the $\frac{1}{4}$ keV band, produces an intensity similar to that of the extragalactic power law assumed for Paper I. The advantage to this revision is that the model now represents the entire 0.1–2.0 keV *ROSAT* spectrum in a self-consistent manner, at least in a general sense. The broadband intensities in the 0.5–2.0 keV band are well fitted with reasonable spectra. These spectra can then be extrapolated down to the $\frac{1}{4}$ keV band to derive reasonable estimates for their contributions to that band. As will be shown below, this more complicated model has little actual effect on the shadow results in the $\frac{1}{4}$ keV band. The assumed geometry for the LHB, absorbing gas, and cooler ($T \sim 10^{6.0}$ keV) region of halo X-ray emission is shown schematically in Figure 5a.

Mathematically, the following equation is fitted separately to the R1, R2, and R12 band data:

$$I_X = I_0 + I_1 \times \exp[-\sigma(N_H, T_{6.0}) \times N_H] \\ + I_{6.4} \times \exp[-\sigma(N_H, T_{6.4}) \times N_H] \\ + I_{\text{eg}} \times \exp[-\sigma(N_H, \alpha_{1.46}) \times N_H].$$

Note that the data in the R1, R2, and R12 bands are fitted independently and that only the parameters I_0 and I_1 are allowed to vary. I_X is the observed X-ray intensity, I_0 is the fitted foreground component, and I_1 is the fitted distant (halo) component, which is absorbed by the column density N_H ; $\sigma(N_H, T_{6.0})$ is the theoretical band-averaged absorption cross section (based on the cross sections of Morrison & McCammon [1983]), which is a function both of N_H and the temperature of the I_1 component (see Snowden et al. 1994b). The fits were first done using $T = 10^{6.02}$ K, the value from Paper I, but were refitted using the value $T = 10^{6.00}$ K based on the initial results. $I_{6.4}$ is the intensity of the hot Galactic halo component that is determined from the R45 band data and is fixed separately for each region; it is absorbed by the column density N_H . $\sigma(N_H, T_{6.4})$ is the theoretical band-averaged absorption cross section for this component. I_{eg} is the fixed isotropic extragalactic power-law contribution, and $\sigma(N_H, \alpha_{1.46})$ is the theoretical band-averaged absorption cross section, which is a function both of N_H and power-law index, α . As noted above, the spectrum of the extragalactic power law is taken to be $10.5 E^{-1.46}$ photons $\text{cm}^{-2} \text{s}^{-1} \text{sr}^{-1} \text{keV}^{-1}$, and is extrapolated to $\frac{1}{4}$ keV and evaluated on a band-by-band basis. The normalization for the hot ($10^{6.4}$ K) halo contribution was determined in the following manner: (1) The absorbed power law contribution in the R45 band was subtracted from the average R45 band intensity over each shadow region. (2) This excess, minus a small amount (10^{-5} counts $\text{s}^{-1} \text{arcmin}^{-2}$) assumed to arise from the LHB (with an assumed temperature of $10^{6.0}$ K and typical high-latitude normalization set by Paper I), was deabsorbed by the average column density of the region. (3) This deabsorbed value was attributed to R45 band emission from the $T = 10^{6.4}$ K component. (4) Finally, the $T = 10^{6.4}$ K spectrum was extrapolated to the R1, R2, and R12 bands to fix $I_{6.4}$.

Following Paper I, the assumed spectra of the I_1 and $I_{6.4}$ components are Raymond & Smith (1977; Raymond 1992; J. C. Smith 1991, private communication [computer code update]⁶) thermal equilibrium plasma models using cosmic abundances with $T = 10^{6.0}$ and $T = 10^{6.4}$ K, respectively. The choice of the spectrum affects the analysis in two ways: (1) The band-averaged absorption cross sections are spectrally dependent, but only to a limited extent, and (2) the choice of the temperature for the hotter halo component affects the amount of emission and band ratios (to the few percent level) attributed to the $\frac{1}{4}$ keV band. The R12/R45 band ratio decreases by a factor of 4 for spectra between $10^{6.3}$ and $10^{6.5}$ K. However, the predicted unabsorbed R12 band intensity for a typical region, even assuming a $10^{6.3}$ K spectrum, is only comparable to the intensity from the extragalactic power law. We have chosen $T = 10^{6.4}$ K following Nousek et al. (1982), but this choice is confirmed by Kuntz & Snowden (2000).

⁶ While there are more recent versions of various plasma codes, use of the 1991 vintage allows direct comparisons with previous work by these authors.

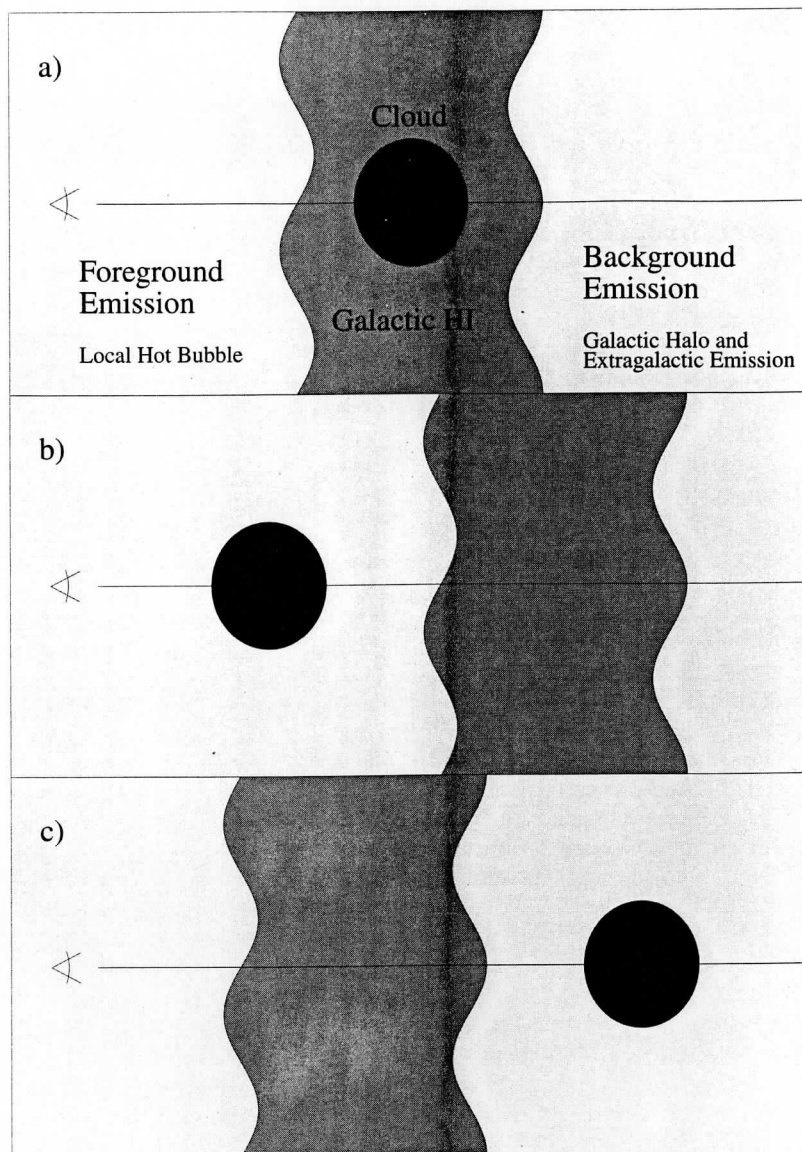


FIG. 5.—Schematic diagrams of ISM shadowing geometries. (a) The assumed geometry for the model fits. (b) Shadowing cloud located within the foreground emission region. (c) Shadowing cloud located within the distant (halo) emission region.

There are a number of alternatives to our simple assumed geometry. The most likely are that the cloud or absorbing feature is located within the foreground X-ray emission region (Fig. 5b) or within the X-ray emission region(s) in the halo (Fig. 5c), i.e., there is some form of intermixture of the X-ray-emitting and -absorbing gas. These variations, while adding some complexity to their interpretations, do not appreciably affect the results. For example, if the shadowing cloud lies within the local emission region, Figure 5b, the fitted distant component includes the emission between the cloud and the edge of the emission region (wall) as well as any more distant emission beyond the wall. In such a situation, the fitting algorithm incorrectly deabsorbs the emission between the cloud and wall by the H I of the wall and “adds” it to the total distant component. Because of this, the attributions of “foreground” and “distant” emission

may need to be reevaluated once the distances to the absorbing features are known.

4. RESULTS

4.1. Shadows

The results of the fits for the R1, R2, and R12 bands are listed in Table 1. For each target region, the table lists the Galactic coordinates of the region center, the diameter of the region, the fitted values for the R1, R2, and R12 band fits and their associated χ^2_{ν} values for the fits, and the number of degrees of freedom. Scatter plots of the R12 band data versus the column density of H I along with the fitted curves are shown in Figure 6. Inspection of both the table and figure shows the wide range of both X-ray emission and absorption covered by the shadows. The errors quoted in

COORDINATES^a

BAND R1

BAND R2

BAND R12

| NUMBER | SHADOW NAME | l | b | Size ^b | I ₀ ^c | I ₁ ^c | χ _v ^{2,d} | I ₀ ^c | I ₁ ^c | χ _v ^{2,d} | I ₀ ^c | I ₁ ^c | χ _v ^{2,d} | ν ^e |
|--------|-------------|-------|--------|-------------------|-----------------------------|-----------------------------|-------------------------------|-----------------------------|-----------------------------|-------------------------------|-----------------------------|-----------------------------|-------------------------------|----------------|
| 1 | S0047M461 | 4.69 | -46.09 | 6.00 | 204 ± 7 | 488 ± 140 | 1.01 | 236 ± 9 | 572 ± 83 | 1.05 | 463 ± 12 | 1047 ± 148 | 1.08 | 707 |
| 2 | S0049M557 | 4.92 | -55.66 | 4.80 | 329 ± 42 | <428 ^f | 1.16 | 352 ± 65 | 482 ± 217 | 1.29 | 714 ± 77 | 698 ± 328 | 1.31 | 439 |
| 3 | S0070M826 | 7.03 | -82.64 | 4.00 | 185 ± 32 | <259 | 1.11 | 234 ± 51 | <309 | 1.06 | 447 ± 60 | <449 | 1.11 | 315 |
| 4 | S0078M352 | 7.82 | -35.18 | 6.00 | 129 ± 12 | 1481 ± 357 | 0.91 | 117 ± 17 | 1613 ± 206 | 0.92 | 266 ± 21 | 3224 ± 370 | 0.97 | 642 |
| 5 | S0131M461 | 13.09 | -46.12 | 4.00 | 180 ± 9 | 1496 ± 352 | 1.23 | 190 ± 10 | 1957 ± 183 | 1.07 | 399 ± 14 | 3538 ± 343 | 1.10 | 315 |
| 6 | S0138M511 | 13.78 | -51.06 | 3.20 | 142 ± 35 | 1869 ± 424 | 1.08 | 119 ± 53 | 1814 ± 311 | 1.37 | 281 ± 64 | 3666 ± 509 | 1.42 | 195 |
| 7 | S0140M637 | 13.98 | -63.70 | 4.00 | 263 ± 66 | 524 ± 371 | 1.45 | 327 ± 105 | 584 ± 339 | 1.17 | 719 ± 124 | 774 ± 511 | 1.38 | 314 |
| 8 | S0142M538 | 14.15 | -53.82 | 3.20 | 248 ± 34 | 822 ± 306 | 0.99 | 343 ± 52 | 691 ± 240 | 1.13 | 610 ± 62 | 1491 ± 383 | 1.16 | 195 |
| 9 | S0179M484 | 17.90 | -48.43 | 4.00 | 210 ± 21 | 1146 ± 389 | 1.14 | 239 ± 29 | 1374 ± 245 | 1.05 | 470 ± 36 | 2552 ± 424 | 1.18 | 315 |
| 10 | S0183M346 | 18.32 | -34.63 | 3.20 | 104 ± 14 | 1959 ± 787 | 0.82 | 137 ± 19 | 1400 ± 403 | 1.16 | 260 ± 24 | 3078 ± 748 | 1.02 | 187 |
| 11 | S0195M448 | 19.51 | -44.81 | 4.00 | 176 ± 10 | 1567 ± 378 | 1.18 | 201 ± 12 | 1743 ± 203 | 1.25 | 398 ± 16 | 3349 ± 373 | 1.34 | 315 |
| 12 | S0201M530 | 20.13 | -53.04 | 4.00 | 160 ± 27 | 1549 ± 246 | 1.02 | 243 ± 43 | 1173 ± 199 | 1.21 | 404 ± 51 | 2714 ± 314 | 1.23 | 314 |
| 13 | S0237M437 | 23.67 | -43.66 | 3.20 | 184 ± 25 | <1000 | 1.07 | 228 ± 37 | 857 ± 387 | 1.16 | 448 ± 46 | 1184 ± 675 | 1.12 | 195 |
| 14 | S0248M357 | 24.76 | -35.73 | 4.00 | 143 ± 10 | 1244 ± 657 | 1.03 | 188 ± 14 | 1766 ± 357 | 1.18 | 349 ± 17 | 3213 ± 648 | 1.10 | 313 |
| 15 | S0250M679 | 25.05 | -67.90 | 6.00 | 215 ± 33 | <405 | 0.90 | 225 ± 47 | 282 ± 237 | 1.04 | 460 ± 61 | 790 ± 411 | 1.01 | 638 |
| 16 | S0260M309 | 26.01 | -30.93 | 3.20 | 74 ± 16 | 2924 ± 579 | 0.97 | 49 ± 22 | 3478 ± 333 | 1.37 | 132 ± 28 | 6849 ± 598 | 1.43 | 186 |
| 17 | S0261M499 | 26.11 | -49.87 | 6.00 | 139 ± 12 | 1729 ± 224 | 1.12 | 196 ± 19 | 1230 ± 148 | 1.10 | 354 ± 23 | 2783 ± 253 | 1.17 | 707 |
| 18 | S0291P828 | 29.05 | 82.79 | 4.00 | 270 ± 32 | 380 ± 138 | 1.13 | 329 ± 49 | 297 ± 133 | 1.20 | 580 ± 58 | 757 ± 193 | 1.29 | 315 |
| 19 | S0332M526 | 33.21 | -52.65 | 6.00 | 256 ± 26 | 497 ± 303 | 1.16 | 286 ± 39 | 889 ± 221 | 1.12 | 582 ± 47 | 1403 ± 364 | 1.20 | 707 |
| 20 | S0341M405 | 34.12 | -40.52 | 6.00 | 114 ± 7 | 2612 ± 313 | 1.17 | 141 ± 9 | 2300 ± 174 | 1.28 | 272 ± 12 | 4808 ± 314 | 1.39 | 707 |
| 21 | S0363P770 | 36.25 | 76.95 | 4.80 | 281 ± 34 | 274 ± 149 | 1.37 | 371 ± 52 | 163 ± 142 | 1.45 | 666 ± 61 | 425 ± 208 | 1.68 | 439 |
| 22 | S0370M829 | 37.03 | -82.86 | 4.00 | 139 ± 46 | 294 ± 269 | 1.08 | 164 ± 72 | 299 ± 239 | 1.27 | 329 ± 86 | 573 ± 364 | 1.25 | 315 |
| 23 | S0373P446 | 37.28 | 44.65 | 3.20 | 168 ± 10 | 2981 ± 776 | 1.16 | 181 ± 12 | 2974 ± 352 | 1.24 | 362 ± 16 | 5906 ± 679 | 1.29 | 195 |
| 24 | S0382M571 | 38.25 | -57.08 | 4.00 | 229 ± 13 | <483 | 1.42 | 218 ± 39 | 728 ± 299 | 1.82 | 470 ± 50 | 1104 ± 531 | 2.05 | 316 |
| 25 | S0383M214 | 38.26 | -21.43 | 3.20 | 96 ± 9 | 4181 ± 1021 | 0.88 | 123 ± 12 | 3233 ± 469 | 1.11 | 232 ± 15 | 7277 ± 898 | 1.09 | 180 |
| 26 | S0383M308 | 38.26 | -30.84 | 3.20 | 117 ± 14 | 4032 ± 1130 | 1.29 | 205 ± 20 | 2673 ± 590 | 1.13 | 350 ± 25 | 5755 ± 1089 | 1.25 | 195 |
| 27 | S0394M341 | 39.41 | -34.10 | 6.00 | 128 ± 5 | 1671 ± 260 | 1.15 | 171 ± 6 | 2021 ± 140 | 1.17 | 318 ± 8 | 3811 ± 256 | 1.21 | 704 |
| 28 | S0395M463 | 39.48 | -46.33 | 4.00 | 169 ± 16 | 552 ± 506 | 1.18 | 199 ± 21 | 786 ± 271 | 1.16 | 394 ± 27 | 1423 ± 501 | 1.19 | 312 |
| 29 | S0399M644 | 39.89 | -64.37 | 4.80 | 157 ± 60 | <1205 | 0.84 | <88 | 1528 ± 550 | 0.99 | 239 ± 112 | 2181 ± 955 | 0.96 | 382 |
| 30 | S0413P245 | 41.30 | 24.50 | 4.00 | 155 ± 12 | 1699 ± 804 | 1.22 | 214 ± 17 | 778 ± 390 | 1.37 | 385 ± 22 | 1954 ± 739 | 1.39 | 315 |
| 31 | S0415M543 | 41.54 | -54.29 | 4.00 | 92 ± 38 | 2447 ± 580 | 1.25 | <58 | 2771 ± 404 | 1.44 | 102 ± 70 | 5295 ± 677 | 1.71 | 315 |
| 32 | S0421P585 | 42.14 | 58.45 | 4.00 | 214 ± 15 | <337 | 1.07 | 209 ± 20 | 630 ± 136 | 1.17 | 446 ± 25 | 915 ± 238 | 0.97 | 314 |
| 33 | S0422P634 | 42.23 | 63.43 | 4.00 | 235 ± 17 | 428 ± 133 | 1.06 | 262 ± 25 | 542 ± 106 | 1.27 | 514 ± 31 | 981 ± 168 | 1.20 | 315 |
| 34 | S0425M248 | 42.54 | -24.79 | 3.20 | 114 ± 11 | 4504 ± 900 | 1.26 | 148 ± 15 | 3869 ± 439 | 1.11 | 275 ± 19 | 8210 ± 827 | 1.28 | 193 |
| 35 | S0429M310 | 42.95 | -30.99 | 3.20 | 136 ± 15 | 1315 ± 734 | 1.04 | 152 ± 21 | 2599 ± 407 | 1.08 | 298 ± 27 | 4673 ± 738 | 1.04 | 194 |
| 36 | S0440P399 | 44.00 | 39.91 | 4.80 | 203 ± 12 | <585 | 1.36 | 226 ± 15 | 474 ± 175 | 1.28 | 457 ± 20 | 696 ± 323 | 1.33 | 437 |
| 37 | S0443M268 | 44.34 | -26.76 | 3.20 | 109 ± 18 | 3085 ± 806 | 1.15 | 107 ± 27 | 3341 ± 462 | 1.46 | 238 ± 34 | 6510 ± 831 | 1.51 | 192 |
| 38 | S0448P558 | 44.76 | 55.84 | 4.80 | 207 ± 24 | <377 | 1.01 | 250 ± 34 | 363 ± 174 | 1.02 | 490 ± 43 | 507 ± 290 | 1.06 | 410 |
| 39 | S0450M374 | 45.00 | -37.40 | 6.00 | 133 ± 4 | 1498 ± 168 | 1.19 | 169 ± 5 | 1215 ± 89 | 1.27 | 316 ± 7 | 2681 ± 165 | 1.34 | 703 |
| 40 | S0456M481 | 45.59 | -48.06 | 4.00 | 131 ± 23 | 1269 ± 505 | 1.03 | 186 ± 35 | 1489 ± 328 | 1.23 | 353 ± 43 | 2660 ± 568 | 1.23 | 314 |
| 41 | S0458M325 | 45.80 | -32.45 | 3.20 | 123 ± 9 | 1657 ± 728 | 0.93 | 133 ± 11 | 1665 ± 337 | 1.01 | 275 ± 15 | 3113 ± 649 | 0.94 | 191 |
| 42 | S0461P276 | 46.06 | 27.56 | 4.00 | 175 ± 12 | 731 ± 702 | 1.15 | 186 ± 15 | 452 ± 322 | 1.29 | 373 ± 20 | 1127 ± 626 | 1.23 | 314 |
| 43 | S0485P429 | 48.54 | 42.92 | 4.80 | 164 ± 8 | 601 ± 101 | 1.21 | 174 ± 10 | 792 ± 69 | 1.27 | 352 ± 13 | 1456 ± 116 | 1.22 | 439 |
| 44 | S0491M253 | 49.13 | -25.35 | 6.00 | 104 ± 6 | 2045 ± 852 | 0.94 | 128 ± 8 | 1706 ± 366 | 1.18 | 243 ± 10 | 3991 ± 728 | 1.12 | 695 |
| 45 | S0505M709 | 50.54 | -70.87 | 8.00 | 133 ± 14 | 529 ± 154 | 1.19 | 107 ± 21 | 664 ± 112 | 1.23 | 264 ± 26 | 1254 ± 186 | 1.29 | 1241 |

TABLE 1—Continued

| NUMBER | SHADOW NAME | COORDINATES ^a | | | BAND R1 | | | | BAND R2 | | | | BAND R12 | | | |
|--------|-------------|--------------------------|----------|-------------------|------------------------------------|------------------------------------|------------|------------------------------------|------------------------------------|------------|------------------------------------|------------------------------------|------------|------------------------------------|------------------------------------|------------|
| | | <i>l</i> | <i>b</i> | Size ^b | <i>I</i> ₀ ^c | <i>I</i> ₁ ^c | χ^2_d | <i>I</i> ₀ ^c | <i>I</i> ₁ ^c | χ^2_d | <i>I</i> ₀ ^c | <i>I</i> ₁ ^c | χ^2_d | <i>I</i> ₀ ^c | <i>I</i> ₁ ^c | χ^2_d |
| 46 | S0506P680 | 50.56 | 67.98 | 4.80 | 256 ± 25 | 522 ± 101 | 1.22 | 284 ± 39 | 573 ± 103 | 1.34 | 558 ± 45 | 1088 ± 145 | 1.56 | 439 | | |
| 47 | S0509M404 | 50.91 | -40.41 | 6.00 | 135 ± 14 | 1548 ± 246 | 1.19 | 168 ± 23 | 1763 ± 175 | 1.27 | 328 ± 27 | 3353 ± 290 | 1.45 | 705 | | |
| 48 | S0515P386 | 51.54 | 38.62 | 6.00 | 197 ± 8 | 598 ± 120 | 1.13 | 189 ± 11 | 839 ± 77 | 1.21 | 402 ± 14 | 1491 ± 134 | 1.32 | 705 | | |
| 49 | S0516M300 | 51.56 | -30.03 | 4.00 | 133 ± 8 | 3536 ± 949 | 0.87 | 169 ± 10 | 2058 ± 407 | 1.18 | 312 ± 13 | 5076 ± 804 | 1.12 | 314 | | |
| 50 | S0531M553 | 53.10 | -55.33 | 8.00 | 186 ± 7 | <387 | 0.85 | 200 ± 18 | 386 ± 220 | 1.01 | 421 ± 24 | 602 ± 418 | 0.89 | 1158 | | |
| 51 | S0532P549 | 53.23 | 54.87 | 4.00 | 209 ± 42 | <506 | 1.01 | 242 ± 62 | 384 ± 298 | 1.10 | 486 ± 76 | 511 ± 486 | 1.05 | 305 | | |
| 52 | S0560P638 | 56.00 | 63.84 | 4.00 | 309 ± 30 | <260 | 2.58 | 384 ± 47 | 159 ± 132 | 3.20 | 692 ± 54 | 328 ± 192 | 4.83 | 315 | | |
| 53 | S0567M402 | 56.67 | -40.22 | 6.00 | 120 ± 6 | 1548 ± 279 | 1.02 | 133 ± 7 | 1775 ± 143 | 1.08 | 270 ± 9 | 3515 ± 267 | 1.15 | 668 | | |
| 54 | S0573P409 | 57.34 | 40.88 | 3.20 | 219 ± 39 | 796 ± 303 | 0.97 | 231 ± 62 | 885 ± 253 | 1.22 | 454 ± 73 | 1748 ± 391 | 1.15 | 195 | | |
| 55 | S0576P711 | 57.58 | 71.08 | 4.00 | 387 ± 9 | <61 | 1.16 | 448 ± 10 | <108 | 1.49 | 850 ± 14 | <81 | 1.44 | 316 | | |
| 56 | S0578P488 | 57.77 | 48.81 | 6.00 | 188 ± 15 | 506 ± 87 | 1.25 | 215 ± 22 | 500 ± 77 | 1.49 | 419 ± 26 | 1019 ± 116 | 1.62 | 704 | | |
| 57 | S0599M878 | 59.93 | -87.80 | 4.80 | 183 ± 6 | <47 | 1.35 | 279 ± 7 | <45 | 1.40 | 484 ± 8 | <67 | 1.59 | 440 | | |
| 58 | S0603P397 | 60.33 | 39.72 | 3.20 | 274 ± 36 | 541 ± 212 | 1.10 | 279 ± 50 | 768 ± 169 | 1.25 | 577 ± 62 | 1321 ± 269 | 1.32 | 195 | | |
| 59 | S0604P359 | 60.43 | 35.93 | 4.00 | 181 ± 11 | 1117 ± 114 | 0.94 | 179 ± 16 | 1142 ± 86 | 1.26 | 367 ± 20 | 2258 ± 139 | 1.32 | 315 | | |
| 60 | S0610P137 | 60.96 | 13.69 | 6.00 | 150 ± 3 | 2947 ± 782 | 1.09 | 186 ± 4 | 2457 ± 311 | 1.24 | 348 ± 5 | 5024 ± 620 | 1.21 | 706 | | |
| 61 | S0611P324 | 61.07 | 32.38 | 3.20 | 183 ± 22 | <913 | 1.10 | 209 ± 31 | 859 ± 287 | 1.15 | 404 ± 39 | 1412 ± 500 | 1.25 | 195 | | |
| 62 | S0611M340 | 61.11 | -34.01 | 3.20 | 128 ± 11 | 996 ± 650 | 1.04 | 138 ± 15 | 1957 ± 347 | 1.17 | 283 ± 19 | 3369 ± 637 | 1.33 | 187 | | |
| 63 | S0614P281 | 61.37 | 28.15 | 6.00 | 204 ± 9 | 1009 ± 148 | 1.21 | 254 ± 14 | 1133 ± 101 | 1.42 | 468 ± 17 | 2161 ± 169 | 1.49 | 707 | | |
| 64 | S0618M294 | 61.79 | -29.38 | 8.00 | 142 ± 5 | 1652 ± 198 | 1.13 | 184 ± 7 | 2065 ± 115 | 1.30 | 345 ± 8 | 3859 ± 204 | 1.37 | 1245 | | |
| 65 | S0623P359 | 62.34 | 33.89 | 3.20 | 200 ± 18 | 512 ± 438 | 1.39 | 233 ± 25 | 567 ± 256 | 1.40 | 453 ± 31 | 980 ± 456 | 1.40 | 195 | | |
| 66 | S0629P354 | 62.91 | 35.37 | 3.20 | 193 ± 14 | 988 ± 284 | 1.28 | 196 ± 19 | 1042 ± 174 | 1.23 | 402 ± 24 | 2004 ± 305 | 1.28 | 195 | | |
| 67 | S0640P756 | 63.97 | 75.61 | 4.00 | 312 ± 35 | 253 ± 170 | 1.28 | 333 ± 54 | 355 ± 158 | 1.29 | 669 ± 64 | 601 ± 233 | 1.45 | 315 | | |
| 68 | S0646P316 | 64.55 | 31.58 | 3.20 | 194 ± 24 | <797 | 1.44 | 238 ± 36 | 574 ± 313 | 1.60 | 438 ± 43 | 1020 ± 538 | 1.95 | 195 | | |
| 69 | S0646P468 | 64.59 | 46.80 | 4.00 | 213 ± 44 | 688 ± 144 | 1.69 | 216 ± 71 | 730 ± 156 | 2.62 | 459 ± 81 | 1402 ± 214 | 2.96 | 315 | | |
| 70 | S0663M410 | 66.30 | -41.02 | 4.80 | 123 ± 4 | 1392 ± 337 | 0.81 | 160 ± 10 | 887 ± 173 | 0.92 | 304 ± 13 | 2119 ± 325 | 0.88 | 415 | | |
| 71 | S0669M588 | 66.85 | -58.84 | 6.00 | 147 ± 17 | 868 ± 271 | 1.01 | 177 ± 24 | 608 ± 215 | 1.25 | 358 ± 31 | 1234 ± 383 | 1.16 | 700 | | |
| 72 | S0674P246 | 67.37 | 24.63 | 2.80 | 185 ± 13 | 868 ± 271 | 1.01 | 239 ± 18 | 970 ± 166 | 1.26 | 432 ± 22 | 1837 ± 288 | 1.48 | 147 | | |
| 73 | S0684P527 | 68.40 | 52.67 | 6.00 | 210 ± 12 | 791 ± 91 | 1.51 | 213 ± 19 | 809 ± 77 | 1.38 | 431 ± 22 | 1635 ± 116 | 1.82 | 706 | | |
| 74 | S0689P459 | 68.87 | 45.93 | 3.20 | 431 ± 70 | 709 ± 275 | 1.52 | 446 ± 110 | 742 ± 277 | 2.01 | 919 ± 128 | 1392 ± 394 | 2.28 | 195 | | |
| 75 | S0697M219 | 69.67 | -21.90 | 4.00 | 169 ± 12 | <2545 | 1.29 | 238 ± 17 | 2549 ± 698 | 1.55 | 421 ± 21 | 4296 ± 1304 | 1.87 | 314 | | |
| 76 | S0700M510 | 69.95 | -51.04 | 4.00 | 163 ± 14 | <1319 | 1.01 | 190 ± 8 | <280 | 0.88 | 378 ± 17 | <625 | 1.02 | 297 | | |
| 77 | S0715P250 | 71.49 | 24.99 | 2.80 | 188 ± 12 | 807 ± 277 | 1.19 | 257 ± 16 | 759 ± 166 | 1.28 | 452 ± 20 | 1513 ± 290 | 1.50 | 147 | | |
| 78 | S0723P353 | 72.28 | 35.28 | 4.00 | 195 ± 11 | 711 ± 127 | 1.28 | 208 ± 17 | 843 ± 95 | 1.20 | 413 ± 21 | 1568 ± 154 | 1.39 | 315 | | |
| 79 | S0728P393 | 72.75 | 39.28 | 4.00 | 220 ± 17 | 847 ± 109 | 1.41 | 278 ± 25 | 723 ± 93 | 1.63 | 499 ± 30 | 1565 ± 143 | 1.94 | 315 | | |
| 80 | S0737P287 | 73.69 | 28.73 | 2.80 | 188 ± 13 | 686 ± 198 | 0.97 | 230 ± 19 | 878 ± 139 | 1.57 | 425 ± 23 | 1611 ± 229 | 1.36 | 147 | | |
| 81 | S0740P156 | 74.00 | 15.60 | 3.20 | 169 ± 12 | 2685 ± 1015 | 1.13 | 225 ± 17 | 2548 ± 489 | 1.25 | 403 ± 21 | 5393 ± 921 | 1.09 | 195 | | |
| 82 | S0743P807 | 74.31 | 80.75 | 4.00 | 296 ± 37 | 220 ± 144 | 1.25 | 385 ± 58 | 151 ± 144 | 1.57 | 679 ± 68 | 398 ± 206 | 1.73 | 315 | | |
| 83 | S0744P429 | 74.42 | 42.90 | 3.20 | 334 ± 28 | 630 ± 156 | 1.47 | 393 ± 44 | 575 ± 146 | 2.04 | 722 ± 51 | 1255 ± 215 | 2.55 | 195 | | |
| 84 | S0753M451 | 75.30 | -45.13 | 4.80 | 136 ± 7 | 977 ± 573 | 1.01 | 149 ± 9 | 859 ± 259 | 1.05 | 305 ± 12 | 1707 ± 506 | 1.09 | 424 | | |
| 85 | S0754P329 | 75.44 | 32.91 | 3.20 | 183 ± 17 | 787 ± 178 | 1.21 | 181 ± 25 | 971 ± 133 | 1.63 | 374 ± 30 | 1792 ± 215 | 1.75 | 195 | | |
| 86 | S0759M501 | 75.93 | -50.13 | 4.00 | 122 ± 9 | 1169 ± 508 | 1.09 | 158 ± 12 | 586 ± 236 | 1.25 | 309 ± 16 | 1351 ± 465 | 0.96 | 314 | | |
| 87 | S0762P170 | 76.21 | 17.04 | 3.20 | 181 ± 17 | 1663 ± 785 | 1.08 | 273 ± 23 | 780 ± 402 | 1.31 | 464 ± 29 | 2058 ± 745 | 1.20 | 195 | | |
| 88 | S0766P625 | 76.63 | 62.50 | 4.00 | 231 ± 23 | 342 ± 124 | 1.18 | 268 ± 35 | 475 ± 113 | 1.40 | 525 ± 42 | 793 ± 169 | 1.42 | 315 | | |
| 89 | S0767P552 | 76.65 | 55.25 | 6.00 | 183 ± 11 | 1032 ± 72 | 1.44 | 175 ± 16 | 980 ± 60 | 1.57 | 364 ± 19 | 2012 ± 93 | 1.93 | 707 | | |
| 90 | S0778P276 | 77.81 | 27.62 | 4.00 | 205 ± 11 | 709 ± 292 | 1.04 | 252 ± 15 | 1022 ± 175 | 1.41 | 460 ± 19 | 1858 ± 306 | 1.44 | 315 | | |
| 91 | S0780P349 | 77.99 | 34.86 | 3.20 | 188 ± 14 | 576 ± 140 | 1.22 | 181 ± 21 | 828 ± 110 | 1.50 | 373 ± 25 | 1490 ± 175 | 1.59 | 195 | | |

TABLE 1—Continued

| NUMBER | SHADOW NAME | COORDINATES ^a | | | BAND R1 | | | | BAND R2 | | | | BAND R12 | | | |
|--------|-------------|--------------------------|----------|-------------------|------------------------------------|------------------------------------|-----------------------------|------------------------------------|------------------------------------|-----------------------------|------------------------------------|------------------------------------|-----------------------------|------------------------------------|------------------------------------|-----------------------------|
| | | <i>l</i> | <i>b</i> | Size ^b | <i>I</i> ₀ ^c | <i>I</i> ₁ ^c | χ^2_{ν} ^d | <i>I</i> ₀ ^e | <i>I</i> ₁ ^e | χ^2_{ν} ^d | <i>I</i> ₀ ^e | <i>I</i> ₁ ^e | χ^2_{ν} ^d | <i>I</i> ₀ ^e | <i>I</i> ₁ ^e | χ^2_{ν} ^d |
| 92 | S0783P727 | 78.30 | 72.68 | 4.00 | 349 ± 21 | 141 ± 85 | 1.19 | 387 ± 32 | 275 ± 83 | 1.33 | 751 ± 38 | 427 ± 120 | 1.50 | 427 ± 120 | 1.50 | 315 |
| 93 | S0788M583 | 78.76 | -58.30 | 8.00 | 163 ± 11 | 391 ± 240 | 1.00 | 199 ± 16 | 364 ± 144 | 1.10 | 385 ± 20 | 704 ± 256 | 1.03 | 704 ± 256 | 1.03 | 1255 |
| 94 | S0795P457 | 79.47 | 45.68 | 3.20 | 191 ± 32 | 1551 ± 230 | 1.32 | 219 ± 50 | 1264 ± 195 | 1.46 | 419 ± 59 | 2745 ± 300 | 1.64 | 2745 ± 300 | 1.64 | 195 |
| 95 | S0802P420 | 80.23 | 42.04 | 3.20 | 284 ± 27 | 352 ± 258 | 1.10 | 273 ± 36 | 691 ± 177 | 1.44 | 565 ± 45 | 1220 ± 299 | 1.41 | 1220 ± 299 | 1.41 | 195 |
| 96 | S0806P375 | 80.56 | 37.45 | 3.20 | 185 ± 9 | 841 ± 89 | 1.46 | 204 ± 11 | 922 ± 64 | 1.82 | 393 ± 14 | 1794 ± 105 | 2.35 | 1794 ± 105 | 2.35 | 195 |
| 97 | S0815P690 | 81.48 | 68.95 | 4.00 | 332 ± 26 | 190 ± 85 | 1.40 | 470 ± 40 | <132 | 1.35 | 795 ± 46 | 247 ± 125 | 1.55 | 247 ± 125 | 1.55 | 315 |
| 98 | S0815P577 | 81.51 | 57.73 | 3.20 | 236 ± 21 | 503 ± 160 | 1.24 | 284 ± 31 | 455 ± 129 | 1.24 | 527 ± 38 | 952 ± 203 | 1.35 | 952 ± 203 | 1.35 | 195 |
| 99 | S0816P396 | 81.56 | 39.59 | 3.20 | 212 ± 10 | 911 ± 114 | 1.12 | 224 ± 13 | 891 ± 81 | 1.60 | 440 ± 16 | 1847 ± 135 | 1.62 | 1847 ± 135 | 1.62 | 195 |
| 100 | S0829M778 | 82.93 | -77.78 | 4.00 | 136 ± 24 | 446 ± 258 | 1.14 | 223 ± 35 | 218 ± 188 | 1.20 | 368 ± 43 | 675 ± 310 | 1.31 | 675 ± 310 | 1.31 | 314 |
| 101 | S0832M371 | 83.22 | -37.09 | 6.00 | 117 ± 5 | 292 ± 225 | 1.15 | 137 ± 7 | 372 ± 115 | 1.14 | 270 ± 9 | 691 ± 217 | 1.21 | 691 ± 217 | 1.21 | 704 |
| 102 | S0853P257 | 85.35 | 25.69 | 4.00 | 217 ± 8 | 697 ± 220 | 1.47 | 260 ± 11 | 859 ± 125 | 1.91 | 482 ± 14 | 1584 ± 224 | 2.30 | 1584 ± 224 | 2.30 | 315 |
| 103 | S0854M663 | 85.38 | -66.25 | 4.00 | 192 ± 7 | <292 | 1.16 | 222 ± 38 | <516 | 1.21 | 470 ± 48 | <468 | 1.24 | <468 | 1.24 | 316 |
| 104 | S0854M555 | 85.45 | -55.47 | 6.00 | 154 ± 9 | 699 ± 189 | 0.94 | 188 ± 11 | 409 ± 106 | 1.10 | 360 ± 15 | 993 ± 194 | 1.01 | 993 ± 194 | 1.01 | 706 |
| 105 | S0862P383 | 86.22 | 38.25 | 3.20 | 265 ± 27 | 474 ± 169 | 1.16 | 235 ± 39 | 844 ± 140 | 1.61 | 521 ± 48 | 1360 ± 218 | 1.88 | 1360 ± 218 | 1.88 | 187 |
| 106 | S0866P286 | 86.58 | 28.58 | 2.80 | 207 ± 10 | 1054 ± 216 | 1.44 | 252 ± 14 | 1005 ± 131 | 1.80 | 461 ± 17 | 2012 ± 228 | 2.19 | 2012 ± 228 | 2.19 | 147 |
| 107 | S0867P599 | 86.72 | 59.91 | 3.20 | 242 ± 17 | 444 ± 159 | 1.21 | 281 ± 24 | 475 ± 114 | 1.33 | 534 ± 30 | 903 ± 189 | 1.52 | 903 ± 189 | 1.52 | 195 |
| 108 | S0873P539 | 87.26 | 53.86 | 3.20 | 313 ± 32 | 424 ± 170 | 1.45 | 345 ± 48 | 503 ± 152 | 1.25 | 672 ± 57 | 927 ± 228 | 1.55 | 927 ± 228 | 1.55 | 195 |
| 109 | S0877P574 | 87.68 | 57.44 | 3.20 | 308 ± 20 | 457 ± 149 | 1.08 | 299 ± 28 | 637 ± 115 | 1.50 | 622 ± 35 | 1111 ± 184 | 1.49 | 1111 ± 184 | 1.49 | 195 |
| 110 | S0878P462 | 87.72 | -46.21 | 8.00 | 140 ± 4 | 752 ± 154 | 1.05 | 169 ± 5 | 420 ± 77 | 1.13 | 328 ± 7 | 807 ± 146 | 1.06 | 807 ± 146 | 1.06 | 1252 |
| 111 | S0878P361 | 87.76 | 36.09 | 2.80 | 183 ± 20 | 473 ± 171 | 1.19 | 158 ± 28 | 1092 ± 130 | 1.46 | 352 ± 34 | 1934 ± 209 | 1.55 | 1934 ± 209 | 1.55 | 147 |
| 112 | S0886P449 | 88.56 | 44.93 | 4.00 | 355 ± 18 | 490 ± 73 | 2.08 | 410 ± 28 | 564 ± 73 | 2.52 | 769 ± 33 | 1071 ± 104 | 3.58 | 1071 ± 104 | 3.58 | 315 |
| 113 | S0890P269 | 89.02 | 26.95 | 3.20 | 246 ± 10 | 294 ± 212 | 1.31 | 322 ± 15 | 317 ± 132 | 1.60 | 570 ± 18 | 604 ± 228 | 1.81 | 604 ± 228 | 1.81 | 195 |
| 114 | S0891M414 | 89.13 | -41.39 | 6.00 | 133 ± 4 | 646 ± 232 | 1.04 | 158 ± 5 | 475 ± 108 | 1.26 | 309 ± 7 | 1020 ± 209 | 1.13 | 1020 ± 209 | 1.13 | 705 |
| 115 | S0894P325 | 89.43 | 32.53 | 2.80 | 172 ± 9 | 1379 ± 174 | 2.01 | 199 ± 12 | 1155 ± 110 | 1.42 | 370 ± 15 | 2478 ± 189 | 2.24 | 2478 ± 189 | 2.24 | 147 |
| 116 | S0896P386 | 89.64 | 38.63 | 2.80 | 220 ± 11 | 1387 ± 84 | 1.70 | 259 ± 14 | 1357 ± 61 | 2.01 | 485 ± 18 | 2732 ± 100 | 2.68 | 2732 ± 100 | 2.68 | 147 |
| 117 | S0902M614 | 90.20 | -61.40 | 6.00 | 170 ± 15 | <306 | 1.07 | 195 ± 21 | 324 ± 151 | 1.17 | 387 ± 26 | 462 ± 261 | 1.12 | 462 ± 261 | 1.12 | 702 |
| 118 | S0906P315 | 90.56 | 31.49 | 2.80 | 200 ± 9 | 636 ± 160 | 1.83 | 232 ± 12 | 774 ± 100 | 1.81 | 437 ± 15 | 1421 ± 173 | 2.41 | 1421 ± 173 | 2.41 | 147 |
| 119 | S0915M325 | 91.48 | -32.53 | 3.60 | 151 ± 6 | 1090 ± 409 | 0.98 | 182 ± 7 | 660 ± 188 | 1.20 | 349 ± 10 | 1469 ± 363 | 1.07 | 1469 ± 363 | 1.07 | 251 |
| 120 | S0923P399 | 92.33 | 39.89 | 2.80 | 213 ± 10 | 1573 ± 100 | 1.97 | 236 ± 15 | 1617 ± 77 | 2.49 | 453 ± 18 | 3201 ± 123 | 3.28 | 3201 ± 123 | 3.28 | 147 |
| 121 | S0926P336 | 92.64 | 33.57 | 3.20 | 212 ± 14 | 441 ± 171 | 1.55 | 302 ± 21 | 260 ± 122 | 2.34 | 516 ± 25 | 634 ± 200 | 2.71 | 634 ± 200 | 2.71 | 195 |
| 122 | S0932P630 | 93.22 | 63.01 | 4.80 | 308 ± 21 | 348 ± 115 | 1.49 | 344 ± 30 | 377 ± 99 | 1.57 | 660 ± 36 | 744 ± 152 | 1.85 | 744 ± 152 | 1.85 | 439 |
| 123 | S0934P714 | 93.40 | 71.39 | 4.00 | 229 ± 25 | 560 ± 87 | 1.50 | 269 ± 39 | 536 ± 91 | 1.38 | 507 ± 45 | 1091 ± 127 | 1.94 | 1091 ± 127 | 1.94 | 315 |
| 124 | S0936P184 | 93.64 | 18.37 | 6.00 | 180 ± 4 | 2725 ± 313 | 1.20 | 213 ± 6 | 2543 ± 146 | 1.85 | 399 ± 7 | 5113 ± 278 | 2.02 | 5113 ± 278 | 2.02 | 707 |
| 125 | S0941P457 | 94.11 | 45.69 | 4.00 | 244 ± 24 | 1103 ± 103 | 1.78 | 220 ± 38 | 1243 ± 101 | 2.93 | 473 ± 44 | 2364 ± 145 | 3.67 | 2364 ± 145 | 3.67 | 315 |
| 126 | S0947P375 | 94.66 | 37.54 | 2.80 | 186 ± 12 | 1361 ± 140 | 1.80 | 207 ± 17 | 1437 ± 96 | 2.24 | 396 ± 21 | 2820 ± 160 | 3.01 | 2820 ± 160 | 3.01 | 147 |
| 127 | S0956P327 | 95.59 | 32.71 | 3.20 | 183 ± 8 | 810 ± 134 | 1.57 | 232 ± 11 | 804 ± 88 | 2.38 | 415 ± 14 | 1616 ± 149 | 2.87 | 1616 ± 149 | 2.87 | 195 |
| 128 | S0958M331 | 95.84 | -33.12 | 6.00 | 129 ± 4 | <801 | 1.01 | 161 ± 5 | 290 ± 185 | 1.17 | 305 ± 7 | 603 ± 362 | 1.16 | 603 ± 362 | 1.16 | 684 |
| 129 | S0959M554 | 95.89 | -55.40 | 6.00 | 143 ± 5 | 105 ± 91 | 1.03 | 166 ± 7 | 250 ± 57 | 1.18 | 325 ± 9 | 405 ± 99 | 1.20 | 405 ± 99 | 1.20 | 696 |
| 130 | S0971P265 | 97.07 | 26.49 | 3.20 | 187 ± 5 | <347 | 1.91 | 270 ± 3 | <45 | 4.32 | 460 ± 4 | <138 | 4.85 | <138 | 4.85 | 195 |
| 131 | S0980P234 | 98.01 | 23.41 | 6.00 | 165 ± 3 | 1986 ± 126 | 1.47 | 195 ± 4 | 2019 ± 66 | 2.59 | 365 ± 5 | 3983 ± 120 | 2.93 | 3983 ± 120 | 2.93 | 707 |
| 132 | S0983P327 | 98.33 | 32.66 | 3.20 | 213 ± 7 | 165 ± 144 | 1.76 | 308 ± 10 | 141 ± 92 | 2.63 | 520 ± 12 | 295 ± 157 | 3.26 | 295 ± 157 | 3.26 | 195 |
| 133 | S0996P366 | 99.59 | 36.61 | 3.20 | 219 ± 11 | 561 ± 190 | 1.81 | 246 ± 15 | 658 ± 118 | 2.63 | 468 ± 19 | 1244 ± 205 | 3.32 | 1244 ± 205 | 3.32 | 195 |
| 134 | S0999P672 | 99.92 | 67.21 | 4.80 | 355 ± 14 | 402 ± 63 | 1.16 | 325 ± 21 | 452 ± 61 | 1.19 | 634 ± 25 | 849 ± 88 | 1.42 | 849 ± 88 | 1.42 | 439 |
| 135 | S1000P520 | 100.04 | 52.04 | 8.00 | 293 ± 16 | 797 ± 60 | 1.77 | 313 ± 24 | 862 ± 59 | 1.87 | 678 ± 28 | 1662 ± 84 | 2.63 | 1662 ± 84 | 2.63 | 1255 |
| 136 | S1001M607 | 100.15 | -60.73 | 3.20 | 152 ± 12 | <269 | 0.98 | 183 ± 28 | 218 ± 184 | 1.19 | 355 ± 36 | <600 | 1.06 | <600 | 1.06 | 192 |
| 137 | S1007M421 | 100.71 | -42.09 | 6.00 | 115 ± 5 | <210 | 0.98 | 141 ± 6 | 270 ± 76 | 1.01 | 272 ± 8 | 384 ± 138 | 1.07 | 384 ± 138 | 1.07 | 681 |

TABLE 1—Continued

| NUMBER | SHADOW NAME | COORDINATES ^a | | | BAND R1 | | | | BAND R2 | | | | BAND R12 | | | | v ^c |
|--------|-------------|--------------------------|--------|-------------------|-----------------------------|-----------------------------|-------------------------------|-----------------------------|-----------------------------|-------------------------------|-----------------------------|-----------------------------|-------------------------------|-----------------------------|-----------------------------|-------------------------------|----------------|
| | | l | b | Size ^b | I ₀ ^c | I ₁ ^c | χ _v ^{2,d} | I ₀ ^c | I ₁ ^c | χ _v ^{2,d} | I ₀ ^c | I ₁ ^c | χ _v ^{2,d} | I ₀ ^c | I ₁ ^c | χ _v ^{2,d} | |
| 138 | S100P423 | 100.82 | 42.31 | 3.20 | 181 ± 20 | 1848 ± 274 | 2.53 | 141 ± 28 | 1599 ± 181 | 3.54 | 326 ± 35 | 3380 ± 307 | 4.92 | 3380 ± 307 | 4.92 | 195 | |
| 139 | S1011P274 | 101.08 | 27.44 | 3.20 | 188 ± 8 | 1004 ± 382 | 1.97 | 235 ± 10 | 446 ± 184 | 2.26 | 424 ± 13 | 1216 ± 348 | 3.02 | 1216 ± 348 | 3.02 | 195 | |
| 140 | S1018P453 | 101.77 | 45.25 | 4.00 | 267 ± 14 | 726 ± 119 | 1.50 | 245 ± 21 | 759 ± 91 | 2.01 | 507 ± 25 | 1561 ± 146 | 2.39 | 1561 ± 146 | 2.39 | 315 | |
| 141 | S1021M291 | 102.10 | -29.06 | 6.00 | 110 ± 3 | <839 | 1.13 | 128 ± 4 | 665 ± 237 | 1.14 | 253 ± 6 | 1021 ± 475 | 1.18 | 1021 ± 475 | 1.18 | 694 | |
| 142 | S1041P421 | 104.07 | 42.13 | 3.20 | 211 ± 17 | 802 ± 197 | 1.56 | 247 ± 24 | 530 ± 134 | 1.69 | 456 ± 30 | 1285 ± 226 | 2.01 | 1285 ± 226 | 2.01 | 195 | |
| 143 | S1044M628 | 104.40 | -62.80 | 3.20 | 154 ± 13 | <237 | 0.98 | 154 ± 31 | 401 ± 190 | 1.07 | 339 ± 40 | 422 ± 330 | 1.02 | 422 ± 330 | 1.02 | 194 | |
| 144 | S1050P360 | 104.99 | 36.02 | 3.20 | 189 ± 12 | 453 ± 199 | 1.46 | 217 ± 16 | 345 ± 120 | 1.39 | 410 ± 20 | 742 ± 210 | 1.73 | 742 ± 210 | 1.73 | 195 | |
| 145 | S1061P324 | 106.11 | 32.44 | 3.20 | 148 ± 17 | 1299 ± 362 | 1.19 | 179 ± 23 | 843 ± 215 | 1.39 | 328 ± 29 | 1984 ± 378 | 1.42 | 1984 ± 378 | 1.42 | 195 | |
| 146 | S1062M432 | 106.20 | -43.20 | 8.00 | 108 ± 4 | <152 | 1.00 | 133 ± 5 | 212 ± 52 | 1.10 | 257 ± 6 | 329 ± 93 | 1.09 | 329 ± 93 | 1.09 | 1195 | |
| 147 | S1062P753 | 106.21 | 75.28 | 4.00 | 247 ± 35 | 578 ± 163 | 1.28 | 272 ± 54 | 569 ± 152 | 1.62 | 536 ± 63 | 1119 ± 224 | 1.86 | 1119 ± 224 | 1.86 | 315 | |
| 148 | S1076M374 | 107.62 | -37.37 | 6.00 | 116 ± 5 | 376 ± 212 | 0.99 | 134 ± 6 | 358 ± 108 | 1.05 | 265 ± 8 | 814 ± 204 | 1.04 | 814 ± 204 | 1.04 | 646 | |
| 149 | S1081P696 | 108.08 | 69.59 | 4.80 | 314 ± 14 | 254 ± 62 | 1.28 | 348 ± 20 | 320 ± 56 | 1.45 | 677 ± 25 | 575 ± 84 | 1.66 | 575 ± 84 | 1.66 | 439 | |
| 150 | S1084M543 | 108.43 | -54.33 | 4.00 | 114 ± 5 | 145 ± 93 | 1.04 | 128 ± 6 | 320 ± 55 | 1.06 | 253 ± 8 | 557 ± 98 | 1.11 | 557 ± 98 | 1.11 | 312 | |
| 151 | S1090P463 | 109.03 | 46.32 | 3.20 | 366 ± 20 | 209 ± 131 | 1.32 | 447 ± 29 | 112 ± 107 | 1.45 | 816 ± 36 | 303 ± 167 | 1.76 | 303 ± 167 | 1.76 | 195 | |
| 152 | S1093P590 | 109.26 | 59.01 | 4.00 | 390 ± 50 | 457 ± 139 | 1.44 | 564 ± 80 | 191 ± 157 | 1.42 | 942 ± 91 | 661 ± 210 | 1.64 | 661 ± 210 | 1.64 | 315 | |
| 153 | S1093P338 | 109.34 | 33.75 | 3.20 | 208 ± 23 | <715 | 1.31 | 264 ± 32 | <440 | 1.23 | 480 ± 40 | <838 | 1.52 | <838 | 1.52 | 195 | |
| 154 | S1102M225 | 110.18 | -22.51 | 8.00 | 127 ± 4 | <1516 | 0.81 | 140 ± 5 | 434 ± 311 | 0.94 | 284 ± 7 | 1144 ± 637 | 0.93 | 1144 ± 637 | 0.93 | 1118 | |
| 155 | S1120P849 | 112.01 | 84.93 | 4.00 | 275 ± 51 | 360 ± 220 | 1.15 | 136 ± 78 | 845 ± 211 | 1.13 | 463 ± 92 | 1184 ± 308 | 1.31 | 1184 ± 308 | 1.31 | 315 | |
| 156 | S1127P381 | 112.67 | 38.15 | 3.60 | 202 ± 18 | 338 ± 229 | 1.20 | 262 ± 26 | 199 ± 156 | 1.22 | 476 ± 33 | 442 ± 263 | 1.20 | 442 ± 263 | 1.20 | 251 | |
| 157 | S1131P729 | 113.11 | 72.87 | 6.00 | 284 ± 17 | 257 ± 90 | 1.13 | 339 ± 25 | 233 ± 78 | 1.26 | 633 ± 30 | 489 ± 119 | 1.33 | 489 ± 119 | 1.33 | 707 | |
| 158 | S1137M311 | 113.72 | -31.06 | 6.00 | 109 ± 8 | 380 ± 265 | 0.82 | 116 ± 11 | 520 ± 141 | 1.01 | 243 ± 14 | 952 ± 262 | 0.96 | 952 ± 262 | 0.96 | 626 | |
| 159 | S1145P499 | 114.54 | 49.94 | 3.20 | 535 ± 31 | <252 | 1.10 | 558 ± 41 | <204 | 1.07 | 1102 ± 51 | <346 | 1.25 | <346 | 1.25 | 195 | |
| 160 | S1152P362 | 115.23 | 36.20 | 3.20 | 247 ± 12 | <280 | 1.09 | 308 ± 38 | <266 | 1.24 | 573 ± 47 | <387 | 1.13 | <387 | 1.13 | 196 | |
| 161 | S1165P621 | 116.47 | 62.13 | 4.80 | 308 ± 24 | 357 ± 126 | 1.36 | 366 ± 36 | 355 ± 112 | 1.41 | 695 ± 43 | 678 ± 169 | 1.69 | 678 ± 169 | 1.69 | 439 | |
| 162 | S1175M537 | 117.50 | -53.66 | 6.00 | 119 ± 5 | 146 ± 133 | 0.90 | 135 ± 6 | 269 ± 81 | 1.03 | 269 ± 8 | 536 ± 145 | 1.12 | 536 ± 145 | 1.12 | 646 | |
| 163 | S1173P541 | 117.51 | 54.13 | 6.00 | 361 ± 17 | 266 ± 93 | 1.53 | 372 ± 25 | 333 ± 80 | 1.51 | 743 ± 30 | 617 ± 122 | 1.95 | 617 ± 122 | 1.95 | 707 | |
| 164 | S1176M681 | 117.62 | -68.08 | 14.00 | 137 ± 3 | 297 ± 45 | 1.12 | 143 ± 4 | 469 ± 29 | 1.19 | 299 ± 5 | 822 ± 51 | 1.26 | 822 ± 51 | 1.26 | 3797 | |
| 165 | S1179M389 | 117.86 | -38.89 | 8.00 | 130 ± 5 | <108 | 0.98 | 146 ± 10 | 313 ± 79 | 1.18 | 293 ± 12 | 430 ± 136 | 1.18 | 430 ± 136 | 1.18 | 1205 | |
| 166 | S1179P409 | 117.91 | 40.87 | 4.00 | 306 ± 14 | 196 ± 140 | 1.43 | 360 ± 19 | 212 ± 102 | 1.26 | 673 ± 24 | 402 ± 167 | 1.66 | 402 ± 167 | 1.66 | 315 | |
| 167 | S1182M459 | 118.17 | -45.93 | 4.00 | 130 ± 10 | <406 | 0.70 | 134 ± 12 | 239 ± 165 | 0.92 | 282 ± 16 | 344 ± 313 | 0.80 | 344 ± 313 | 0.80 | 288 | |
| 168 | S1231P714 | 123.09 | 71.42 | 4.00 | 271 ± 21 | 671 ± 111 | 1.34 | 276 ± 29 | 632 ± 92 | 1.26 | 555 ± 35 | 1320 ± 143 | 1.51 | 1320 ± 143 | 1.51 | 315 | |
| 169 | S1240P515 | 123.98 | 51.53 | 3.20 | 426 ± 11 | <219 | 1.39 | 489 ± 12 | <57 | 1.43 | 928 ± 16 | <114 | 1.66 | <114 | 1.66 | 196 | |
| 170 | S1250P367 | 125.02 | 36.69 | 8.00 | 201 ± 4 | 749 ± 96 | 1.12 | 210 ± 4 | 685 ± 52 | 1.11 | 425 ± 6 | 1405 ± 96 | 1.21 | 1405 ± 96 | 1.21 | 1253 | |
| 171 | S1253M558 | 125.34 | -55.78 | 6.00 | 114 ± 6 | 182 ± 103 | 0.95 | 138 ± 8 | 223 ± 65 | 1.19 | 269 ± 11 | 433 ± 114 | 1.13 | 433 ± 114 | 1.13 | 677 | |
| 172 | S1285M259 | 128.48 | -25.86 | 6.00 | 139 ± 10 | <623 | 1.08 | 141 ± 13 | 806 ± 179 | 1.28 | 306 ± 18 | 1195 ± 338 | 1.18 | 1195 ± 338 | 1.18 | 706 | |
| 173 | S1291P435 | 129.08 | 43.52 | 4.80 | 294 ± 9 | 614 ± 69 | 1.41 | 320 ± 11 | 385 ± 46 | 1.45 | 623 ± 14 | 933 ± 79 | 1.82 | 933 ± 79 | 1.82 | 439 | |
| 174 | S1298M355 | 129.84 | -38.53 | 6.00 | 130 ± 3 | <61 | 0.97 | 147 ± 8 | 176 ± 118 | 1.00 | 303 ± 9 | <222 | 1.03 | <222 | 1.03 | 689 | |
| 175 | S1302P680 | 130.17 | 68.01 | 4.00 | 348 ± 49 | <367 | 1.27 | 342 ± 76 | 381 ± 214 | 1.14 | 721 ± 89 | 527 ± 311 | 1.44 | 527 ± 311 | 1.44 | 315 | |
| 176 | S1341M637 | 134.07 | -63.75 | 6.00 | 136 ± 4 | <70 | 1.05 | 156 ± 12 | 136 ± 92 | 1.09 | 317 ± 16 | <280 | 1.08 | <280 | 1.08 | 689 | |
| 177 | S1348M298 | 134.81 | -29.78 | 6.00 | 151 ± 4 | <142 | 1.13 | 127 ± 20 | 869 ± 234 | 1.08 | 314 ± 26 | 999 ± 433 | 1.09 | 999 ± 433 | 1.09 | 702 | |
| 178 | S1348P407 | 134.83 | 40.69 | 6.00 | 298 ± 7 | 260 ± 127 | 1.30 | 312 ± 8 | 344 ± 74 | 1.19 | 632 ± 11 | 596 ± 134 | 1.40 | 596 ± 134 | 1.40 | 704 | |
| 179 | S1350P292 | 134.97 | 29.22 | 6.00 | 193 ± 10 | 184 ± 134 | 1.13 | 184 ± 13 | 479 ± 89 | 1.13 | 392 ± 17 | 763 ± 152 | 1.24 | 763 ± 152 | 1.24 | 707 | |
| 180 | S1353M597 | 135.27 | -59.67 | 4.00 | 125 ± 8 | <208 | 1.01 | 154 ± 22 | <281 | 1.24 | 296 ± 28 | <428 | 1.22 | <428 | 1.22 | 313 | |
| 181 | S1359P512 | 135.85 | 51.22 | 4.00 | 316 ± 16 | 263 ± 71 | 1.20 | 304 ± 20 | 254 ± 57 | 1.45 | 635 ± 26 | 502 ± 90 | 1.52 | 502 ± 90 | 1.52 | 315 | |
| 182 | S1359P548 | 135.94 | 54.80 | 4.00 | 281 ± 14 | 385 ± 95 | 1.12 | 285 ± 18 | 340 ± 70 | 1.20 | 578 ± 24 | 720 ± 115 | 1.20 | 720 ± 115 | 1.20 | 315 | |
| 183 | S1361P745 | 136.05 | 74.54 | 6.00 | 342 ± 18 | 335 ± 110 | 1.16 | 357 ± 26 | 383 ± 91 | 1.44 | 713 ± 31 | 724 ± 141 | 1.67 | 724 ± 141 | 1.67 | 707 | |

| NUMBER | SHADOW NAME | COORDINATES ^a | | | | BAND R1 | | | | BAND R2 | | | | BAND R12 | | | |
|--------|-------------|--------------------------|----------|-------------------|------------------------------------|------------------------------------|----------------|------------------------------------|------------------------------------|----------------|------------------------------------|------------------------------------|----------------|------------------------------------|------------------------------------|----------------|---------|
| | | <i>l</i> | <i>b</i> | Size ^b | <i>I</i> ₀ ^c | <i>I</i> ₁ ^c | χ^2_{ν} | <i>I</i> ₀ ^c | <i>I</i> ₁ ^c | χ^2_{ν} | <i>I</i> ₀ ^c | <i>I</i> ₁ ^c | χ^2_{ν} | <i>I</i> ₀ ^c | <i>I</i> ₁ ^c | χ^2_{ν} | ν^e |
| 184 | S1361M467 | 136.15 | -46.68 | 6.00 | 133 ± 6 | 275 ± 187 | 1.09 | 153 ± 7 | 188 ± 96 | 1.13 | 303 ± 10 | 431 ± 182 | 1.19 | 303 ± 10 | 431 ± 182 | 1.19 | 695 |
| 185 | S1369P461 | 136.89 | 46.06 | 3.20 | 284 ± 35 | 279 ± 180 | 1.01 | 227 ± 52 | 503 ± 157 | 1.24 | 534 ± 62 | 783 ± 238 | 1.33 | 534 ± 62 | 783 ± 238 | 1.33 | 195 |
| 186 | S1373P585 | 137.34 | 58.47 | 4.00 | 301 ± 22 | 266 ± 102 | 1.28 | 336 ± 31 | 276 ± 89 | 1.49 | 660 ± 38 | 516 ± 136 | 1.58 | 660 ± 38 | 516 ± 136 | 1.58 | 315 |
| 187 | S1378M519 | 137.82 | -51.92 | 6.00 | 134 ± 3 | <42 | 1.11 | 160 ± 3 | <22 | 1.21 | 315 ± 5 | <42 | 1.21 | 315 ± 5 | <42 | 1.21 | 703 |
| 188 | S1382M397 | 138.21 | -39.74 | 6.00 | 154 ± 5 | <433 | 0.95 | 164 ± 7 | 242 ± 149 | 0.98 | 336 ± 9 | 340 ± 290 | 1.02 | 336 ± 9 | 340 ± 290 | 1.02 | 704 |
| 189 | S1394M695 | 139.37 | -69.47 | 8.00 | 153 ± 5 | 171 ± 113 | 1.01 | 168 ± 6 | 190 ± 60 | 1.19 | 343 ± 8 | 343 ± 113 | 1.16 | 343 ± 8 | 343 ± 113 | 1.16 | 1231 |
| 190 | S1412P350 | 141.20 | 34.99 | 3.20 | 221 ± 13 | 248 ± 186 | 1.01 | 238 ± 15 | 168 ± 107 | 1.26 | 478 ± 20 | 397 ± 194 | 1.16 | 478 ± 20 | 397 ± 194 | 1.16 | 195 |
| 191 | S1414P485 | 141.41 | 48.54 | 3.20 | 335 ± 18 | <151 | 1.30 | 290 ± 22 | 263 ± 67 | 1.50 | 637 ± 29 | 367 ± 105 | 1.78 | 637 ± 29 | 367 ± 105 | 1.78 | 195 |
| 192 | S1427P816 | 142.72 | 81.57 | 4.80 | 241 ± 32 | 559 ± 151 | 1.25 | 282 ± 51 | 562 ± 146 | 1.31 | 523 ± 60 | 1164 ± 212 | 1.52 | 523 ± 60 | 1164 ± 212 | 1.52 | 439 |
| 193 | S1436P653 | 143.65 | 65.35 | 8.00 | 254 ± 14 | 499 ± 93 | 1.33 | 297 ± 21 | 364 ± 75 | 1.31 | 571 ± 25 | 822 ± 119 | 1.55 | 571 ± 25 | 822 ± 119 | 1.55 | 1255 |
| 194 | S1444P502 | 144.39 | 50.22 | 4.00 | 291 ± 29 | 212 ± 95 | 1.25 | 239 ± 41 | 361 ± 92 | 1.53 | 553 ± 50 | 572 ± 134 | 1.70 | 553 ± 50 | 572 ± 134 | 1.70 | 315 |
| 195 | S1456M579 | 145.56 | -57.94 | 4.80 | 147 ± 5 | <45 | 1.22 | 185 ± 24 | <200 | 1.27 | 373 ± 9 | <84 | 1.18 | 373 ± 9 | <84 | 1.18 | 438 |
| 196 | S1463P442 | 146.35 | 44.22 | 4.00 | 346 ± 9 | <95 | 1.20 | 325 ± 10 | 183 ± 51 | 1.18 | 687 ± 14 | 225 ± 84 | 1.43 | 687 ± 14 | 225 ± 84 | 1.43 | 315 |
| 197 | S1519P503 | 151.92 | 50.34 | 3.20 | 214 ± 38 | 500 ± 107 | 1.47 | 311 ± 57 | 240 ± 112 | 1.42 | 529 ± 67 | 715 ± 156 | 1.85 | 529 ± 67 | 715 ± 156 | 1.85 | 195 |
| 198 | S1533P367 | 153.29 | 36.72 | 4.00 | 267 ± 10 | <388 | 0.98 | 254 ± 11 | <404 | 1.19 | 546 ± 15 | <525 | 1.11 | 546 ± 15 | <525 | 1.11 | 316 |
| 199 | S1556P502 | 155.60 | 50.23 | 3.20 | 308 ± 34 | 238 ± 107 | 1.12 | 254 ± 46 | 388 ± 101 | 1.36 | 580 ± 57 | 648 ± 148 | 1.31 | 580 ± 57 | 648 ± 148 | 1.31 | 195 |
| 200 | S1559P741 | 155.85 | 74.06 | 4.00 | 296 ± 27 | 354 ± 165 | 1.19 | 284 ± 39 | 521 ± 137 | 1.34 | 613 ± 48 | 877 ± 215 | 1.33 | 613 ± 48 | 877 ± 215 | 1.33 | 315 |
| 201 | S1571P532 | 157.05 | 53.21 | 3.20 | 292 ± 28 | 315 ± 121 | 1.36 | 316 ± 40 | 251 ± 109 | 1.15 | 609 ± 48 | 588 ± 163 | 1.43 | 609 ± 48 | 588 ± 163 | 1.43 | 195 |
| 202 | S1596P436 | 159.64 | 43.63 | 4.00 | 317 ± 21 | <217 | 0.94 | 307 ± 27 | <217 | 1.10 | 643 ± 35 | <323 | 1.09 | 643 ± 35 | <323 | 1.09 | 315 |
| 203 | S1601P618 | 160.14 | 61.75 | 6.00 | 315 ± 23 | 548 ± 104 | 1.22 | 297 ± 34 | 594 ± 95 | 1.19 | 630 ± 40 | 1143 ± 141 | 1.38 | 630 ± 40 | 1143 ± 141 | 1.38 | 707 |
| 204 | S1603P554 | 160.29 | 55.38 | 3.20 | 307 ± 34 | 436 ± 167 | 1.33 | 351 ± 48 | 260 ± 142 | 1.42 | 660 ± 59 | 688 ± 218 | 1.67 | 660 ± 59 | 688 ± 218 | 1.67 | 195 |
| 205 | S1621P681 | 162.06 | 68.11 | 3.20 | 346 ± 65 | <954 | 1.19 | 450 ± 21 | <394 | 1.17 | 824 ± 116 | <942 | 1.10 | 824 ± 116 | <942 | 1.10 | 195 |
| 206 | S1637M681 | 163.73 | -68.10 | 4.80 | 156 ± 20 | 244 ± 184 | 1.17 | 139 ± 28 | 426 ± 136 | 1.23 | 312 ± 35 | 746 ± 224 | 1.28 | 312 ± 35 | 746 ± 224 | 1.28 | 438 |
| 207 | S1664M870 | 166.43 | -87.02 | 4.00 | 166 ± 28 | 214 ± 201 | 1.01 | 147 ± 39 | 506 ± 154 | 1.23 | 357 ± 49 | 694 ± 251 | 1.19 | 357 ± 49 | 694 ± 251 | 1.19 | 312 |
| 208 | S1685P473 | 168.53 | 47.28 | 3.20 | 303 ± 32 | 197 ± 146 | 1.13 | 314 ± 45 | 159 ± 128 | 1.18 | 625 ± 55 | 364 ± 194 | 1.25 | 625 ± 55 | 364 ± 194 | 1.25 | 194 |
| 209 | S1699M791 | 169.93 | -79.12 | 3.20 | 187 ± 26 | 356 ± 194 | 1.14 | 159 ± 35 | 465 ± 144 | 1.55 | 362 ± 44 | 899 ± 237 | 1.41 | 362 ± 44 | 899 ± 237 | 1.41 | 195 |
| 210 | S1700P578 | 170.03 | 57.80 | 4.80 | 346 ± 24 | 419 ± 120 | 1.29 | 406 ± 36 | 286 ± 108 | 1.29 | 765 ± 43 | 674 ± 161 | 1.48 | 765 ± 43 | 674 ± 161 | 1.48 | 439 |
| 211 | S1720P706 | 171.95 | 70.62 | 3.20 | 300 ± 45 | <645 | 1.38 | 348 ± 68 | <536 | 1.12 | 694 ± 84 | <878 | 1.28 | 694 ± 84 | <878 | 1.28 | 195 |
| 212 | S1763P474 | 176.28 | 47.44 | 4.00 | 330 ± 28 | 348 ± 142 | 1.13 | 292 ± 41 | 437 ± 125 | 1.35 | 623 ± 50 | 850 ± 189 | 1.55 | 623 ± 50 | 850 ± 189 | 1.55 | 315 |
| 213 | S1768M593 | 176.79 | -59.29 | 4.00 | 179 ± 32 | <451 | 1.14 | 178 ± 45 | <484 | 1.52 | 356 ± 56 | 543 ± 441 | 1.70 | 356 ± 56 | 543 ± 441 | 1.70 | 314 |
| 214 | S1770M651 | 176.99 | -65.07 | 4.80 | 127 ± 35 | 375 ± 294 | 1.00 | 180 ± 51 | <373 | 1.18 | 329 ± 63 | 439 ± 361 | 1.19 | 329 ± 63 | 439 ± 361 | 1.19 | 435 |
| 215 | S1789P647 | 178.86 | 64.69 | 4.00 | 362 ± 10 | <137 | 0.95 | 391 ± 11 | <79 | 16.39 | 767 ± 15 | <118 | 23.30 | 767 ± 15 | <118 | 23.30 | 316 |
| 216 | S1789P535 | 178.88 | 53.48 | 6.00 | 448 ± 6 | <69 | 1.37 | 506 ± 7 | <50 | 1.66 | 969 ± 9 | <53 | 1.85 | 969 ± 9 | <53 | 708 | |
| 217 | S1792M827 | 179.22 | -82.69 | 4.00 | 174 ± 30 | 220 ± 197 | 1.38 | 62 ± 44 | 755 ± 163 | 1.40 | 254 ± 54 | 1119 ± 255 | 1.68 | 254 ± 54 | 1119 ± 255 | 1.68 | 315 |
| 218 | S1839P302 | 183.91 | 30.23 | 3.20 | 159 ± 28 | 1566 ± 976 | 1.18 | 196 ± 35 | 490 ± 477 | 1.06 | 393 ± 47 | 1210 ± 921 | 1.24 | 393 ± 47 | 1210 ± 921 | 1.24 | 195 |
| 219 | S1860P403 | 186.03 | 40.28 | 4.00 | 167 ± 23 | 541 ± 280 | 0.91 | 180 ± 35 | 379 ± 200 | 0.99 | 365 ± 42 | 857 ± 332 | 0.99 | 365 ± 42 | 857 ± 332 | 0.99 | 307 |
| 220 | S1861M721 | 186.13 | -72.13 | 4.80 | 153 ± 15 | 359 ± 104 | 1.17 | 177 ± 22 | 306 ± 84 | 1.42 | 348 ± 27 | 637 ± 133 | 1.46 | 348 ± 27 | 637 ± 133 | 1.46 | 439 |
| 221 | S1863P325 | 186.26 | 32.49 | 4.00 | 195 ± 11 | <845 | 1.21 | 172 ± 27 | 492 ± 399 | 1.15 | 368 ± 36 | 1204 ± 787 | 1.35 | 368 ± 36 | 1204 ± 787 | 1.35 | 314 |
| 222 | S1868P600 | 186.77 | 59.95 | 4.80 | 427 ± 31 | 457 ± 165 | 1.41 | 356 ± 46 | 754 ± 145 | 1.53 | 810 ± 56 | 1244 ± 220 | 1.86 | 810 ± 56 | 1244 ± 220 | 1.86 | 439 |
| 223 | S1888P737 | 188.83 | 73.65 | 4.80 | 193 ± 42 | 1001 ± 321 | 1.00 | 173 ± 61 | 850 ± 248 | 1.17 | 387 ± 76 | 1817 ± 400 | 1.11 | 387 ± 76 | 1817 ± 400 | 1.11 | 439 |
| 224 | S1911P696 | 191.09 | 69.61 | 4.00 | 297 ± 34 | 260 ± 254 | 1.20 | 299 ± 49 | 306 ± 198 | 1.34 | 638 ± 60 | 520 ± 318 | 1.25 | 638 ± 60 | 520 ± 318 | 1.25 | 315 |
| 225 | S1917P565 | 191.72 | 56.54 | 4.00 | 342 ± 32 | 605 ± 158 | 1.44 | 376 ± 46 | 447 ± 139 | 1.48 | 731 ± 56 | 1024 ± 211 | 1.83 | 731 ± 56 | 1024 ± 211 | 1.83 | 315 |
| 226 | S1923M679 | 192.33 | -67.85 | 4.00 | 228 ± 11 | <189 | 1.56 | 247 ± 25 | <266 | 1.33 | 495 ± 32 | <474 | 1.62 | 495 ± 32 | <474 | 1.62 | 316 |
| 227 | S1947P657 | 194.67 | 65.73 | 4.00 | 368 ± 34 | <312 | 1.15 | 361 ± 48 | 281 ± 199 | 1.29 | 763 ± 59 | 324 ± 323 | 1.49 | 763 ± 59 | 324 ± 323 | 1.49 | 315 |
| 228 | S1969M646 | 196.85 | -64.61 | 3.20 | 322 ± 13 | <199 | 1.35 | 289 ± 43 | <471 | 1.11 | 653 ± 56 | <592 | 1.39 | 653 ± 56 | <592 | 1.39 | 195 |
| 229 | S1983P357 | 198.26 | 35.67 | 4.00 | 184 ± 28 | <666 | 0.90 | 193 ± 39 | <696 | 0.97 | 392 ± 50 | <1180 | 1.06 | 392 ± 50 | <1180 | 1.06 | 302 |

TABLE 1—Continued

| NUMBER | SHADOW NAME | COORDINATES ^a | | | BAND R1 | | | | BAND R2 | | | | BAND R12 | | | |
|--------|-------------|--------------------------|----------|-------------------|------------------------------------|------------------------------------|-------------------------|------------------------------------|------------------------------------|-------------------------|------------------------------------|------------------------------------|-------------------------|------------------------------------|------------------------------------|-------------------------|
| | | <i>l</i> | <i>b</i> | Size ^b | <i>I</i> ₀ ^c | <i>I</i> ₁ ^c | χ^2_v ^d | <i>I</i> ₀ ^c | <i>I</i> ₁ ^c | χ^2_v ^d | <i>I</i> ₀ ^c | <i>I</i> ₁ ^c | χ^2_v ^d | <i>I</i> ₀ ^c | <i>I</i> ₁ ^c | χ^2_v ^d |
| 230 | S1984P321 | 198.37 | 32.14 | 3.20 | 190 ± 20 | <728 | 1.20 | 224 ± 25 | 238 ± 213 | 1.10 | 453 ± 33 | 1.10 | 453 ± 33 | <761 | 1.10 | 195 |
| 231 | S1985P565 | 198.54 | 56.51 | 4.80 | 363 ± 24 | 341 ± 224 | 1.11 | 441 ± 34 | <280 | 1.25 | 814 ± 42 | 1.25 | 814 ± 42 | 420 ± 265 | 1.43 | 439 |
| 232 | S2016P421 | 201.55 | 42.06 | 8.00 | 156 ± 8 | 947 ± 96 | 1.08 | 136 ± 11 | 890 ± 65 | 1.30 | 311 ± 14 | 1.30 | 311 ± 14 | 1816 ± 110 | 1.28 | 1247 |
| 233 | S2020P849 | 202.01 | 84.93 | 4.80 | 265 ± 29 | 563 ± 192 | 1.25 | 305 ± 43 | 474 ± 160 | 1.45 | 591 ± 52 | 1.45 | 591 ± 52 | 977 ± 248 | 1.58 | 439 |
| 234 | S2030M805 | 203.04 | -80.54 | 3.20 | 179 ± 33 | 216 ± 160 | 1.17 | 104 ± 47 | 527 ± 138 | 1.34 | 322 ± 58 | 1.34 | 322 ± 58 | 742 ± 213 | 1.31 | 195 |
| 235 | S2043P662 | 204.28 | 66.24 | 4.00 | 378 ± 35 | 410 ± 285 | 1.07 | 378 ± 48 | 441 ± 208 | 1.11 | 769 ± 60 | 1.11 | 769 ± 60 | 915 ± 342 | 1.19 | 315 |
| 236 | S2045M738 | 204.50 | -73.79 | 3.20 | 233 ± 47 | <286 | 1.17 | 187 ± 70 | 310 ± 218 | 1.45 | 448 ± 85 | 1.45 | 448 ± 85 | 351 ± 332 | 1.72 | 195 |
| 237 | S2061M627 | 206.09 | -62.69 | 4.80 | 349 ± 9 | <147 | 1.43 | 359 ± 9 | <75 | 1.28 | 731 ± 11 | 1.28 | 731 ± 11 | <111 | 1.69 | 440 |
| 238 | S2062M520 | 206.22 | -51.96 | 3.20 | 234 ± 16 | 1454 ± 531 | 1.16 | 179 ± 16 | 627 ± 223 | 1.25 | 435 ± 23 | 1.25 | 435 ± 23 | 1929 ± 462 | 1.32 | 194 |
| 239 | S2070P734 | 207.03 | 73.44 | 4.00 | 249 ± 62 | <906 | 1.17 | 201 ± 91 | 670 ± 380 | 1.36 | 502 ± 111 | 1.36 | 502 ± 111 | 1002 ± 610 | 1.46 | 315 |
| 240 | S2081P503 | 208.08 | 50.34 | 8.00 | 266 ± 11 | <144 | 1.19 | 306 ± 16 | 131 ± 84 | 1.25 | 593 ± 20 | 1.25 | 593 ± 20 | 151 ± 141 | 1.38 | 1255 |
| 241 | S2098P617 | 209.77 | 61.72 | 6.00 | 371 ± 15 | 445 ± 138 | 1.18 | 440 ± 21 | 220 ± 100 | 1.27 | 830 ± 26 | 1.27 | 830 ± 26 | 583 ± 162 | 1.43 | 707 |
| 242 | S2107P443 | 210.65 | 44.28 | 4.80 | 187 ± 14 | 412 ± 197 | 1.08 | 211 ± 20 | 443 ± 130 | 1.12 | 410 ± 25 | 1.12 | 410 ± 25 | 896 ± 222 | 1.16 | 439 |
| 243 | S2128M511 | 212.82 | -51.06 | 3.20 | 219 ± 17 | 704 ± 286 | 1.12 | 191 ± 20 | 503 ± 160 | 1.39 | 420 ± 27 | 1.39 | 420 ± 27 | 1298 ± 295 | 1.37 | 194 |
| 244 | S2151P263 | 215.08 | 26.33 | 3.20 | 239 ± 19 | <651 | 1.17 | 228 ± 24 | 707 ± 199 | 1.08 | 479 ± 31 | 1.08 | 479 ± 31 | 1369 ± 354 | 1.11 | 194 |
| 245 | S2156P371 | 215.59 | 37.11 | 6.00 | 201 ± 11 | 181 ± 142 | 1.21 | 209 ± 15 | 427 ± 97 | 1.14 | 437 ± 19 | 1.14 | 437 ± 19 | 617 ± 164 | 1.31 | 707 |
| 246 | S2184M789 | 218.42 | -78.88 | 4.00 | 218 ± 48 | <324 | 1.18 | 243 ± 70 | <290 | 1.49 | 493 ± 85 | 1.49 | 493 ± 85 | <412 | 1.54 | 315 |
| 247 | S2194M696 | 219.41 | -69.57 | 4.00 | 411 ± 9 | <74 | 1.34 | 440 ± 10 | <178 | 1.02 | 870 ± 14 | 1.02 | 870 ± 14 | <98 | 1.24 | 316 |
| 248 | S2195M494 | 219.49 | -49.37 | 3.20 | 231 ± 18 | 614 ± 139 | 1.13 | 221 ± 24 | 571 ± 106 | 1.14 | 471 ± 30 | 1.14 | 471 ± 30 | 1173 ± 172 | 1.28 | 195 |
| 249 | S2198P745 | 219.76 | 74.47 | 3.20 | 311 ± 35 | <635 | 0.86 | 349 ± 48 | <426 | 0.93 | 664 ± 60 | 0.93 | 664 ± 60 | 497 ± 386 | 1.00 | 195 |
| 250 | S2199P441 | 219.92 | 44.06 | 6.00 | 184 ± 10 | 352 ± 135 | 1.15 | 233 ± 14 | 265 ± 92 | 1.28 | 435 ± 18 | 1.28 | 435 ± 18 | 585 ± 156 | 1.26 | 707 |
| 251 | S2219P369 | 221.94 | 36.88 | 6.00 | 205 ± 9 | <277 | 1.19 | 264 ± 12 | <143 | 1.26 | 491 ± 15 | 1.26 | 491 ± 15 | <271 | 1.27 | 706 |
| 252 | S2222P609 | 222.18 | 60.95 | 4.00 | 295 ± 28 | 1121 ± 341 | 0.97 | 320 ± 37 | 840 ± 218 | 1.24 | 625 ± 47 | 1.24 | 625 ± 47 | 2003 ± 379 | 1.02 | 315 |
| 253 | S2223M405 | 222.30 | -40.48 | 8.00 | 157 ± 9 | 1292 ± 152 | 1.23 | 158 ± 12 | 1047 ± 98 | 1.24 | 335 ± 15 | 1.24 | 335 ± 15 | 2286 ± 170 | 1.43 | 1239 |
| 254 | S2229P543 | 222.92 | 54.33 | 4.80 | 168 ± 14 | 1046 ± 219 | 1.05 | 186 ± 19 | 631 ± 134 | 1.27 | 364 ± 24 | 1.27 | 364 ± 24 | 1605 ± 237 | 1.25 | 439 |
| 255 | S2246P257 | 224.58 | 25.70 | 3.20 | 235 ± 18 | <485 | 1.18 | 208 ± 32 | 496 ± 270 | 1.25 | 475 ± 44 | 1.25 | 475 ± 44 | 737 ± 497 | 1.18 | 189 |
| 256 | S2259M349 | 225.92 | -34.86 | 6.00 | 148 ± 12 | 1416 ± 156 | 1.22 | 114 ± 17 | 1179 ± 105 | 1.50 | 278 ± 21 | 1.50 | 278 ± 21 | 2532 ± 179 | 1.59 | 707 |
| 257 | S2266M473 | 226.55 | -47.28 | 4.00 | 200 ± 13 | 828 ± 83 | 1.15 | 211 ± 18 | 722 ± 67 | 1.56 | 424 ± 22 | 1.56 | 424 ± 22 | 1535 ± 106 | 1.68 | 315 |
| 258 | S2267M661 | 226.70 | -66.06 | 4.00 | 356 ± 25 | 387 ± 159 | 1.08 | 266 ± 28 | 569 ± 100 | 1.48 | 655 ± 39 | 1.48 | 655 ± 39 | 947 ± 178 | 1.50 | 315 |
| 259 | S2271M209 | 227.10 | -20.93 | 2.40 | 224 ± 9 | <297 | 1.03 | 271 ± 12 | <288 | 1.18 | 503 ± 14 | 1.18 | 503 ± 14 | <293 | 1.46 | 112 |
| 260 | S2279M285 | 227.90 | -28.46 | 3.20 | 184 ± 20 | 1343 ± 318 | 1.30 | 191 ± 25 | 1022 ± 184 | 1.37 | 402 ± 34 | 1.37 | 402 ± 34 | 2184 ± 335 | 1.46 | 195 |
| 261 | S2287P516 | 228.66 | 51.59 | 4.80 | 200 ± 16 | 287 ± 284 | 1.09 | 223 ± 22 | 278 ± 174 | 1.13 | 441 ± 28 | 1.13 | 441 ± 28 | 535 ± 307 | 1.18 | 439 |
| 262 | S2289M180 | 228.86 | -17.99 | 3.20 | 172 ± 13 | 2750 ± 769 | 1.06 | 210 ± 16 | 1173 ± 363 | 0.90 | 388 ± 21 | 0.90 | 388 ± 21 | 3216 ± 692 | 1.16 | 195 |
| 263 | S2295M456 | 229.50 | -45.63 | 4.80 | 183 ± 9 | 794 ± 80 | 1.12 | 202 ± 12 | 709 ± 60 | 1.47 | 398 ± 15 | 1.47 | 398 ± 15 | 1488 ± 98 | 1.47 | 439 |
| 264 | S2303M284 | 230.26 | -28.43 | 3.20 | 180 ± 24 | 1279 ± 303 | 1.20 | 202 ± 30 | 853 ± 183 | 1.32 | 400 ± 40 | 1.32 | 400 ± 40 | 1978 ± 326 | 1.33 | 195 |
| 265 | S2305M219 | 230.50 | -21.93 | 2.40 | 138 ± 59 | 1942 ± 1028 | 0.91 | 144 ± 85 | 1391 ± 655 | 1.21 | 317 ± 105 | 1.21 | 317 ± 105 | 2887 ± 1128 | 1.02 | 111 |
| 266 | S2306P622 | 230.59 | 62.16 | 4.80 | 302 ± 30 | 354 ± 213 | 1.31 | 401 ± 44 | <268 | 1.21 | 715 ± 53 | 1.21 | 715 ± 53 | 429 ± 270 | 1.43 | 439 |
| 267 | S2307M403 | 230.73 | -40.27 | 4.00 | 215 ± 37 | 791 ± 392 | 1.06 | 177 ± 50 | 1019 ± 261 | 1.04 | 472 ± 65 | 1.04 | 472 ± 65 | 1617 ± 457 | 1.13 | 299 |
| 268 | S2321M310 | 232.05 | -31.00 | 4.00 | 217 ± 21 | 1026 ± 172 | 1.19 | 163 ± 28 | 1074 ± 125 | 1.15 | 398 ± 36 | 1.15 | 398 ± 36 | 2109 ± 206 | 1.32 | 315 |
| 269 | S2326M246 | 232.60 | -24.60 | 2.40 | 234 ± 42 | <1092 | 1.12 | 234 ± 59 | 668 ± 362 | 1.55 | 491 ± 74 | 1.55 | 491 ± 74 | 1153 ± 619 | 1.63 | 111 |
| 270 | S2345P562 | 234.54 | 56.24 | 4.80 | 187 ± 27 | 479 ± 286 | 1.12 | 144 ± 40 | 851 ± 209 | 1.32 | 369 ± 50 | 1.32 | 369 ± 50 | 1342 ± 346 | 1.40 | 439 |
| 271 | S2352P460 | 235.24 | 45.95 | 10.00 | 224 ± 6 | 138 ± 65 | 1.06 | 267 ± 9 | 264 ± 46 | 1.29 | 514 ± 11 | 1.29 | 514 ± 11 | 405 ± 77 | 1.28 | 1958 |
| 272 | S2356P377 | 235.65 | 37.69 | 6.00 | 222 ± 6 | 626 ± 129 | 1.17 | 281 ± 7 | 416 ± 73 | 1.23 | 520 ± 9 | 1.23 | 520 ± 9 | 929 ± 132 | 1.35 | 707 |
| 273 | S2364P750 | 236.42 | 74.95 | 4.00 | 327 ± 20 | 436 ± 249 | 1.33 | 356 ± 28 | 396 ± 163 | 1.65 | 691 ± 35 | 1.65 | 691 ± 35 | 883 ± 280 | 1.90 | 315 |
| 274 | S2366M353 | 236.57 | -35.29 | 3.20 | 331 ± 35 | 1280 ± 251 | 1.15 | 350 ± 48 | 701 ± 187 | 1.32 | 677 ± 59 | 1.32 | 677 ± 59 | 1903 ± 305 | 1.34 | 195 |
| 275 | S2367M413 | 236.75 | -41.32 | 3.20 | 219 ± 44 | 843 ± 288 | 1.23 | 157 ± 62 | 1251 ± 230 | 1.25 | 465 ± 78 | 1.25 | 465 ± 78 | 1978 ± 370 | 1.28 | 195 |

BAND R1

BAND R2

BAND R12

COORDINATES

| NUMBER | SHADOW NAME | l | b | Size ^b | BAND R1 | | | BAND R2 | | | BAND R12 | | | v ^c |
|--------|-------------|--------|--------|-------------------|-----------------------------|-----------------------------|------------------------------|-----------------------------|-----------------------------|------------------------------|-----------------------------|-----------------------------|------------------------------|----------------|
| | | | | | I ₀ ^c | I ₁ ^c | χ _v ^{2d} | I ₀ ^c | I ₁ ^c | χ _v ^{2d} | I ₀ ^c | I ₁ ^c | χ _v ^{2d} | |
| 276 | S2371P188 | 237.10 | 18.81 | 3.20 | 171 ± 22 | 725 ± 680 | 1.22 | 180 ± 30 | 1200 ± 375 | 1.15 | 373 ± 39 | 2124 ± 684 | 1.29 | 194 |
| 277 | S2372P255 | 237.17 | 25.49 | 4.00 | 212 ± 13 | 436 ± 271 | 1.31 | 284 ± 18 | 378 ± 170 | 1.08 | 522 ± 23 | 682 ± 297 | 1.33 | 315 |
| 278 | S2373M564 | 237.32 | -56.37 | 4.80 | 301 ± 28 | 188 ± 151 | 1.20 | 301 ± 39 | 235 ± 127 | 1.29 | 612 ± 49 | 559 ± 199 | 1.27 | 439 |
| 279 | S2378M377 | 237.79 | -37.74 | 4.00 | 474 ± 37 | 446 ± 194 | 0.95 | 460 ± 52 | 406 ± 161 | 1.23 | 948 ± 64 | 863 ± 250 | 1.20 | 311 |
| 280 | S2378M455 | 237.81 | -45.53 | 4.80 | 211 ± 11 | 524 ± 60 | 1.04 | 272 ± 16 | 393 ± 54 | 1.28 | 497 ± 19 | 884 ± 81 | 1.24 | 439 |
| 281 | S2392P686 | 239.22 | 68.58 | 4.80 | 261 ± 17 | 1083 ± 203 | 1.32 | 246 ± 23 | 1008 ± 133 | 1.15 | 525 ± 29 | 2067 ± 228 | 1.28 | 439 |
| 282 | S2396M168 | 239.55 | -16.77 | 6.00 | 218 ± 6 | 1329 ± 357 | 1.10 | 206 ± 7 | 1874 ± 166 | 1.22 | 444 ± 9 | 3255 ± 319 | 1.14 | 707 |
| 283 | S2399M734 | 239.87 | -73.41 | 4.80 | 163 ± 30 | 718 ± 155 | 1.12 | 225 ± 44 | 343 ± 136 | 1.29 | 398 ± 53 | 994 ± 206 | 1.27 | 439 |
| 284 | S2408P344 | 240.76 | 34.39 | 4.00 | 194 ± 11 | 612 ± 230 | 1.23 | 206 ± 16 | 988 ± 145 | 1.06 | 414 ± 20 | 1756 ± 251 | 1.35 | 315 |
| 285 | S2421M288 | 242.15 | -28.80 | 3.20 | 174 ± 20 | 1694 ± 426 | 1.29 | 161 ± 27 | 1188 ± 246 | 1.37 | 352 ± 34 | 2654 ± 442 | 1.35 | 195 |
| 286 | S2425M653 | 242.49 | -65.34 | 4.00 | 293 ± 17 | 1332 ± 163 | 1.66 | 242 ± 20 | 999 ± 104 | 2.10 | 541 ± 27 | 2296 ± 181 | 2.59 | 315 |
| 287 | S2432M399 | 243.17 | -39.90 | 4.00 | 197 ± 46 | 1004 ± 337 | 1.37 | 283 ± 69 | 592 ± 271 | 1.16 | 475 ± 85 | 1798 ± 437 | 1.27 | 312 |
| 288 | S2437M448 | 243.73 | -44.79 | 4.00 | 248 ± 17 | 205 ± 134 | 1.61 | 338 ± 8 | <69 | 1.66 | 611 ± 31 | <252 | 2.12 | 315 |
| 289 | S2442P450 | 244.19 | 44.98 | 4.00 | 199 ± 17 | <849 | 1.17 | 246 ± 23 | 322 ± 308 | 1.24 | 478 ± 30 | <991 | 1.17 | 315 |
| 290 | S2445P347 | 244.55 | 34.65 | 4.00 | 180 ± 9 | 299 ± 239 | 1.01 | 182 ± 11 | 816 ± 131 | 1.11 | 385 ± 15 | 1205 ± 240 | 1.04 | 315 |
| 291 | S2457P732 | 245.73 | 73.16 | 3.20 | 300 ± 21 | 1167 ± 410 | 1.08 | 290 ± 25 | 1096 ± 223 | 1.23 | 614 ± 34 | 2167 ± 412 | 1.07 | 195 |
| 292 | S2468M280 | 246.84 | -28.04 | 6.00 | 206 ± 8 | 703 ± 203 | 1.28 | 233 ± 10 | 242 ± 111 | 1.56 | 447 ± 13 | 797 ± 204 | 1.68 | 707 |
| 293 | S2472P475 | 247.20 | 47.49 | 4.00 | 216 ± 14 | <965 | 1.11 | 263 ± 19 | 485 ± 301 | 1.09 | 493 ± 24 | 1030 ± 558 | 1.14 | 315 |
| 294 | S2483M436 | 248.27 | 743.64 | 4.80 | 192 ± 22 | 548 ± 143 | 1.29 | 184 ± 35 | 540 ± 122 | 1.46 | 402 ± 42 | 1028 ± 187 | 1.75 | 439 |
| 295 | S2486M322 | 248.61 | -32.21 | 3.20 | 137 ± 22 | 1780 ± 350 | 1.59 | 137 ± 31 | 1166 ± 223 | 1.51 | 273 ± 39 | 2840 ± 385 | 2.09 | 195 |
| 296 | S2489P764 | 248.90 | 76.36 | 3.20 | 333 ± 25 | 727 ± 278 | 1.26 | 328 ± 35 | 846 ± 194 | 1.16 | 681 ± 44 | 1591 ± 324 | 1.22 | 195 |
| 297 | S2495P347 | 249.54 | 34.73 | 4.00 | 176 ± 17 | <1273 | 1.09 | 188 ± 21 | 761 ± 461 | 0.94 | 381 ± 28 | 1358 ± 891 | 1.01 | 311 |
| 298 | S2509P588 | 250.86 | 58.81 | 12.00 | 251 ± 4 | 303 ± 60 | 1.38 | 267 ± 5 | 432 ± 39 | 1.39 | 540 ± 7 | 759 ± 68 | 1.60 | 2816 |
| 299 | S2540M809 | 253.97 | -80.94 | 4.00 | 234 ± 33 | <317 | 1.18 | 274 ± 48 | <295 | 1.16 | 517 ± 59 | <504 | 1.51 | 315 |
| 300 | S2544P423 | 254.42 | 42.33 | 4.00 | 160 ± 16 | 1343 ± 421 | 1.30 | 208 ± 23 | 1009 ± 254 | 1.48 | 401 ± 28 | 2145 ± 453 | 1.40 | 313 |
| 301 | S2551M300 | 255.11 | -30.01 | 6.00 | 152 ± 6 | 1325 ± 199 | 1.30 | 152 ± 8 | 980 ± 106 | 1.47 | 308 ± 11 | 2239 ± 195 | 1.78 | 707 |
| 302 | S2554P729 | 255.39 | 72.89 | 4.00 | 313 ± 18 | 1121 ± 291 | 1.03 | 242 ± 21 | 1560 ± 161 | 1.26 | 579 ± 28 | 2750 ± 297 | 1.21 | 315 |
| 303 | S2555M621 | 255.51 | -62.15 | 4.00 | 257 ± 33 | 737 ± 194 | 1.43 | 334 ± 50 | 506 ± 167 | 1.32 | 605 ± 60 | 1179 ± 255 | 1.53 | 315 |
| 304 | S2559P681 | 255.90 | 68.11 | 4.00 | 371 ± 19 | 578 ± 293 | 1.29 | 366 ± 24 | 706 ± 174 | 1.57 | 753 ± 31 | 1318 ± 310 | 1.78 | 315 |
| 305 | S2560M560 | 256.01 | -56.01 | 4.80 | 394 ± 29 | 262 ± 149 | 1.17 | 365 ± 40 | 386 ± 123 | 1.45 | 787 ± 50 | 630 ± 193 | 1.47 | 439 |
| 306 | S2573P344 | 257.34 | 34.43 | 6.00 | 198 ± 4 | <337 | 1.05 | 224 ± 10 | 748 ± 322 | 1.07 | 448 ± 14 | 756 ± 630 | 1.10 | 706 |
| 307 | S2587M464 | 258.74 | -46.44 | 4.80 | 102 ± 30 | 685 ± 130 | 1.10 | 144 ± 47 | 463 ± 125 | 1.27 | 266 ± 56 | 1130 ± 184 | 1.30 | 437 |
| 308 | S2599P486 | 259.91 | 48.58 | 6.00 | 230 ± 9 | 688 ± 160 | 1.17 | 265 ± 12 | 763 ± 102 | 1.13 | 519 ± 15 | 1404 ± 177 | 1.18 | 707 |
| 309 | S2614P261 | 261.42 | 26.05 | 4.00 | 155 ± 18 | 2428 ± 764 | 1.00 | 133 ± 23 | 2304 ± 390 | 1.10 | 313 ± 30 | 4562 ± 732 | 1.19 | 312 |
| 310 | S2624M289 | 262.36 | -28.95 | 8.00 | 176 ± 3 | 314 ± 148 | 1.19 | 187 ± 4 | 498 ± 70 | 1.40 | 370 ± 5 | 885 ± 134 | 1.44 | 1254 |
| 311 | S2632P841 | 263.23 | 84.06 | 4.00 | 179 ± 19 | 1249 ± 147 | 1.45 | 181 ± 28 | 1048 ± 115 | 1.24 | 369 ± 34 | 2277 ± 184 | 1.53 | 315 |
| 312 | S2639P429 | 263.85 | 42.92 | 6.00 | 223 ± 11 | 668 ± 224 | 1.07 | 252 ± 16 | 869 ± 138 | 1.22 | 493 ± 20 | 1626 ± 242 | 1.23 | 707 |
| 313 | S2643P666 | 264.31 | 66.62 | 4.00 | 328 ± 21 | 265 ± 120 | 1.21 | 378 ± 31 | 280 ± 103 | 1.12 | 718 ± 37 | 557 ± 158 | 1.27 | 315 |
| 314 | S2645P806 | 264.47 | 80.65 | 4.00 | 207 ± 23 | 1457 ± 276 | 1.13 | 203 ± 33 | 1169 ± 191 | 1.13 | 420 ± 41 | 2556 ± 320 | 1.29 | 315 |
| 315 | S2646M675 | 264.62 | -67.46 | 4.00 | 354 ± 8 | <146 | 1.25 | 453 ± 9 | <76 | 1.31 | 818 ± 12 | <92 | 1.45 | 316 |
| 316 | S2648P234 | 264.77 | 23.44 | 4.00 | 244 ± 17 | 1320 ± 1099 | 1.15 | 317 ± 23 | 1374 ± 546 | 1.51 | 587 ± 30 | 2459 ± 1022 | 1.61 | 315 |
| 317 | S2658M582 | 265.80 | -58.21 | 4.80 | 405 ± 25 | <361 | 1.18 | 481 ± 7 | <130 | 1.32 | 902 ± 44 | <331 | 1.48 | 439 |
| 318 | S2659P547 | 265.88 | 54.65 | 6.00 | 281 ± 8 | 179 ± 101 | 1.14 | 320 ± 10 | 294 ± 67 | 1.19 | 624 ± 14 | 465 ± 114 | 1.18 | 707 |
| 319 | S2688P435 | 268.85 | 43.54 | 4.00 | 233 ± 7 | <411 | 1.01 | 255 ± 23 | 456 ± 380 | 1.08 | 521 ± 30 | <979 | 1.14 | 316 |
| 320 | S2692M522 | 269.23 | -52.22 | 4.00 | 243 ± 18 | 981 ± 107 | 1.26 | 193 ± 24 | 711 ± 82 | 1.46 | 449 ± 31 | 1613 ± 132 | 1.46 | 315 |
| 321 | S2694M311 | 269.44 | -31.08 | 6.00 | 193 ± 5 | 223 ± 142 | 1.38 | 183 ± 7 | 568 ± 77 | 1.41 | 385 ± 8 | 836 ± 141 | 1.69 | 707 |

TABLE 1—Continued

| NUMBER | SHADOW NAME | COORDINATES ^a | | | BAND R1 | | | | BAND R2 | | | | BAND R12 | | | | |
|--------|-------------|--------------------------|--------|-------------------|-----------------------------|-----------------------------|-----------------------------|-----------------------------|-----------------------------|-----------------------------|-----------------------------|-----------------------------|-----------------------------|-----------------------------|-----------------------------|-----------------------------|----------------|
| | | l | b | Size ^b | I ₀ ^c | I ₁ ^c | χ _v ^d | I ₀ ^c | I ₁ ^c | χ _v ^d | I ₀ ^c | I ₁ ^c | χ _v ^d | I ₀ ^c | I ₁ ^c | χ _v ^d | v ^e |
| | | | | | | | | | | | | | | | | | |
| 322 | S2696M443 | 269.61 | -44.30 | 3.20 | 194 ± 20 | 319 ± 146 | 1.24 | 288 ± 30 | <194 | 1.30 | 479 ± 36 | 365 ± 187 | 1.44 | 195 | | | |
| 323 | S2697P237 | 269.68 | 23.67 | 6.00 | 236 ± 13 | 3761 ± 773 | 1.30 | 307 ± 18 | 2771 ± 393 | 1.54 | 566 ± 23 | 6081 ± 728 | 1.62 | 706 | | | |
| 324 | S2711P401 | 271.11 | 40.11 | 3.20 | 172 ± 18 | 2111 ± 687 | 1.17 | 210 ± 23 | 1207 ± 346 | 1.00 | 407 ± 30 | 2887 ± 652 | 0.87 | 194 | | | |
| 325 | S2726M564 | 272.59 | -56.39 | 4.00 | 482 ± 7 | <66 | 1.04 | 530 ± 9 | <59 | 1.14 | 1022 ± 10 | <63 | 1.20 | 316 | | | |
| 326 | S2733M457 | 273.32 | -45.74 | 3.20 | 269 ± 7 | <98 | 1.20 | 291 ± 18 | <175 | 1.64 | 576 ± 16 | <172 | 1.83 | 196 | | | |
| 327 | S2755M764 | 275.50 | -76.41 | 4.80 | 279 ± 8 | <100 | 1.32 | 327 ± 72 | <279 | 1.29 | 640 ± 12 | <271 | 1.53 | 440 | | | |
| 328 | S2755P531 | 275.54 | 53.10 | 6.00 | 240 ± 10 | 316 ± 141 | 1.11 | 258 ± 13 | 304 ± 87 | 1.11 | 517 ± 17 | 617 ± 154 | 1.17 | 707 | | | |
| 329 | S2759M475 | 275.94 | -47.51 | 3.20 | 303 ± 18 | 1349 ± 255 | 0.88 | 292 ± 22 | 1002 ± 153 | 1.08 | 605 ± 29 | 2270 ± 273 | 1.08 | 195 | | | |
| 330 | S2774M721 | 277.40 | -72.08 | 6.00 | 331 ± 9 | <153 | 1.07 | 327 ± 46 | 287 ± 141 | 1.17 | 670 ± 53 | 364 ± 209 | 1.33 | 708 | | | |
| 331 | S2788M588 | 278.76 | -58.75 | 4.00 | 362 ± 10 | <150 | 1.09 | 413 ± 57 | <516 | 1.07 | 832 ± 17 | <386 | 1.22 | 316 | | | |
| 332 | S2788M453 | 278.84 | -45.25 | 3.20 | 232 ± 16 | 1841 ± 391 | 1.08 | 221 ± 19 | 1392 ± 215 | 1.23 | 480 ± 26 | 3044 ± 396 | 1.18 | 194 | | | |
| 333 | S2792M549 | 279.16 | -54.91 | 4.00 | 354 ± 41 | 987 ± 539 | 1.30 | 382 ± 53 | 468 ± 332 | 1.15 | 776 ± 69 | 1184 ± 586 | 1.29 | 315 | | | |
| 334 | S2816M422 | 281.55 | -42.18 | 4.80 | 188 ± 6 | 1448 ± 234 | 1.21 | 184 ± 7 | 1132 ± 115 | 1.21 | 382 ± 10 | 2466 ± 218 | 1.40 | 438 | | | |
| 335 | S2825M653 | 282.50 | -65.33 | 3.20 | 200 ± 48 | 832 ± 351 | 1.05 | 256 ± 72 | 586 ± 283 | 1.14 | 474 ± 87 | 1381 ± 446 | 1.08 | 195 | | | |
| 336 | S2829M446 | 282.94 | -44.60 | 3.20 | 214 ± 14 | 1970 ± 268 | 1.47 | 207 ± 16 | 1159 ± 140 | 1.26 | 432 ± 21 | 2836 ± 263 | 1.61 | 195 | | | |
| 337 | S2840M628 | 283.98 | -62.85 | 3.20 | 242 ± 46 | <623 | 1.09 | 353 ± 69 | <397 | 1.19 | 623 ± 84 | <770 | 1.23 | 195 | | | |
| 338 | S2852M532 | 285.23 | -53.20 | 4.00 | 322 ± 39 | <705 | 1.41 | 410 ± 15 | <181 | 1.09 | 798 ± 30 | <517 | 1.25 | 313 | | | |
| 339 | S2855M394 | 285.53 | -39.36 | 3.20 | 160 ± 9 | 3220 ± 361 | 1.28 | 166 ± 10 | 1502 ± 173 | 1.19 | 332 ± 14 | 4167 ± 332 | 1.54 | 195 | | | |
| 340 | S2879P832 | 287.90 | 83.17 | 4.00 | 141 ± 17 | 1463 ± 183 | 1.21 | 55 ± 24 | 1619 ± 129 | 1.19 | 214 ± 30 | 3112 ± 215 | 1.35 | 315 | | | |
| 341 | S2897M591 | 289.74 | -59.14 | 4.80 | 232 ± 15 | <418 | 1.17 | 288 ± 86 | <630 | 1.12 | 564 ± 104 | <989 | 1.13 | 426 | | | |
| 342 | S2904M450 | 290.42 | -45.00 | 4.00 | 344 ± 19 | 529 ± 269 | 1.07 | 343 ± 24 | 420 ± 163 | 1.12 | 721 ± 31 | 773 ± 289 | 1.18 | 315 | | | |
| 343 | S2924M390 | 292.39 | -39.00 | 4.00 | 332 ± 10 | <748 | 1.20 | 279 ± 11 | 386 ± 223 | 1.25 | 579 ± 16 | 662 ± 445 | 1.40 | 315 | | | |
| 344 | S2996M565 | 299.59 | -56.52 | 4.80 | 387 ± 10 | <107 | 1.28 | 412 ± 60 | <381 | 1.24 | 773 ± 72 | <583 | 1.35 | 440 | | | |
| 345 | S3018M527 | 301.82 | -52.75 | 4.80 | 330 ± 66 | <617 | 1.18 | 476 ± 13 | <128 | 1.12 | 866 ± 17 | <277 | 1.26 | 437 | | | |
| 346 | S3026M628 | 302.57 | -62.81 | 4.80 | 191 ± 49 | 387 ± 294 | 1.19 | 278 ± 79 | 304 ± 267 | 1.14 | 508 ± 94 | 633 ± 406 | 1.25 | 438 | | | |
| 347 | S3041M389 | 304.11 | -38.93 | 4.00 | 253 ± 33 | 2915 ± 1765 | 1.02 | 228 ± 40 | 1948 ± 799 | 1.11 | 537 ± 55 | 4121 ± 1592 | 1.12 | 301 | | | |
| 348 | S3069M605 | 306.91 | -60.54 | 4.80 | 225 ± 39 | 408 ± 194 | 1.23 | 128 ± 64 | 884 ± 192 | 1.22 | 393 ± 75 | 1421 ± 281 | 1.36 | 437 | | | |
| 349 | S3075P846 | 307.50 | 84.58 | 4.00 | 199 ± 16 | 758 ± 189 | 1.24 | 170 ± 20 | 909 ± 119 | 1.26 | 394 ± 26 | 1631 ± 208 | 1.46 | 315 | | | |
| 350 | S3102M375 | 310.25 | -37.49 | 6.00 | 269 ± 10 | 3676 ± 1006 | 1.19 | 295 ± 12 | 1203 ± 422 | 1.20 | 605 ± 16 | 4526 ± 870 | 1.42 | 650 | | | |
| 351 | S3138M476 | 313.83 | -47.59 | 6.00 | 292 ± 4 | <50 | 1.22 | 354 ± 23 | <169 | 1.34 | 668 ± 8 | <73 | 1.49 | 708 | | | |
| 352 | S3148M538 | 314.77 | -53.76 | 4.00 | 326 ± 43 | <534 | 1.14 | 451 ± 18 | <216 | 1.21 | 783 ± 79 | <640 | 1.28 | 315 | | | |
| 353 | S3206M204 | 320.61 | -20.39 | 6.00 | 184 ± 32 | <2797 | 0.58 | 224 ± 43 | <1838 | 0.79 | 427 ± 57 | 3631 ± 1982 | 0.79 | 394 | | | |
| 354 | S3207M569 | 320.71 | -56.85 | 4.00 | 370 ± 13 | <98 | 1.40 | 533 ± 125 | <429 | 1.27 | 965 ± 21 | <393 | 1.36 | 314 | | | |
| 355 | S3222M718 | 322.18 | -71.82 | 6.00 | 214 ± 44 | <171 | 1.11 | 300 ± 10 | <66 | 1.27 | 574 ± 13 | <78 | 1.12 | 695 | | | |
| 356 | S3227M773 | 322.68 | -77.27 | 4.80 | 193 ± 26 | <193 | 1.09 | 234 ± 40 | 167 ± 121 | 1.13 | 456 ± 47 | 236 ± 181 | 1.10 | 439 | | | |
| 357 | S3229M410 | 322.86 | -40.98 | 6.00 | 245 ± 20 | <1060 | 0.98 | 293 ± 59 | 564 ± 366 | 1.20 | 530 ± 73 | 1510 ± 621 | 1.11 | 700 | | | |
| 358 | S3242M533 | 324.24 | -53.27 | 4.00 | 182 ± 42 | 997 ± 289 | 1.04 | 264 ± 66 | 636 ± 248 | 1.13 | 460 ± 78 | 1534 ± 380 | 1.21 | 314 | | | |
| 359 | S3251M265 | 325.10 | -26.54 | 6.00 | 204 ± 24 | 1436 ± 1358 | 0.63 | 250 ± 31 | 1125 ± 670 | 0.86 | 500 ± 41 | 2604 ± 1292 | 0.83 | 540 | | | |
| 360 | S3256M637 | 325.64 | -63.73 | 6.00 | 293 ± 49 | <218 | 1.21 | 239 ± 78 | 430 ± 213 | 1.15 | 598 ± 92 | 511 ± 313 | 1.20 | 697 | | | |
| 361 | S3259M479 | 325.89 | -47.87 | 6.00 | 242 ± 21 | 395 ± 208 | 1.19 | 324 ± 34 | 258 ± 158 | 1.26 | 574 ± 256 | 671 ± 256 | 1.29 | 707 | | | |
| 362 | S3286M294 | 328.55 | -29.37 | 6.00 | 219 ± 20 | <1436 | 0.60 | 247 ± 24 | <1052 | 0.71 | 514 ± 33 | <2106 | 0.71 | 486 | | | |
| 363 | S3331M529 | 333.08 | -52.91 | 4.80 | 235 ± 40 | 731 ± 248 | 1.65 | 283 ± 64 | 661 ± 221 | 1.54 | 557 ± 75 | 1285 ± 335 | 2.07 | 439 | | | |
| 364 | S3337M404 | 333.70 | -40.39 | 6.00 | 211 ± 7 | <274 | 1.01 | 154 ± 32 | 1120 ± 258 | 1.13 | 408 ± 40 | 1346 ± 451 | 1.23 | 685 | | | |
| 365 | S3388M370 | 338.83 | -36.98 | 6.00 | 174 ± 17 | 2069 ± 791 | 1.00 | 192 ± 22 | 880 ± 383 | 0.99 | 395 ± 28 | 2408 ± 737 | 1.06 | 680 | | | |
| 366 | S3393P835 | 339.34 | 83.48 | 4.00 | 244 ± 13 | 641 ± 98 | 1.14 | 231 ± 18 | 732 ± 75 | 1.64 | 499 ± 22 | 1340 ± 121 | 1.60 | 315 | | | |
| 367 | S3402M436 | 340.20 | -43.57 | 4.00 | 201 ± 15 | 712 ± 299 | 1.09 | 223 ± 21 | 853 ± 187 | 1.18 | 450 ± 27 | 1591 ± 327 | 1.05 | 313 | | | |

TABLE 1—Continued

| NUMBER | SHADOW NAME | COORDINATES ^a | | | Size ^b | BAND R1 | | | BAND R2 | | | BAND R12 | | | ν^c |
|--------|-------------|--------------------------|--------|------------|-------------------|----------|-------------|------------|-----------|---------|------------|-------------|---------|------------|---------|
| | | l | b | χ_v^d | | I_0^e | I_1^e | χ_v^d | I_0^e | I_1^e | χ_v^d | I_0^e | I_1^e | χ_v^d | |
| 368 | S3416M503 | 341.57 | -50.32 | 0.99 | 4.00 | 276 ± 39 | 352 ± 288 | 391 ± 60 | 303 ± 238 | 1.32 | 681 ± 71 | 661 ± 371 | 1.30 | 315 | |
| 369 | S3455M463 | 345.48 | -46.28 | 1.23 | 4.00 | 278 ± 39 | 356 ± 293 | 462 ± 63 | <351 | 1.22 | 751 ± 73 | 421 ± 385 | 1.32 | 315 | |
| 370 | S3476M506 | 347.58 | -50.63 | 1.13 | 3.20 | 213 ± 35 | 392 ± 285 | 304 ± 54 | 341 ± 232 | 1.21 | 542 ± 65 | 693 ± 365 | 1.28 | 195 | |
| 371 | S3478M618 | 347.80 | -61.79 | 1.12 | 4.00 | 220 ± 71 | 340 ± 285 | 164 ± 122 | 705 ± 309 | 1.24 | 404 ± 138 | 1174 ± 429 | 1.20 | 315 | |
| 372 | S3494M494 | 349.42 | -49.38 | 0.94 | 3.20 | 235 ± 41 | <699 | 238 ± 65 | 684 ± 290 | 1.32 | 476 ± 77 | 1225 ± 456 | 1.35 | 195 | |
| 373 | S3526M544 | 352.61 | -54.44 | 1.22 | 4.00 | 307 ± 9 | <71 | 452 ± 16 | <174 | 1.32 | 777 ± 14 | <138 | 1.51 | 316 | |
| 374 | S3538M684 | 353.84 | -68.45 | 1.02 | 8.00 | 206 ± 34 | 216 ± 193 | 286 ± 55 | <300 | 1.25 | 523 ± 66 | 475 ± 273 | 1.16 | 1201 | |
| 375 | S3541M613 | 354.15 | -61.25 | 1.26 | 4.00 | 213 ± 49 | 456 ± 222 | 197 ± 82 | 674 ± 227 | 1.47 | 483 ± 95 | 1045 ± 327 | 1.45 | 315 | |
| 376 | S3559M578 | 355.85 | -57.79 | 1.23 | 4.00 | 258 ± 69 | <603 | 228 ± 117 | 643 ± 345 | 1.41 | 546 ± 134 | 876 ± 497 | 1.36 | 315 | |
| 377 | S3564M288 | 356.35 | -28.79 | 0.99 | 3.20 | 166 ± 36 | 2637 ± 2447 | 261 ± 49 | <2002 | 1.15 | 429 ± 64 | 3368 ± 2253 | 1.14 | 193 | |
| 378 | S3574M334 | 357.36 | -33.36 | 1.35 | 3.20 | 233 ± 14 | <688 | 324 ± 16 | <436 | 1.25 | 578 ± 21 | <707 | 1.75 | 189 | |

^a Center of analyzed region, not necessarily the center of a shadow.

^b Diameter of the circular analyzed region in degrees.

^c Units of 10^{-6} counts s^{-1} arcmin $^{-2}$.

^d Reduced χ^2 value.

^e Degrees of freedom for the fits.

^f 1σ upper limit.

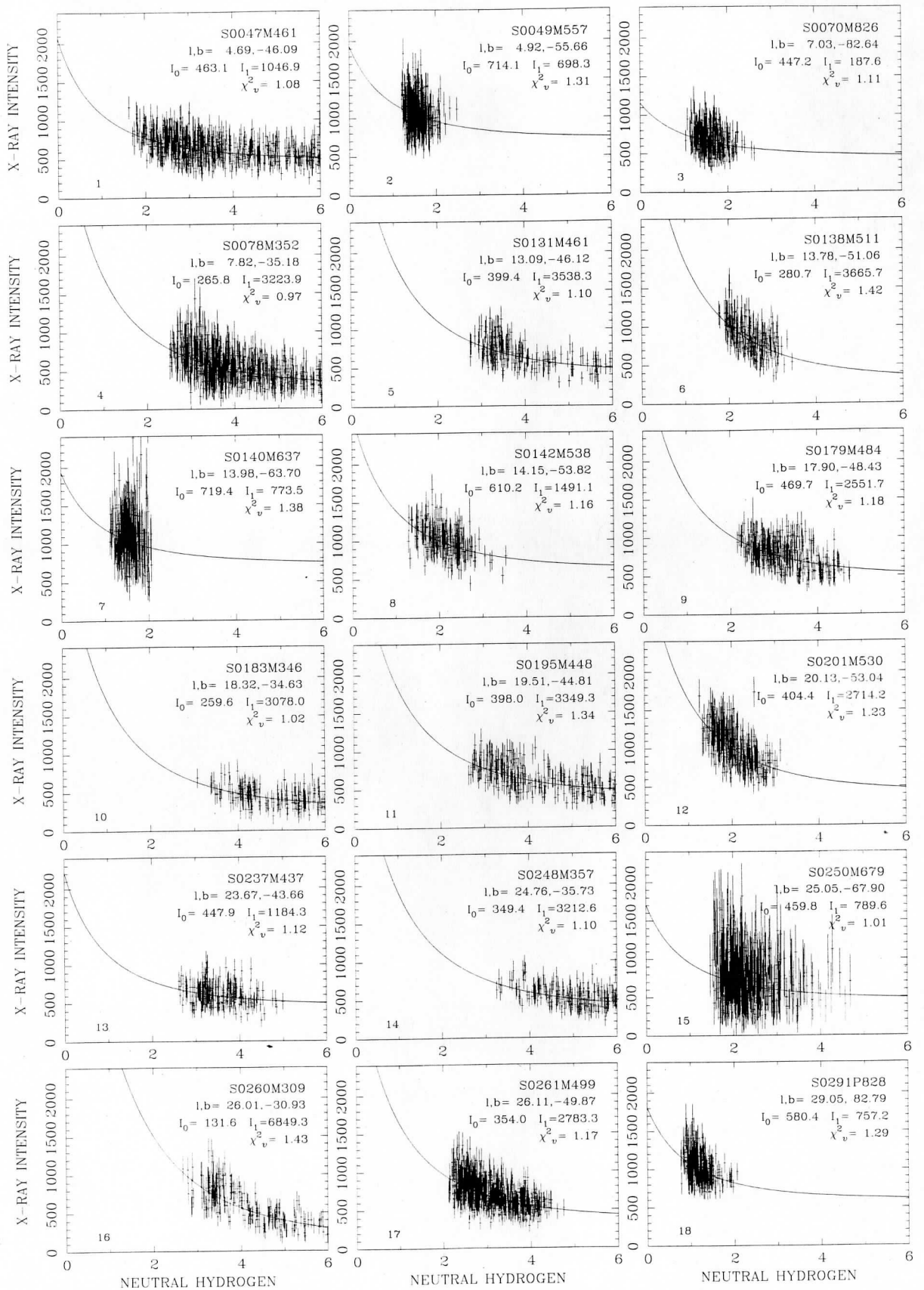


FIG. 6.—Scatter plots of the R12 band fits. The curves show the model fit to the data. The units of the horizontal axis are $10^{20} \text{ H I cm}^{-2}$. The units for the vertical axis are $10^{-6} \text{ R12 band counts s}^{-1} \text{ arcmin}^{-2}$.

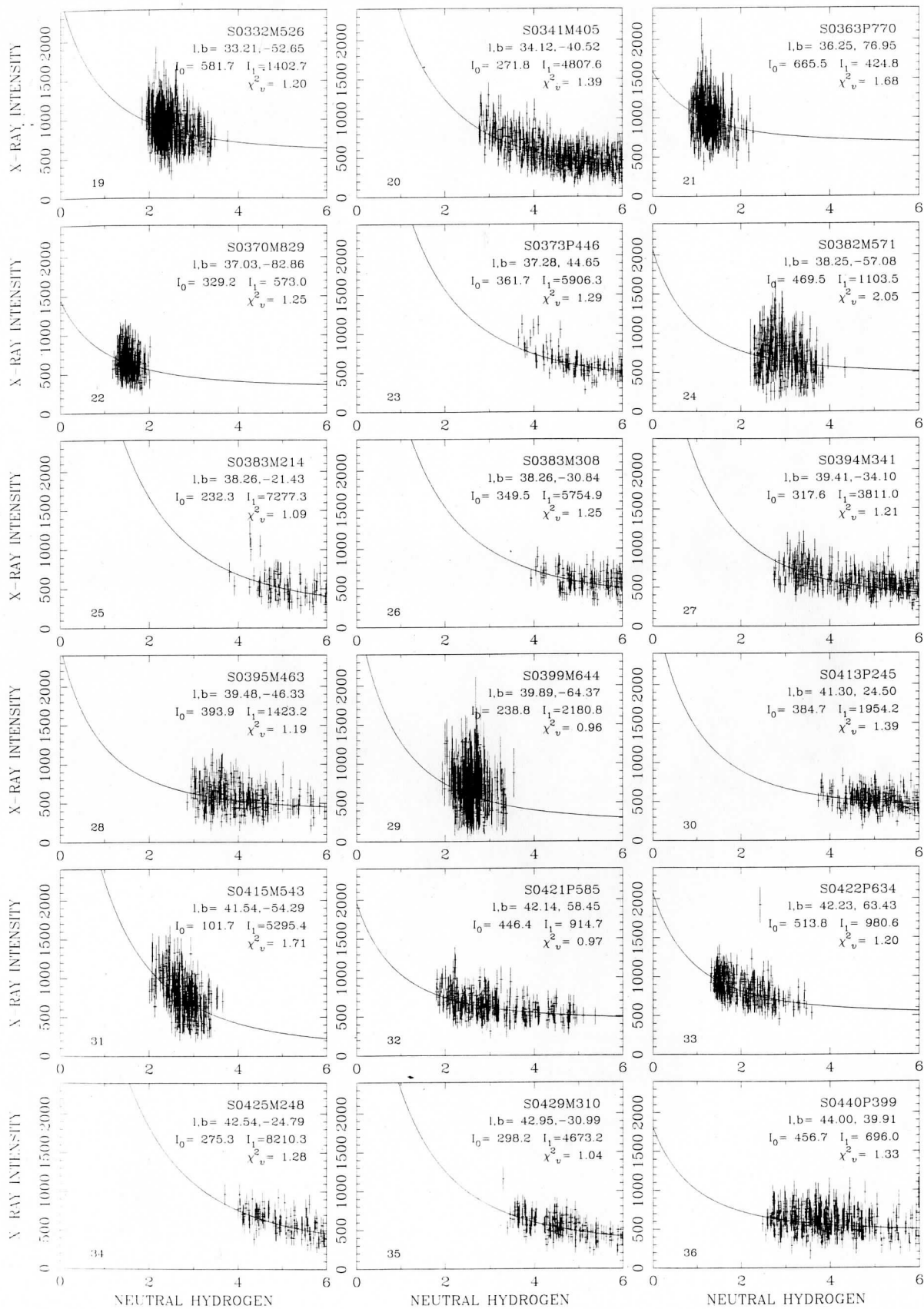


FIG. 6.—Continued

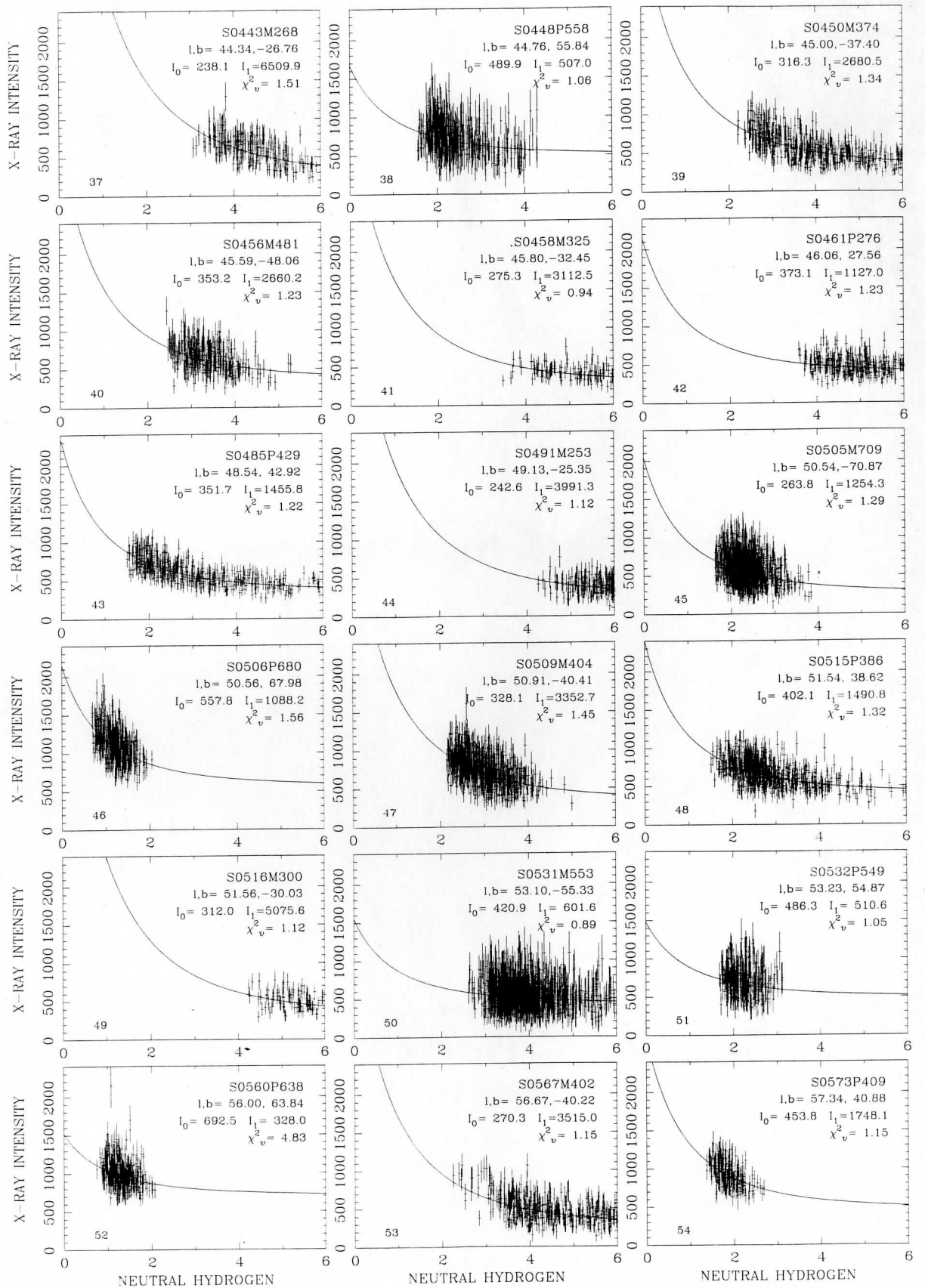


FIG. 6.—Continued

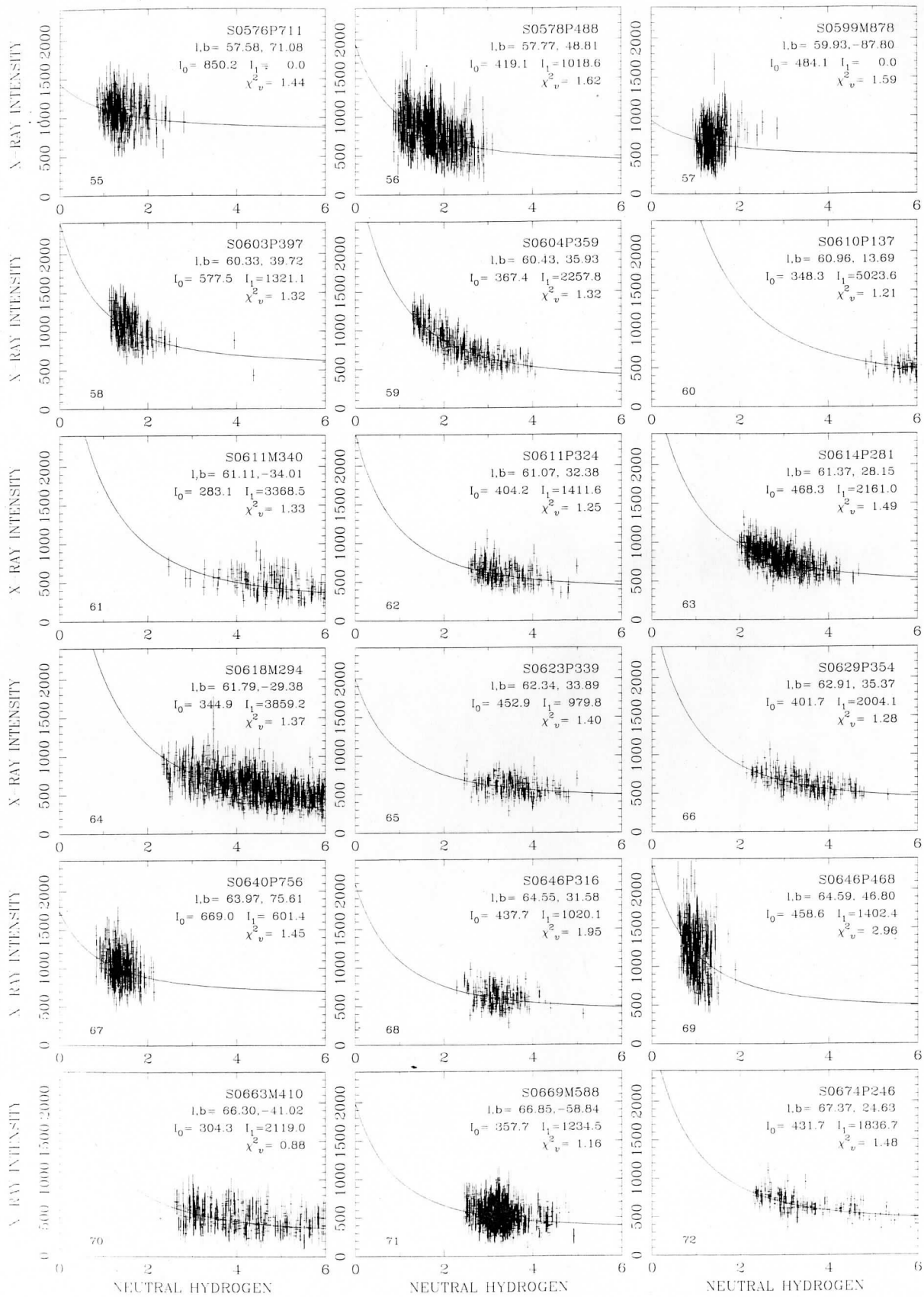


FIG. 6.—Continued

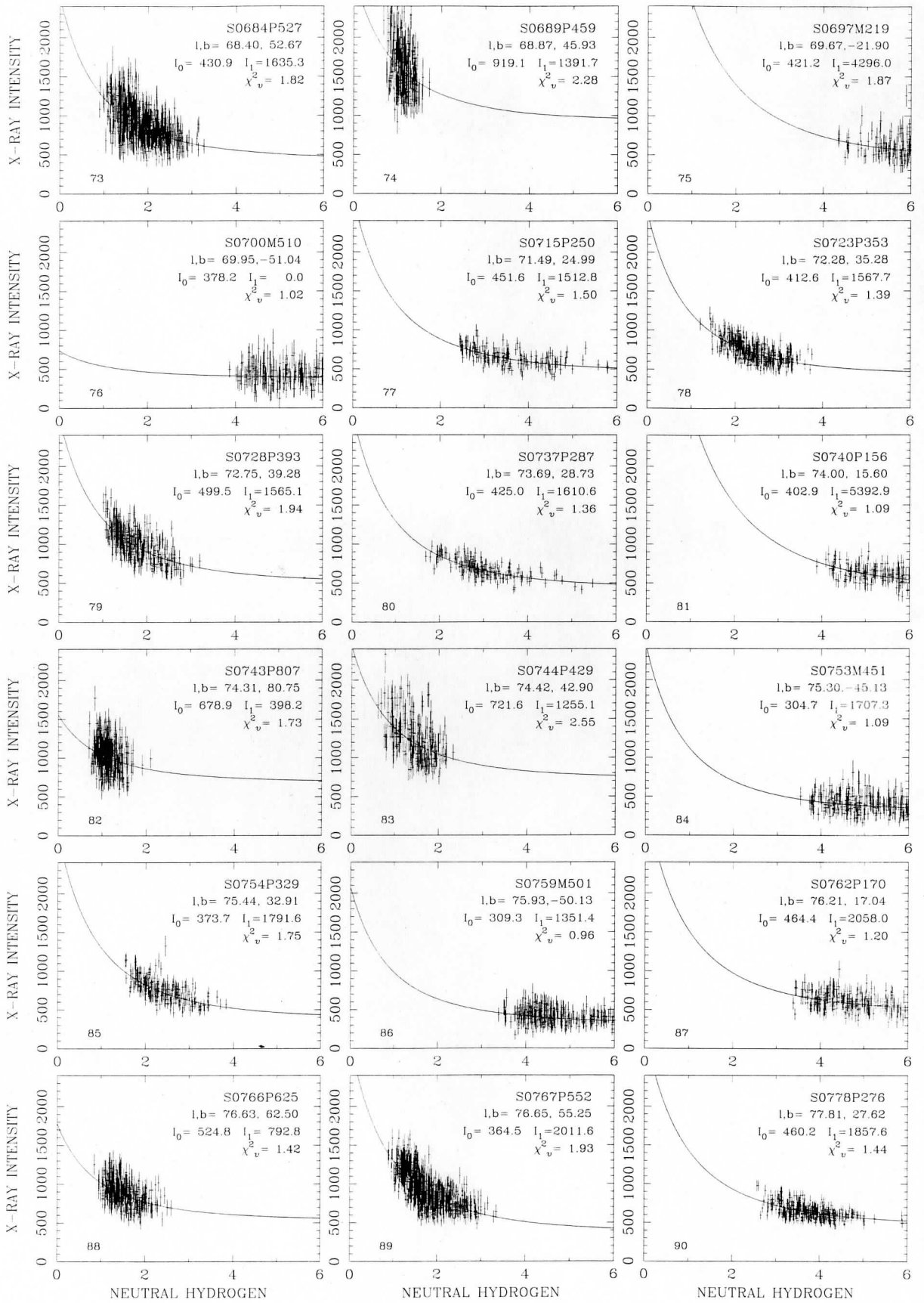


FIG. 6.—Continued

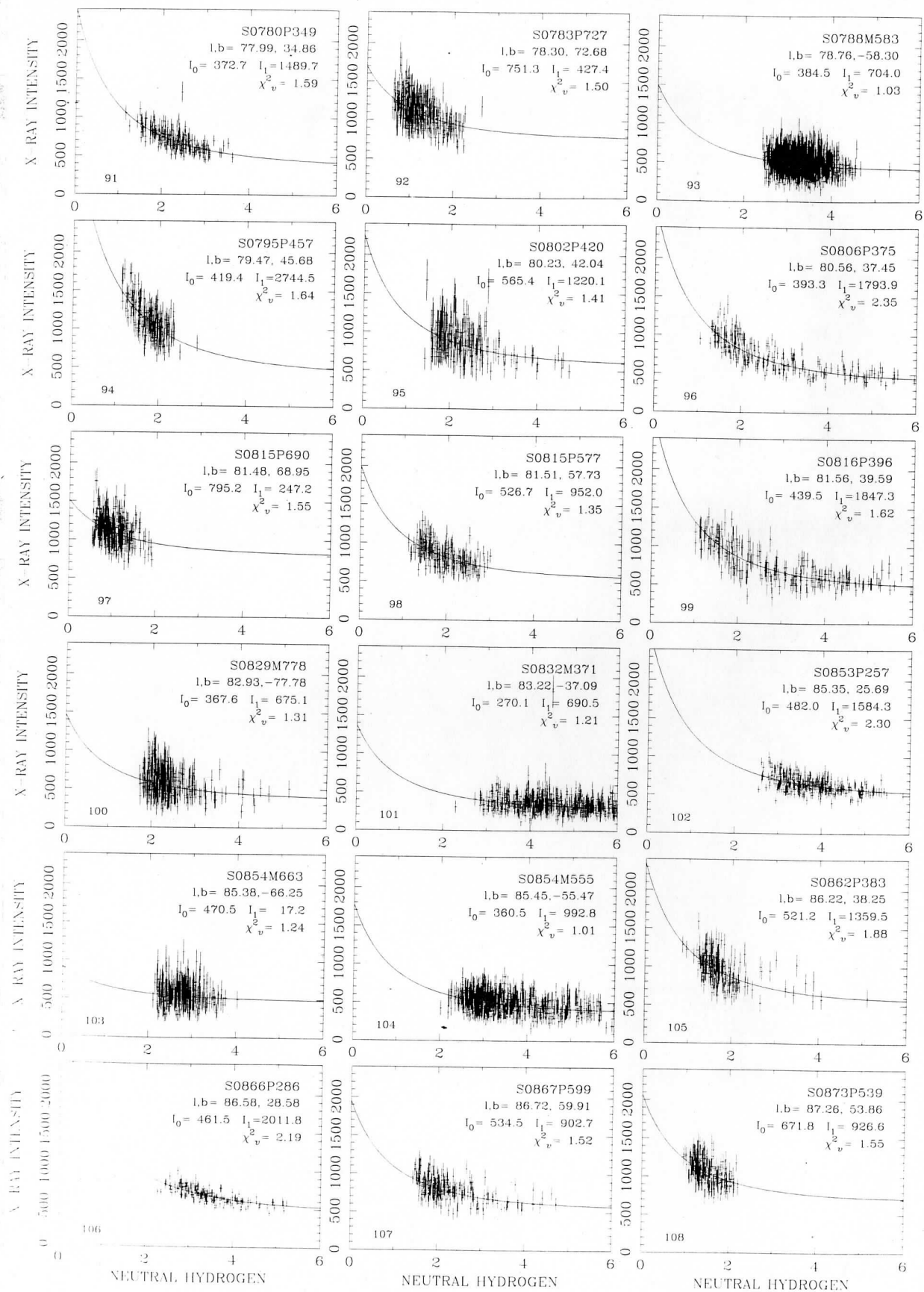


FIG. 6.—Continued

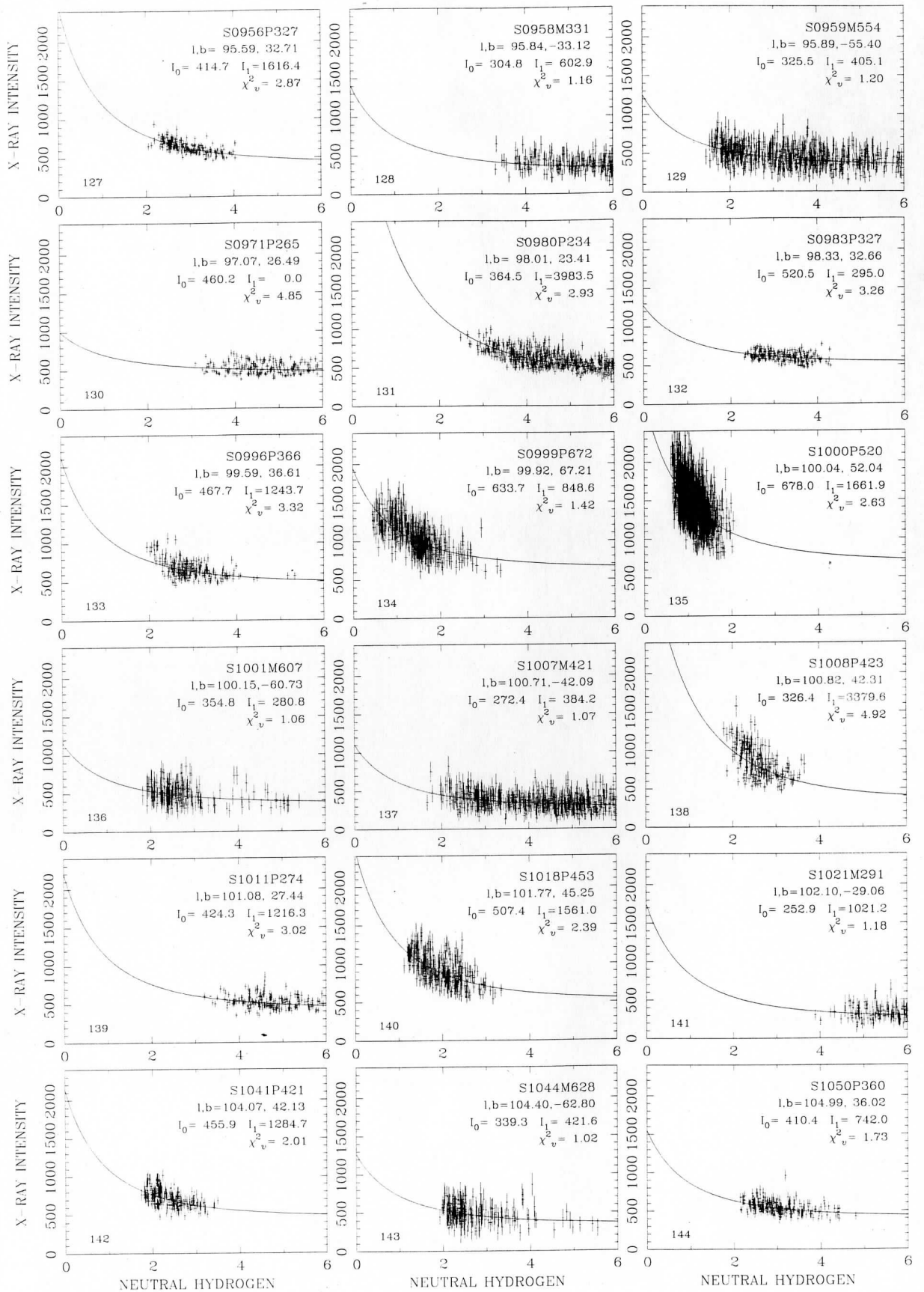


FIG. 6.—Continued

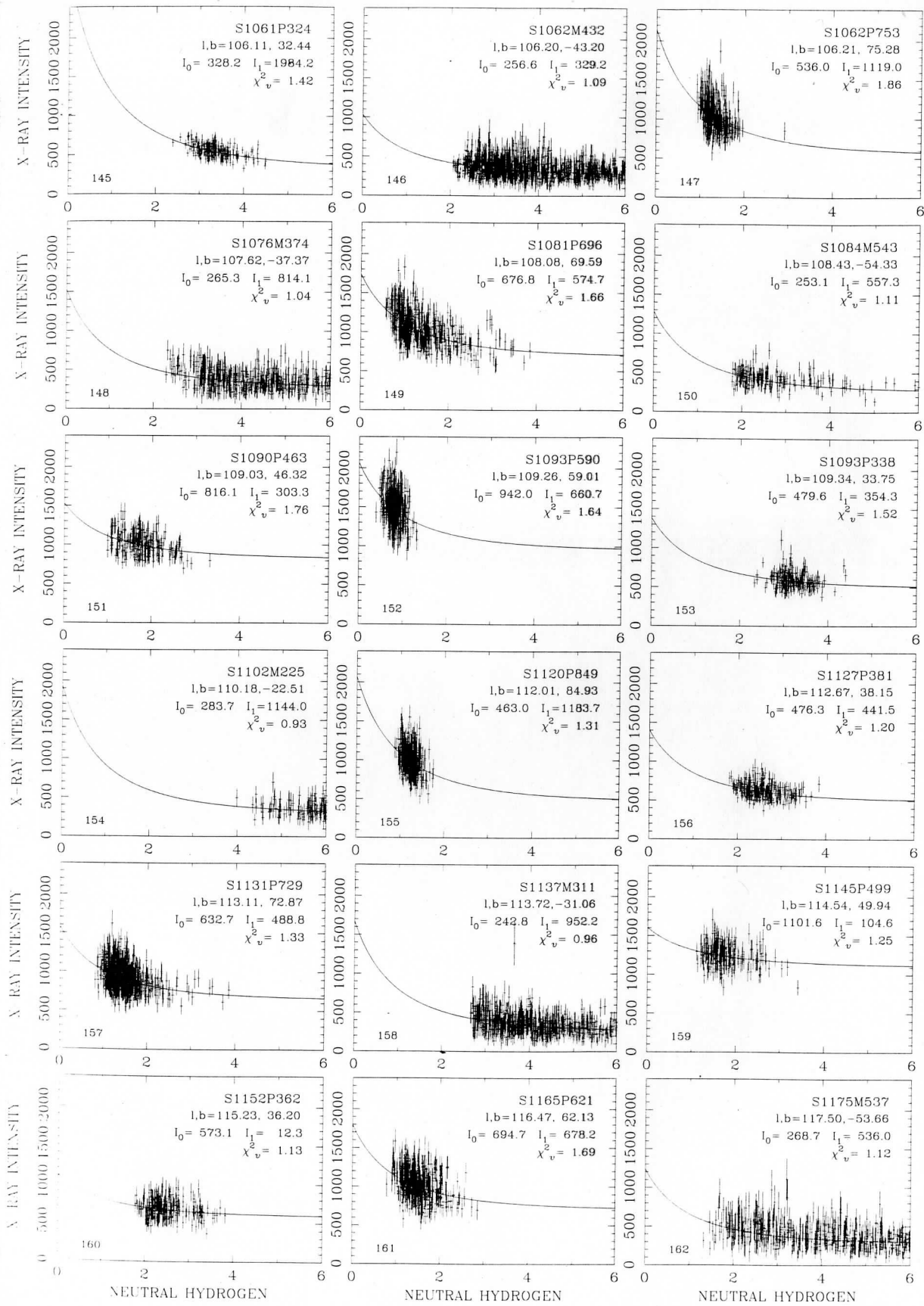


FIG. 6.—Continued

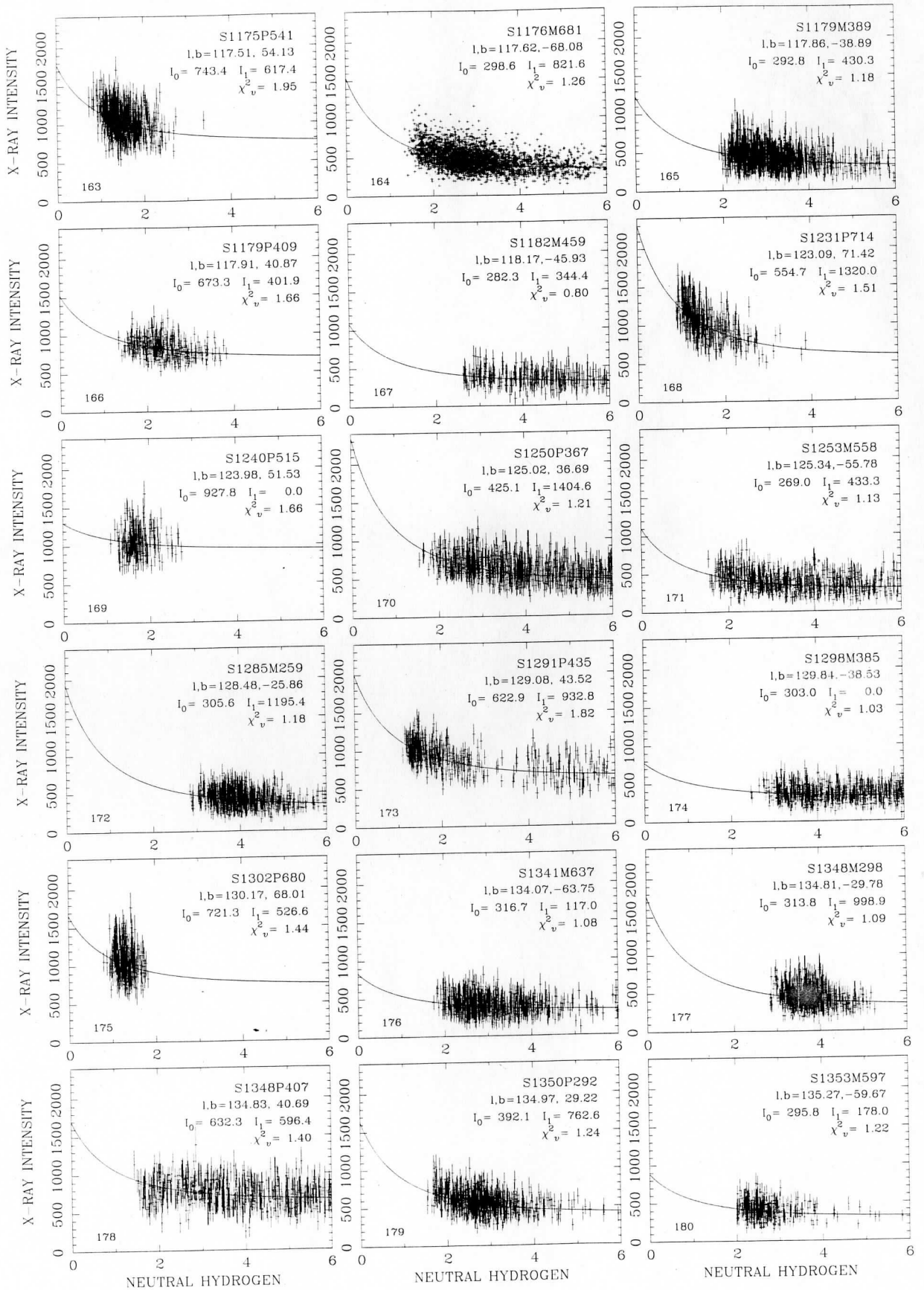


FIG. 6.—Continued

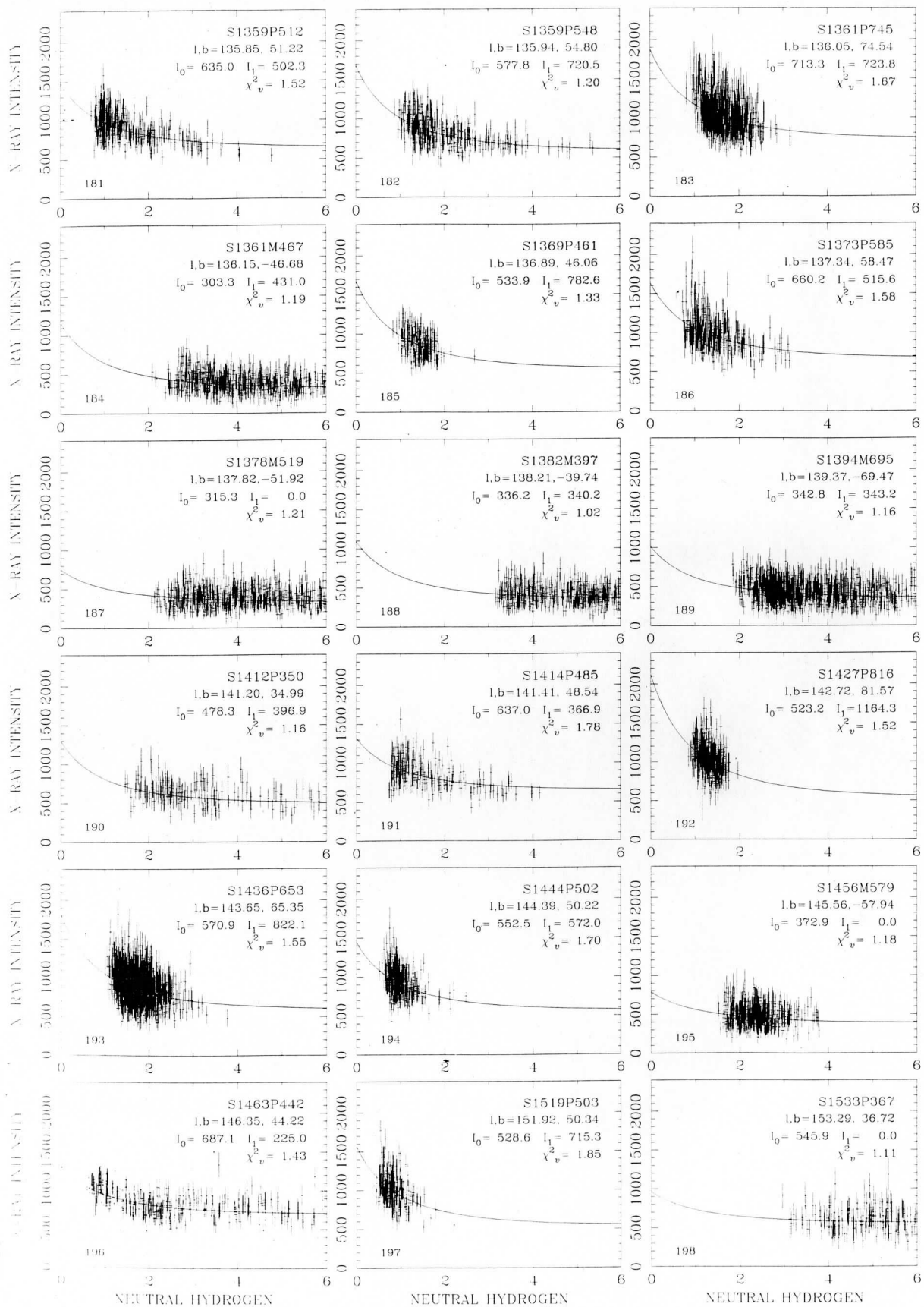


FIG. 6.—Continued

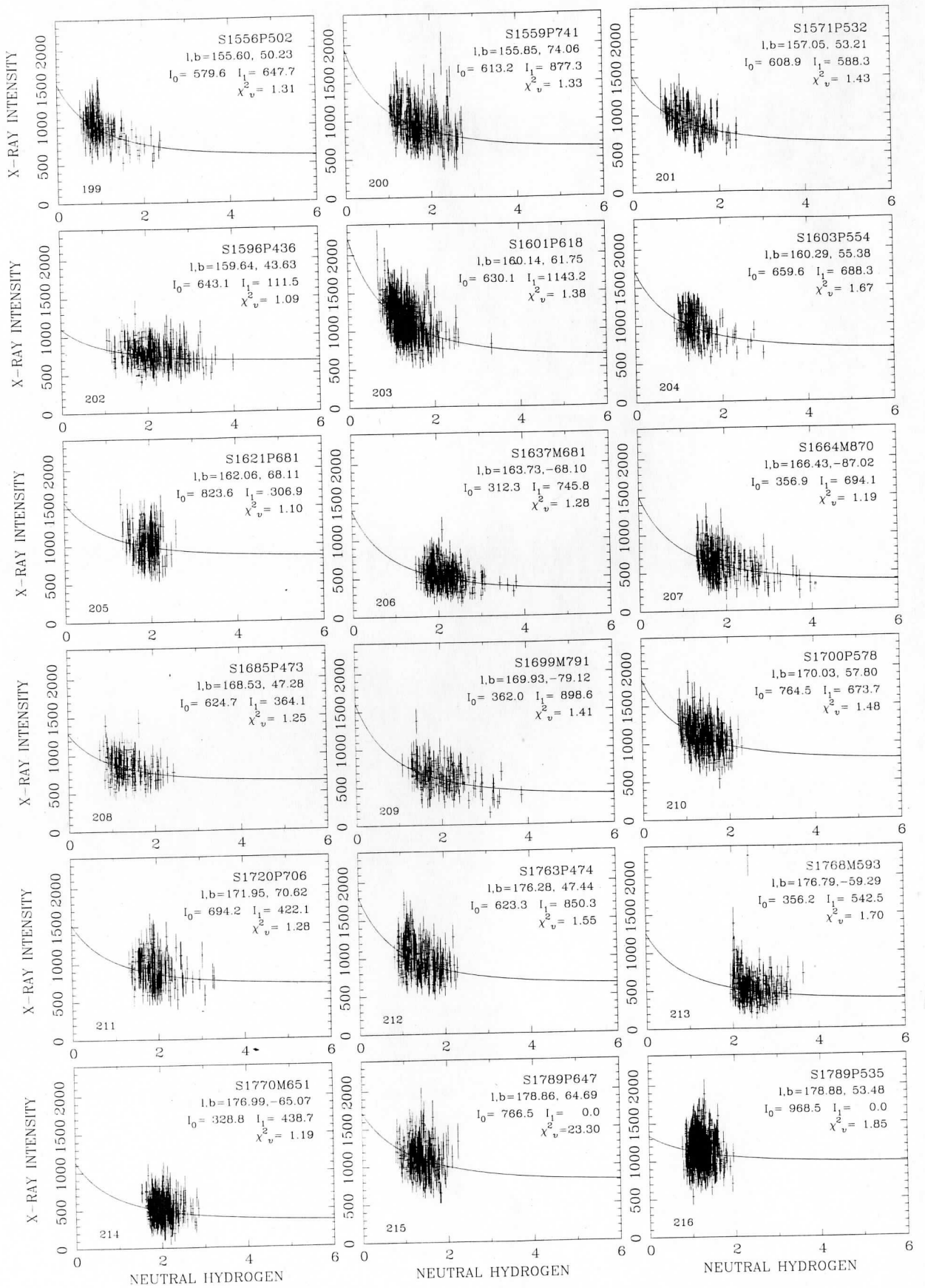


FIG. 6.—Continued

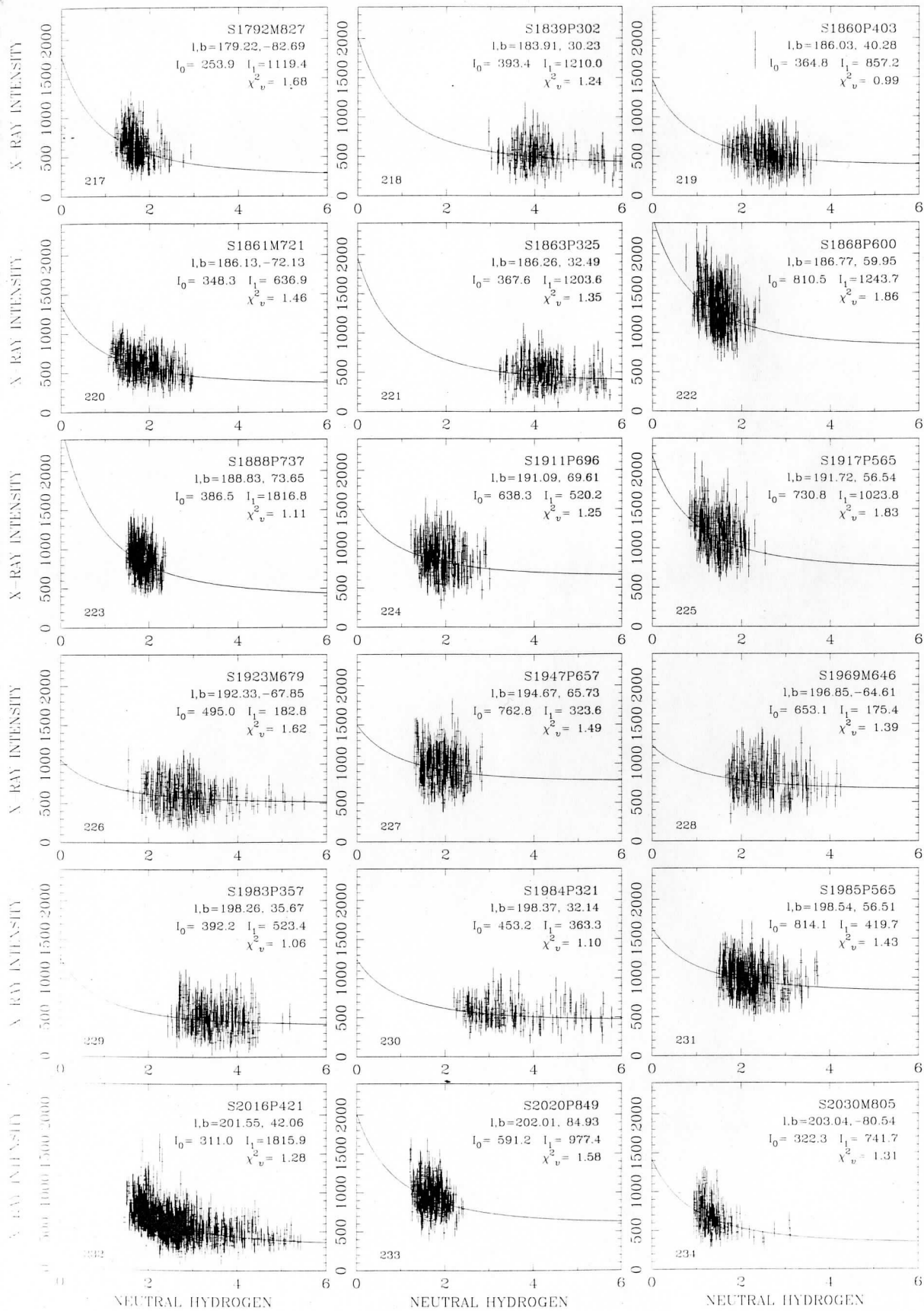


FIG. 6.—Continued

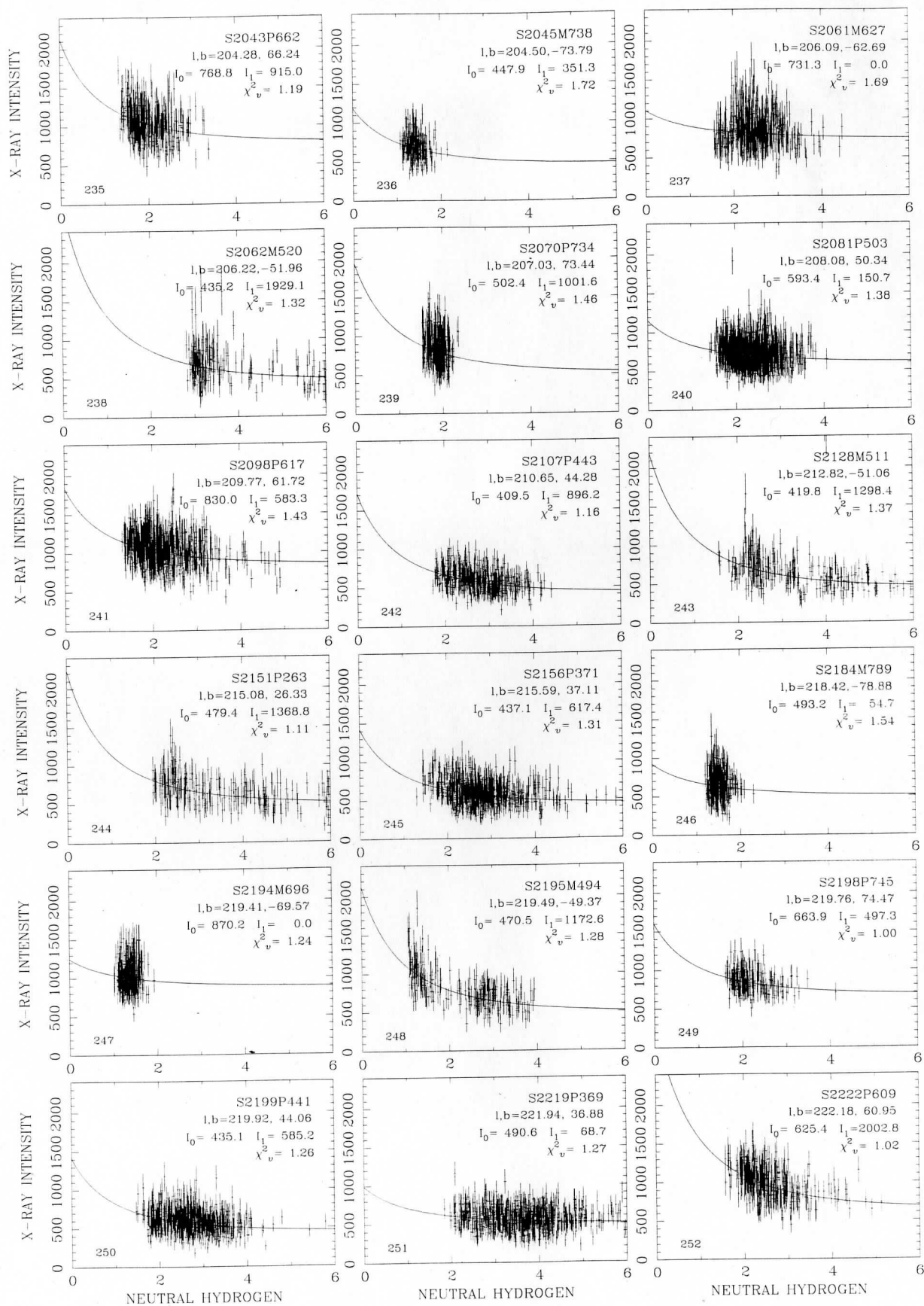


FIG. 6.—Continued

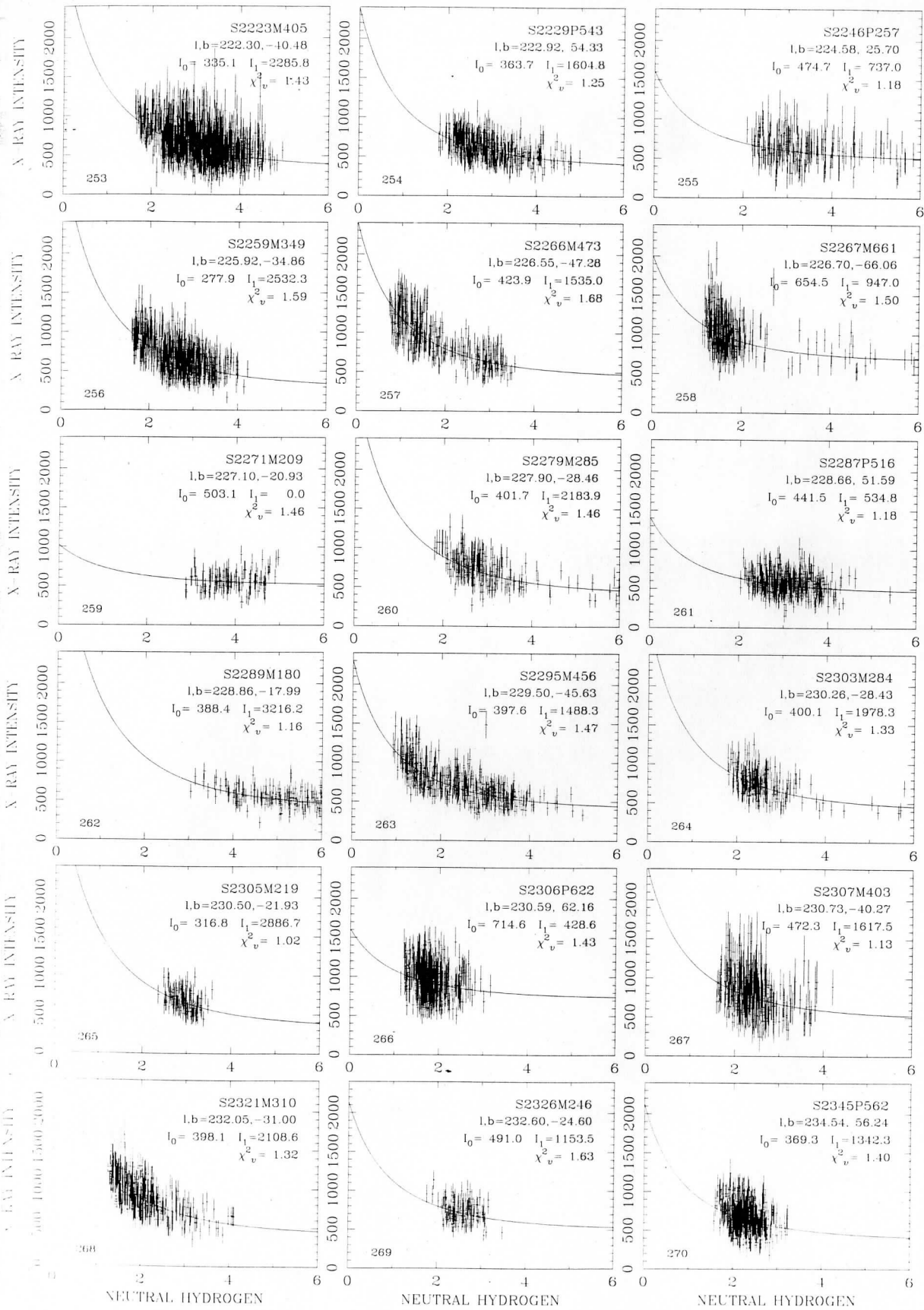


FIG. 6.—Continued

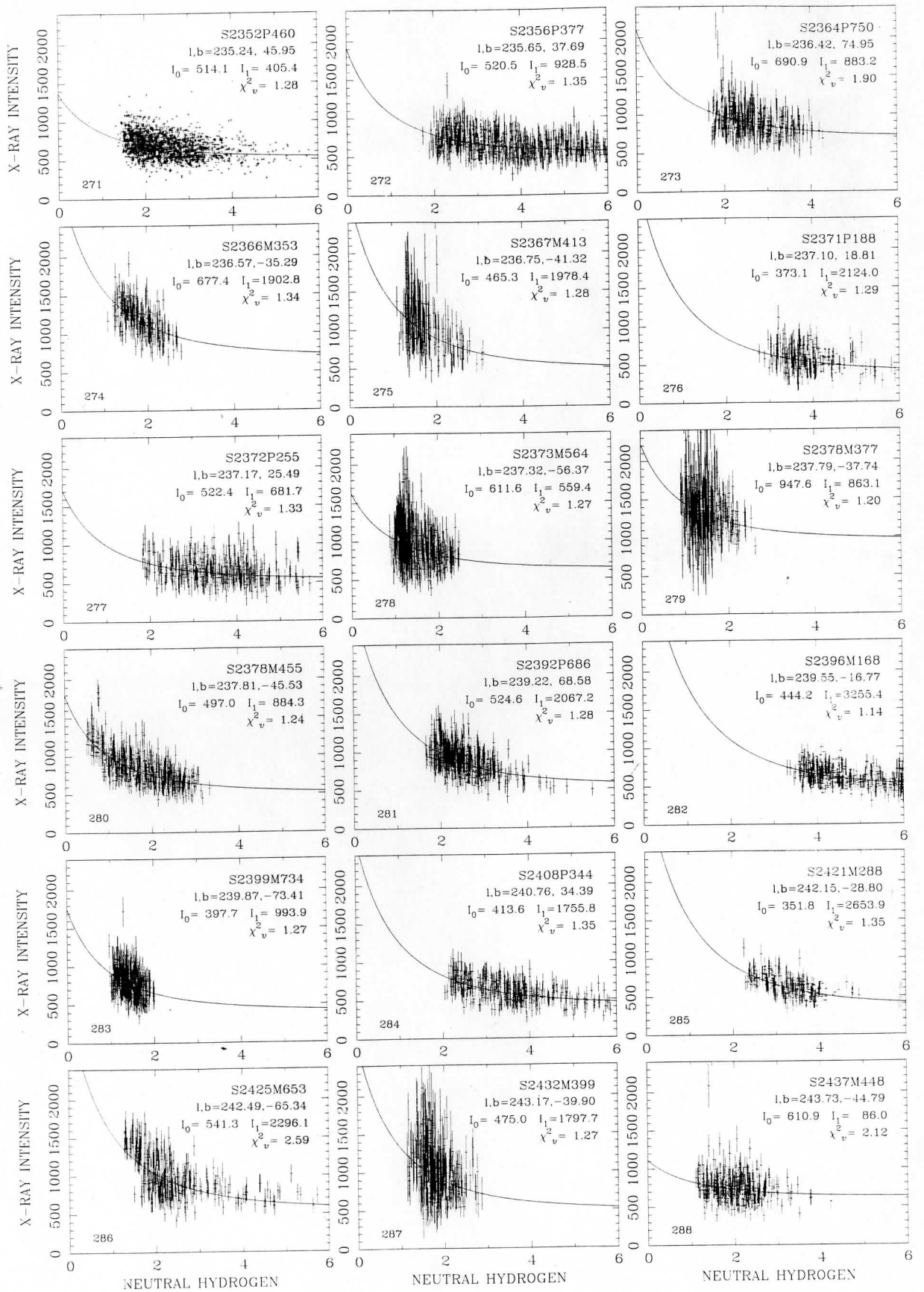


FIG. 6.—Continued

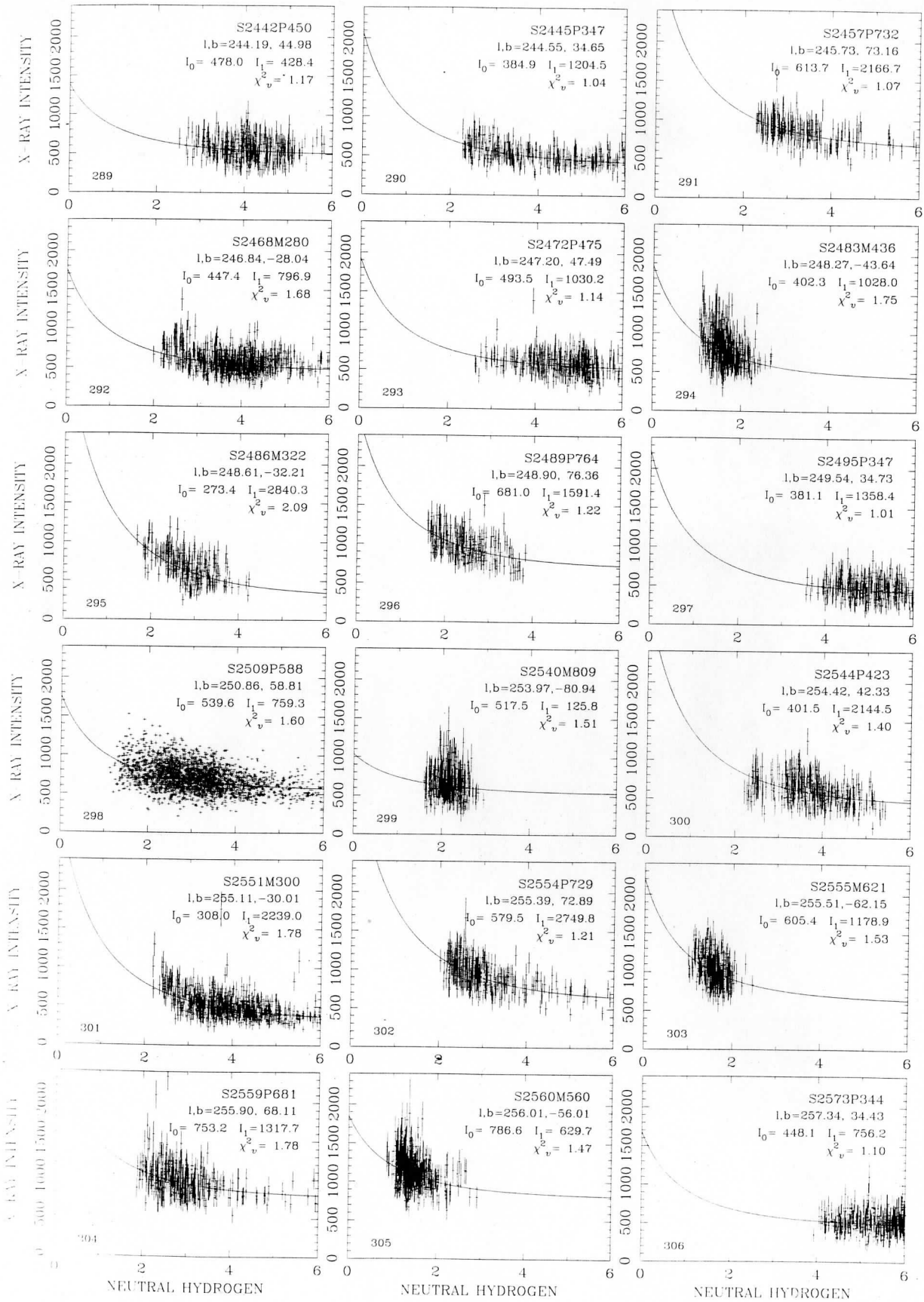


FIG. 6.—Continued

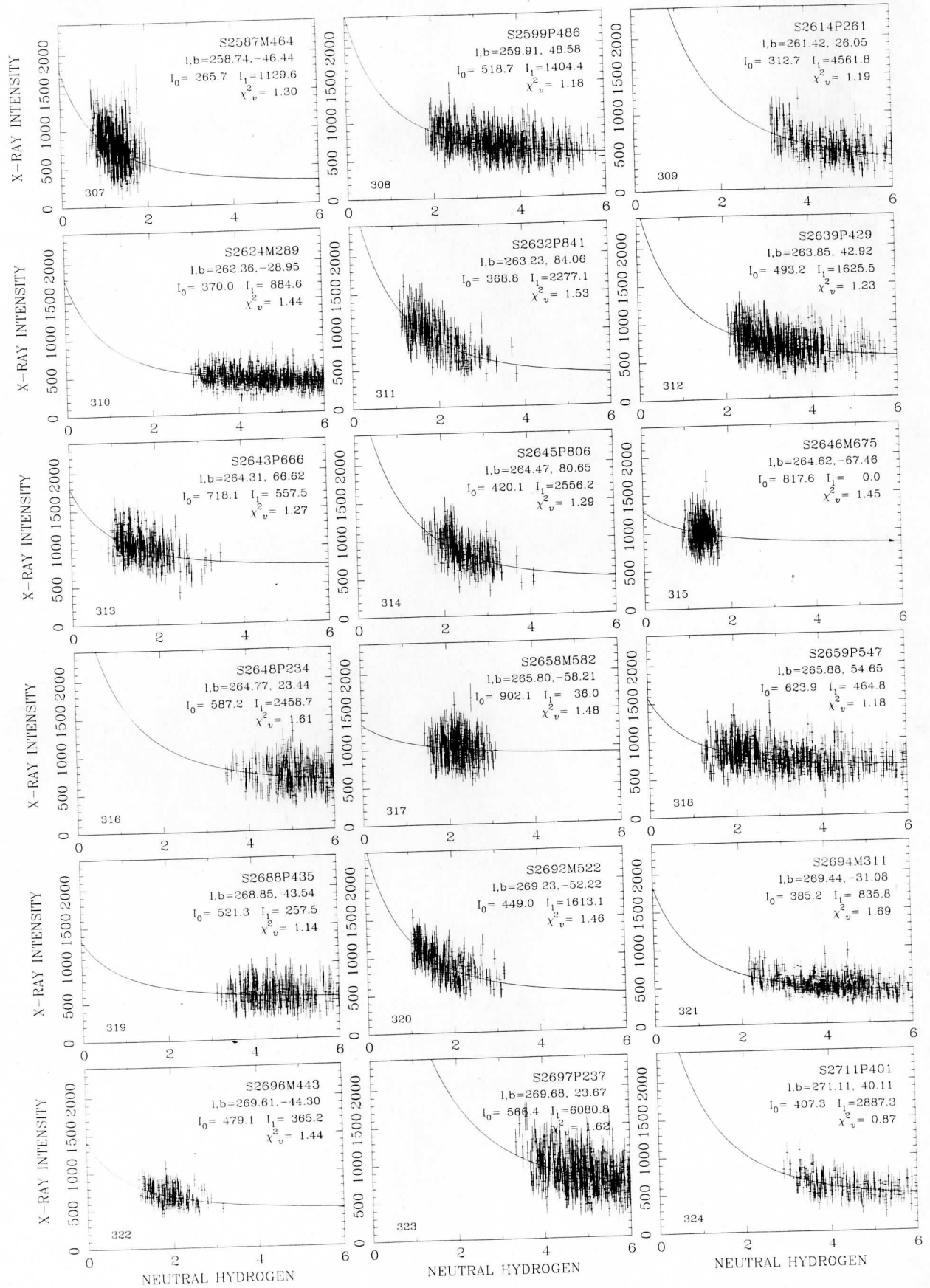


FIG. 6.—Continued

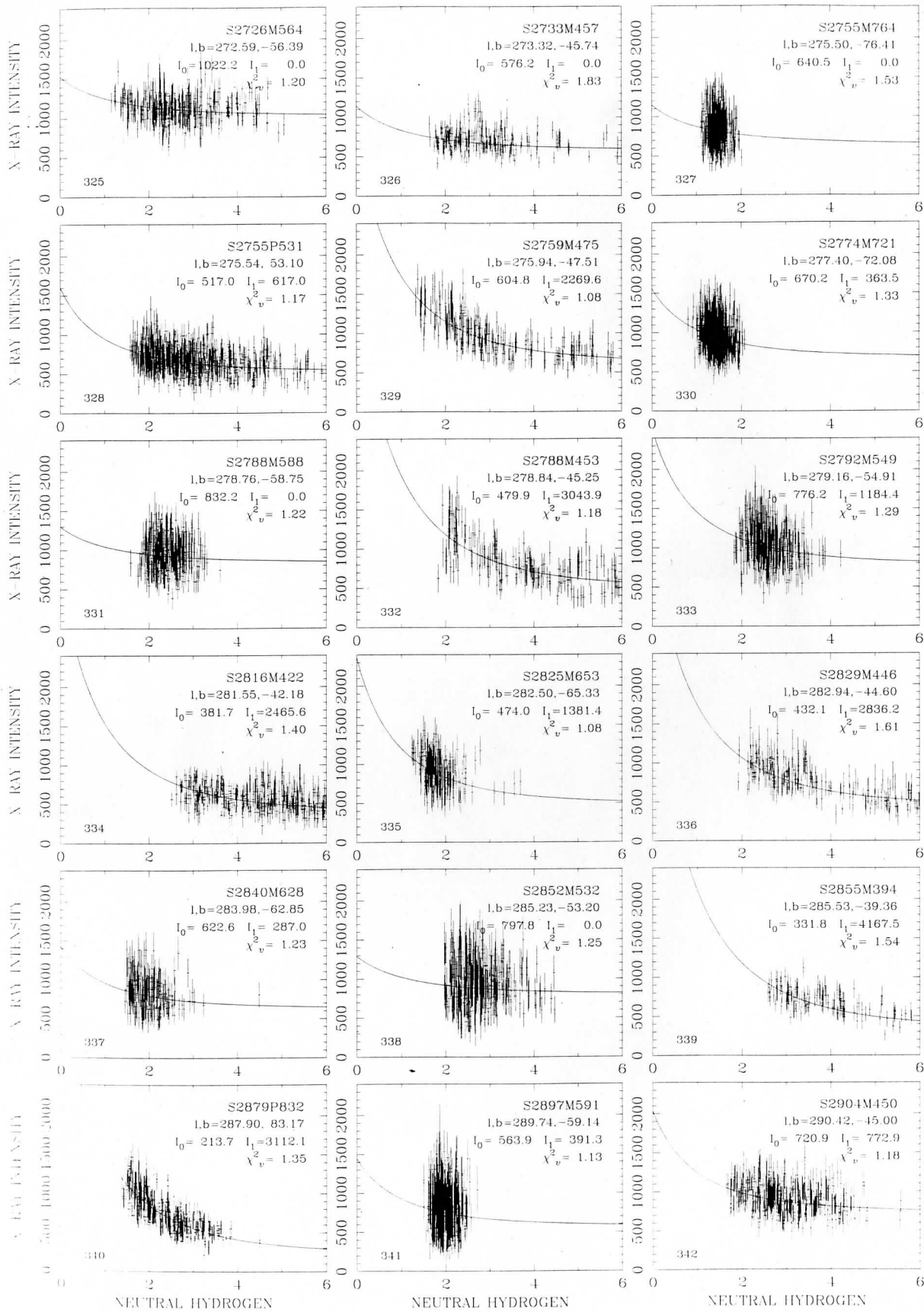


FIG. 6.—Continued

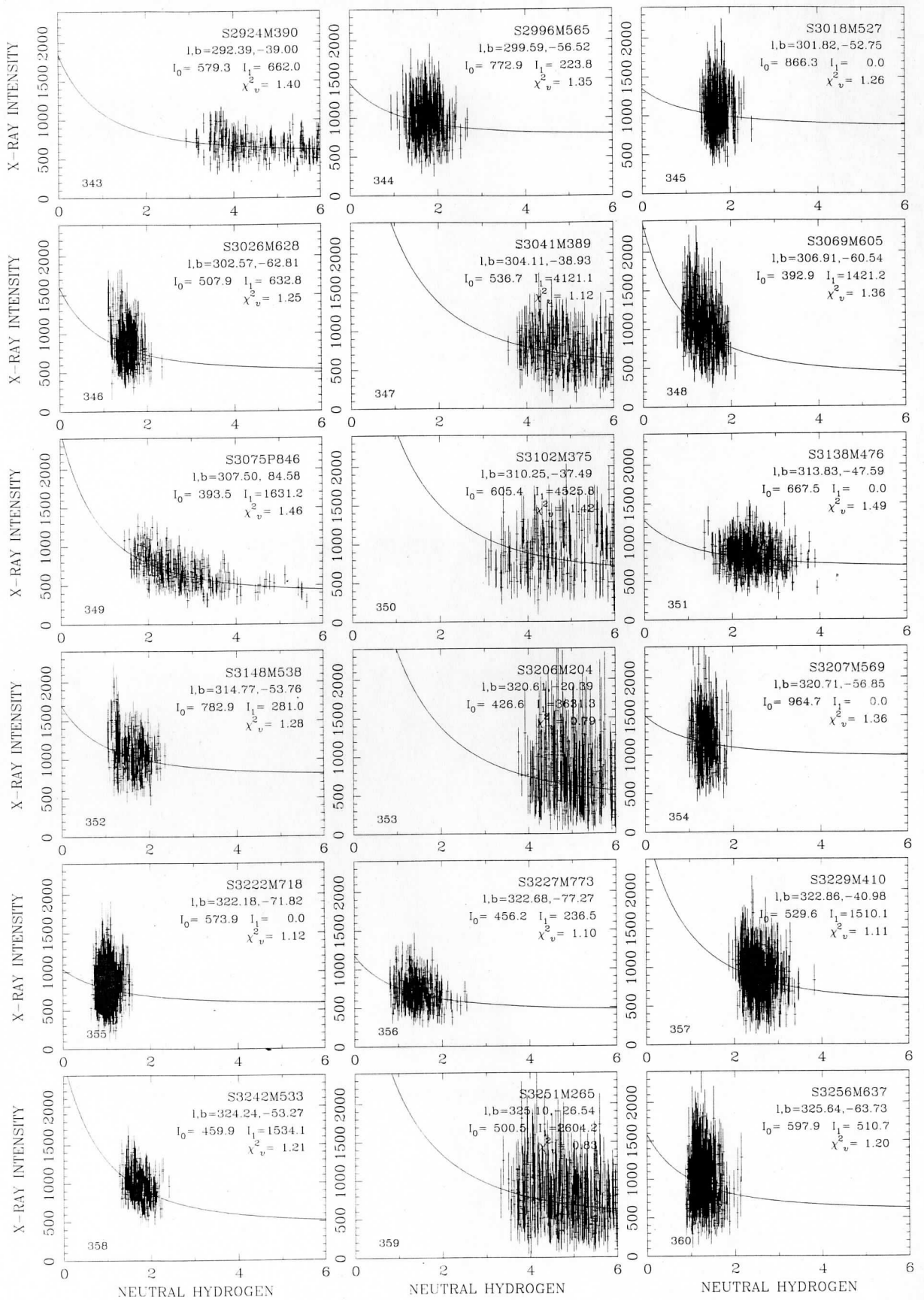


FIG. 6.—Continued

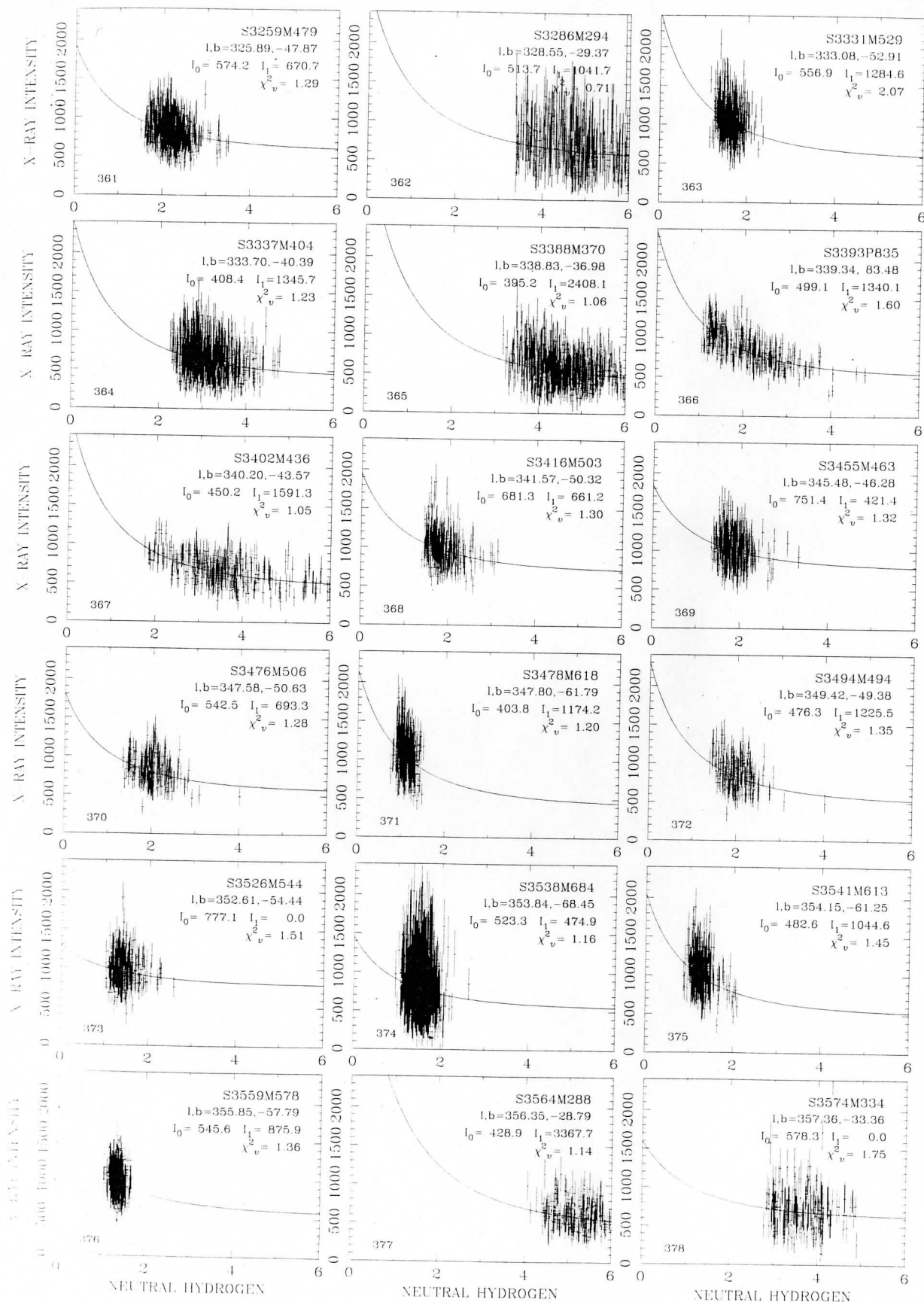


FIG. 6.—Continued

the table are the 1σ values derived using the Lampton, Margon, & Bowyer (1976) criteria ($\chi_{\min}^2 + 2.3$ for two-parameter fits). When the 1σ range in uncertainty includes zero, the 1σ upper limit is listed.

Figure 7 compares the foreground and distant R12 band intensities derived in this paper with those from Paper I. The foreground (I_0) results are in reasonable agreement, showing a moderately tight correlation, while the background (I_1) results show additional scatter. This is not particularly surprising as the I_1 results are more dependent on the chosen model, and the Paper I results were significantly smoothed. Since the regions for this analysis were specifically chosen to provide good measurements, the results of this paper are more reliable.

Figure 8 shows scatter plots of the hardness ratio (R2/R1 band ratio) for the I_0 and I_1 components as a function of the R12 band I_0 and I_1 intensities, respectively. In both cases while there is significant scatter in the data, there is no suggestion of a systematic variation with intensity. Figure 9 shows histograms for the R2/R1 band ratios for the I_0 and I_1 components. The average values for the data are 1.13 and 0.98, respectively. These values imply temperatures of $10^{6.08}$ and $10^{6.00}$ K, which are consistent with those of Paper I, where the derived values for the local and distant emission were $10^{6.06}$ and $10^{6.02}$ K⁷.

4.2. Variation of Intensity with Direction

Figure 10 presents the variation in the fitted values for I_0 and I_1 as a function of position on the sky. The relative size of the plotted circles corresponds to the relative intensities of the emission. From the plots it can be seen that the value for I_0 varies fairly slowly over the sky with higher values generally at higher latitudes. However, this is more consistently true for the northern hemisphere than for the southern. In the south there is an asymmetry in I_0 such that the longitude range $0^\circ < l < 180^\circ$ has in general lower intensities than the range $180^\circ < l < 360^\circ$.

The I_1 results displayed in Figure 10 have a completely different character. The regions of bright emission are considerably clumpier, and in general the higher intensities are at lower latitudes. The consistently bright regions are in the direction of Draco in the north and in the directions of $l, b \sim 40^\circ, -30^\circ$ and the “void” in the south (the void, or “Region of Bizarre Emptiness” [Cox 1997], at $l \sim 230^\circ$ is a direction in which there is little H I near the Galactic plane out to distances of a few hundred parsecs [see, e.g., Sfeir et al. 1999 and references therein]). Note that the latitudes of the displayed enhancements are relatively high ($20^\circ < |b| < 45^\circ$), although in all probability the enhancements would reach down closer to the Galactic plane if the analysis of this paper was able to sample them.

⁷ The quoting of temperatures for the thermal emission must always be done with caution as they are model dependent. Different thermal emission codes will attribute different temperatures to the same broadband ratio or fitted spectrum, and even different versions of a given code will show variations. In addition, current thermal equilibrium codes do not fit the high-spectral-resolution Diffuse X-ray Spectrometer (DXS, a Bragg crystal spectrometer flown on the space shuttle) data for the diffuse $\frac{1}{4}$ keV background particularly well (see Sanders et al. 1998, 2000). However, the use of the temperature does provide a scale (admittedly imperfect) with which to measure various models. We have much to learn about the ionization states and abundances of the X-ray-emitting plasmas.

As expected from the correlations shown in Figure 7, the results of this paper agree well with the position dependencies of the I_0 and I_1 values from Paper I.

4.3. Variation of Hardness Ratio with Direction

Figure 11 shows scatter plots of the average hardness ratios for the data in Figure 8 binned into 10° latitude bins. As in Figure 8, there is relatively little apparent variation in the ratios. On the other hand, when the data are binned into longitude bins they *do* show significant systematic variation (Figure 12), at least for the I_0 ratio. The I_0 ratio varies from a high of $R2/R1 \sim 1.25$ averaged over longitudes within 40° of the Galactic center to $R2/R1 \sim 1.04$ averaged over longitudes within 40° of the Galactic anticenter. The range in the I_0 ratio as a function of longitude is centered on the average value, and implies a temperature range of $10^{6.04}$ to $10^{6.13}$ K. The magnitude of the variation is not as great as that shown in Snowden, Schmidt, & Edwards (1990b), which reported a dipole gradient in the $\frac{1}{4}$ keV hardness ratio in the Wisconsin all-sky survey data (McCammon et al. 1983) with a range of $10^{5.9}$ to $10^{6.2}$ K with the low end of the dipole axis pointing at $l, b = 168^\circ, 7, 11^\circ$. When the data are analyzed with respect to the orientation of the Snowden et al. (1990b) dipole (Fig. 13), the extrapolated range in the ratio is 1.02–1.24, implying only a slightly broader temperature range of $10^{6.02}$ to $10^{6.13}$ K. The fitted line in Figure 13 is acceptable at the 30% level, with $\chi_\nu^2 = 1.15$ with 18 degrees of freedom. The best fit for a constant value has $\chi_\nu^2 = 2.50$ with 19 degrees of freedom, which can be ruled out at the greater than 99.9% confidence level, demonstrating the significance of the dipole variation. The FWHM range of the local component ratio is 0.91–1.30 (Fig. 9a), which is dominated by the systematic variation of the fitted values across the sky.

Figure 14 displays the variation on the hardness ratio of the I_0 data versus position. The southern hemisphere data clearly show the Galactic center/anticenter gradient. The gradient is less obvious in the northern hemisphere data, where the ratio appears to be more mixed, with only a slight trend of hardness ratio versus position.

Because of the statistics of the results for the distant component, it is much less clear whether there is a significant variation of the hardness of the emission across the sky. The FWHM range of the I_1 ratio distribution is 0.67–1.22 (Fig. 9b), implying a temperature range of $10^{5.83}$ – $10^{6.12}$ K. Although the width of the distribution is probably enhanced owing to the poorer statistics of the fits for the distant-emission parameters, it is likely that there is some true variation of the temperature in the halo. The emission appears clumpy suggesting both spatially separate emission regions and that the emission is distributed over large distances (when compared to the size of the LHB).

4.4. The LHB: I_0 and the Local H I Cavity

The premise of the Local Hot Bubble is that there is a cavity in the H I of the Galactic disk that contains the Sun and is filled with an X-ray-emitting plasma. This plasma produces half to all of the observed intensity at $\frac{1}{4}$ keV in all directions. The existence of the cavity is required by interstellar absorption-line measurements. The existence of the plasma within the cavity is absolutely required in low-latitude directions because there are nearby, optically-thick walls of H I (the edge of the cavity), yet a nonzero $\frac{1}{4}$ keV flux

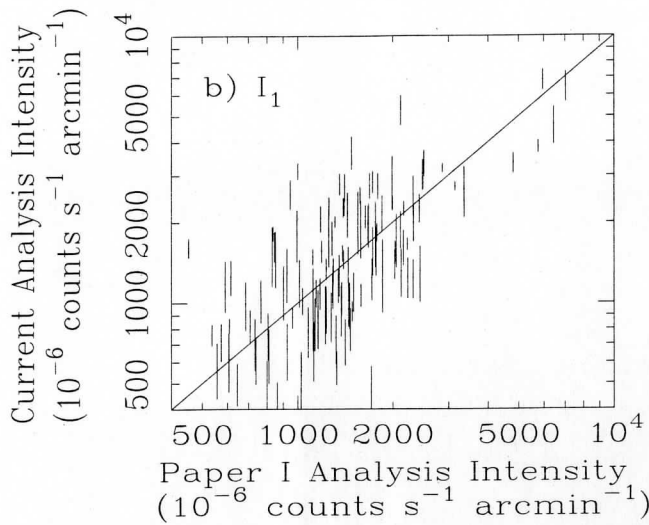
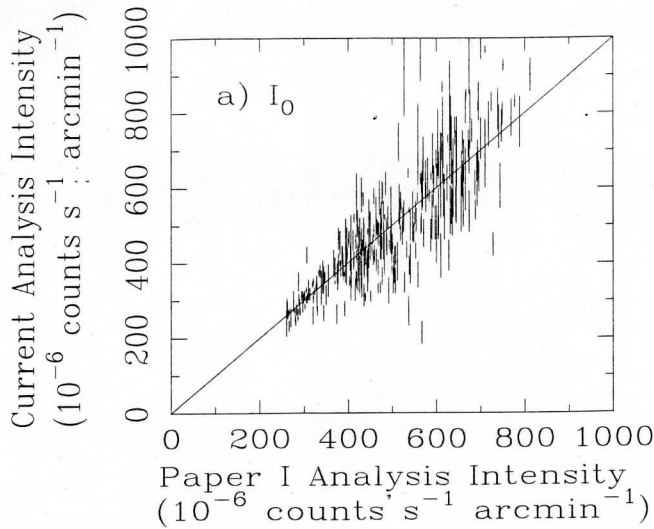


FIG. 7.—(a) Scatter plot comparing values for the foreground emission derived in this paper with those derived in Paper I. The units for both axes are 10^{-6} R12 band counts s^{-1} arcmin $^{-2}$. (b) Same as (a), except that the values for the distant emission are compared.

is observed. If the plasma is isothermal and is distributed uniformly throughout the cavity, then the fitted value for I_0 , when properly scaled, should provide a measure of the distance to the boundary of the cavity. A comparison between the I_0 intensities of Paper I with the shape of the local cavity is made by Sfeir et al. (1999), who presented a mapping of the local ISM based on an extensive optical absorption-line study. The results were in reasonably good agreement over most of the sky but there are directions where the cavity extends well beyond the required path length of plasma (e.g., the RBE).

The dipole gradient in the temperature determined above produces only a $\pm 10\%$ variation in the emissivity of the plasma, with greater emissivity in directions of lower temperatures.

4.5. Galactic Halo Models

Another result of this analysis concerns the fundamental distribution of hot plasma and its temperature(s) in the halo of the Milky Way. A number of other groups have based their analyses of the diffuse X-ray background on a model

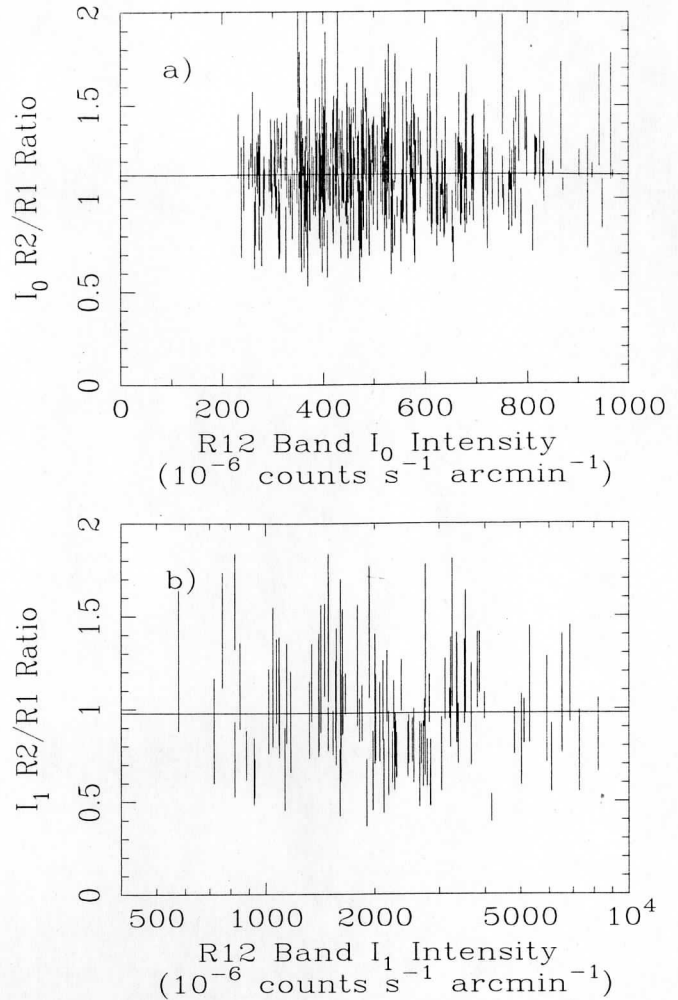


FIG. 8.—(a) Scatter plot of the fitted value for the foreground R12 band intensity vs. the R2/R1 band ratio for the foreground component. (b) Scatter plot of the fitted value for the distant R12 band intensity vs. the R2/R1 band ratio for the distant component. In both cases only values for those shadows where the ratio divided by the uncertainty in the ratio is greater than 3.0 are plotted.

where *all* of the distant Galactic emission arises from just one thermal component. This includes papers analyzing the spectrum of the diffuse X-ray background that concentrated more on the extragalactic component (e.g., Chen, Fabian, & Gendreau 1997; Miyaji et al. 1998; Parmar et al. 1999) as well as those modeling the X-ray halo of the Milky Way (e.g., Sidher et al. 1996; Wang 1997; Pietz et al. 1998). In the case of the studies focussing on the extragalactic background, the single halo component was simply used to provide a mechanism for removing the Galactic emission biasing from their determination of the extragalactic power law. However, for the studies of the Galactic X-ray halo, the fitted single halo component was used to model properties of the entire halo, usually in terms of the general Galactic potential.

If the diffuse halo X-ray emission is produced by a single-temperature component, then any variation in the ratio of the distant unabsorbed $\frac{3}{4}$ keV intensity to the distant unabsorbed $\frac{1}{4}$ keV intensity will map out variations in that temperature. For a large scale-height halo, the variation in the ratio away from the Galactic disk should be smooth over large angular scales, while the intensity of the emission

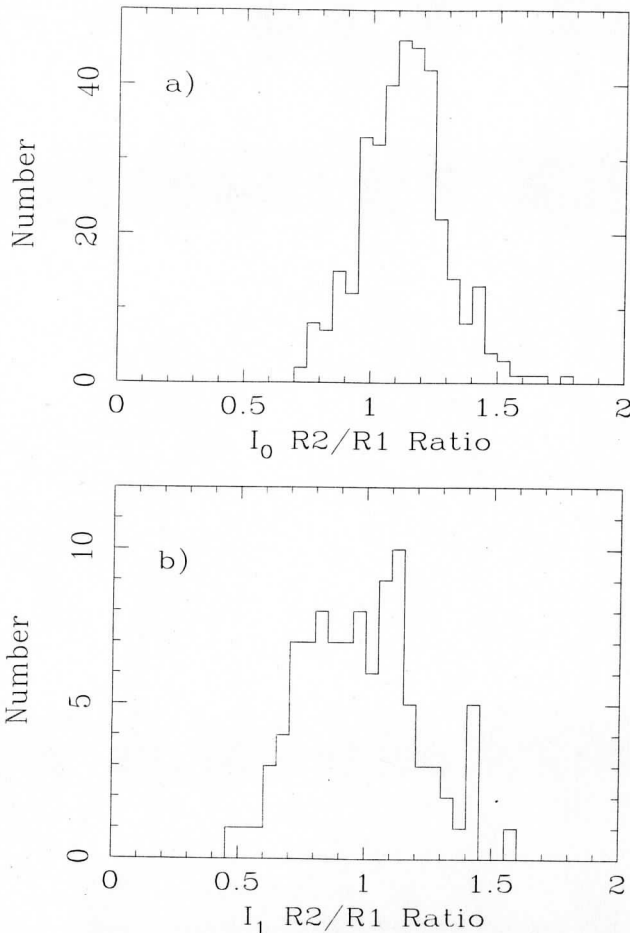


FIG. 9.—(a) Histogram of the R2/R1 band ratio for the foreground component. (b) Same as (a), except for the distant component. In both cases only values for those shadows where the ratio divided by the uncertainty in the ratio is greater than 3.0 are plotted.

should also be slowly varying. For a halo which is more dominated by local variations either associated with physical processes in the Galactic disk (e.g., fountains) or in the halo (e.g., SNRs), both the hardness and intensity of the emission could vary on relatively small angular scales.

From our analysis, the halo $\frac{1}{4}$ keV intensity is the sum of the fitted value for I_1 in the R12 band plus the model contribution from the $10^{6.4}$ K component in the R12 band. The $\frac{3}{4}$ keV intensity is just the model contribution from the $10^{6.4}$ K component in the R45 band. Figure 15 shows a scatter plot of the deabsorbed $\frac{1}{4}$ and $\frac{3}{4}$ keV intensities from the halo. To minimize the effect of large angular scale temperature variations in the halo due to a hydrostatic distribution of the plasma, we have selected data at high Galactic latitude and away from the Galactic center (i.e., $|b| > 45^\circ$ for $60^\circ < l < 270^\circ$, $|b| > 60^\circ$ otherwise). The plot does not show evidence for a convincing correlation between the two intensities, even though both vary by over a factor of 5. In addition, the plots of the $\frac{1}{4}$ keV halo intensities shown in Figures 10b and 10d do not show a smoothly-distributed halo intensity. This argues against a large scale-height halo model that has only one emission component but is consistent with a low scale-height variable (in both temperature and intensity) single component, which could also be considered as the superposition of multiple, spatially distinct components.

The adding of a second, lower temperature emission component to the model of the halo has several attractive aspects. Components at $\sim 10^{6.0}$ and $\sim 10^{6.4}$ K contribute predominantly to different bands so the structures in the $\frac{1}{4}$ and $\frac{3}{4}$ keV bands are effectively decoupled. A high scale-height, higher-temperature halo is consistent with the smoothness of the all-sky images at $\frac{3}{4}$ keV while the significant intensity variations on relatively short angular scales evident in the deabsorbed $\frac{1}{4}$ keV halo data can be interpreted as low scale-height phenomena associated with the Galactic disk. This contention of a two- (or more) component halo is supported by spectral analysis, the subject of another paper (Kuntz & Snowden 2000) that in part shows that while in any one direction it is possible to fit a single temperature component for the halo emission, it is not possible to do so in a consistent manner over the entire sky.

Figure 16 displays the relative strengths of the $\frac{1}{4}$ and $\frac{3}{4}$ keV halo emission as ellipses on the sky. In the north (Fig. 16a), the orientation of the ellipses, i.e., the band ratio of the emission, appears spatially uncorrelated except perhaps in the direction of Draco ($l, b \sim 85^\circ, 37^\circ$). In that region of bright $\frac{1}{4}$ keV emission, the ellipses tend to be vertical indicating that the average emission is relatively softer. In the southern hemisphere (Fig. 16b), the regions of bright $\frac{1}{4}$ keV emission show up as relatively narrow vertical ellipses as well. This implies that in these cases the $\frac{3}{4}$ keV emission does not track the $\frac{1}{4}$ keV enhancements. Thus, the halo $\frac{1}{4}$ keV enhancements are produced by a component that does not emit significantly at higher energies, which is consistent with a multithermal, multicomponent X-ray halo.

4.6. More Support for (at Least) a Two-Component Halo

The R2/R1 I_1 band ratio that we fit here is fairly independent of the choice of the distant spectrum (extragalactic plus Galactic halo). This is demonstrated by the consistency of our present results with those of Paper I, where the assumed extragalactic background was a much softer $E^{-1.96}$ power law scaled to produce roughly the same flux as our current harder extragalactic $E^{-1.46}$ power law plus $T = 10^{6.4}$ K thermal components. The distant emission (extragalactic power law) of Paper I was softer than our fitted halo emission, while the distant emission (extragalactic power law plus $10^{6.4}$ K thermal emission) of this paper is harder than the fitted halo. There was little effect on the fitted parameters whether the assumed extra distant emission was harder or softer than the fitted emission. We repeated the analysis assuming *no* distant emission other than the $10^{6.0}$ K halo component (i.e., no extragalactic power law or $10^{6.4}$ K thermal component) and the R2/R1 I_1 ratio remained essentially unchanged. These results indicate that where the soft halo emission is bright enough to provide a reasonable measurement of the R2/R1 band ratio, it also is bright enough to completely dominate the extragalactic and hard halo emission.

Thus there is a halo component that has a R2/R1 band ratio of ~ 0.98 , which implies a temperature of $\sim 10^{6.00}$ K. This temperature is *not* strongly dependent on the choice of thermal emission code (see Kuntz & Snowden 2000) as the current Raymond & Smith code (Raymond & Smith 1977; as incorporated into the spectral fitting package. Xspec V10.00, Arnaud 1996) indicates a temperature of $\sim 10^{6.04}$ K, while the current MEKAL code (Mewe, Gronenschild, & van den Oord 1985; Mewe, Lemen, & van den Oord 1986; Kaastra 1992; Liedahl, Osterheld, & Goldstein 1995,

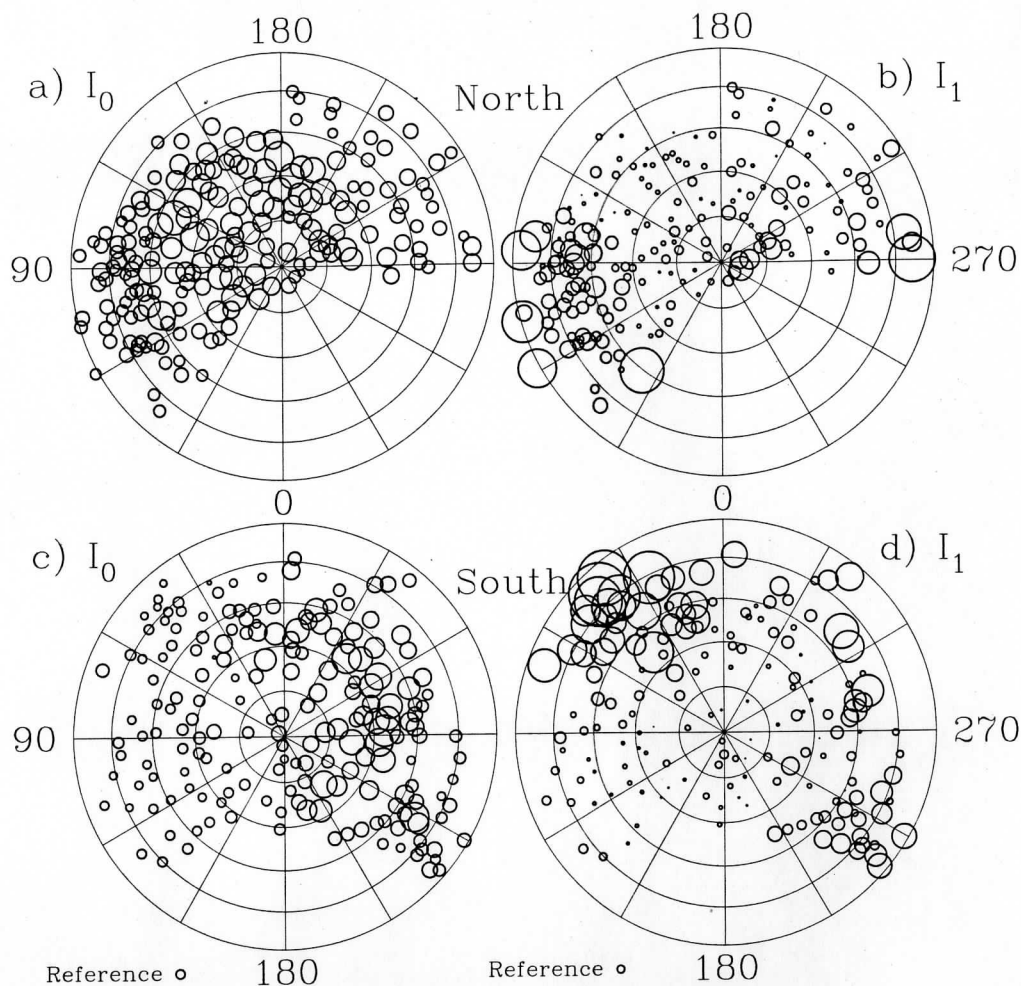


FIG. 10.—Plots showing the relative R12 band intensities of the foreground (I_0), (panels [a] and [c]) and background (I_1) [panels [b] and [d]] emission for the northern (panels [a] and [b]) and southern (panels [c] and [d]) Galactic hemispheres. The size of the circles indicates the size of the fitted values, with the reference circle for the I_0 results indicating an intensity of 300×10^{-6} counts s^{-1} arcmin $^{-2}$ and the reference circle for the I_1 results indicating an intensity of 000×10^{-6} counts s^{-1} arcmin $^{-2}$. The latitude spacing of the coordinate grid is 15° with a minimum latitude of $|b| = 15^\circ$. The longitude spacing is 30° .

as incorporated into Xspec V10.00) indicates a temperature of $\sim 10^{6.00}$ K for that R2/R1 band ratio. We note again that with current thermal equilibrium emission models it is not possible to produce the observed excess at $\frac{3}{4}$ keV over the extrapolation of the extragalactic power law with the same spectrum that produces the observed R2/R1 I_1 band ratio. In addition, as shown above, the excess at $\frac{3}{4}$ keV is not correlated with the halo emission at $\frac{1}{4}$ keV. Therefore, a second harder emission component is required to produce the observed excess at $\frac{3}{4}$ keV. However, an analysis of the spatial structure of the harder component is beyond the scope of this paper.

4.7. And Perhaps a Physical Justification for the Temperatures

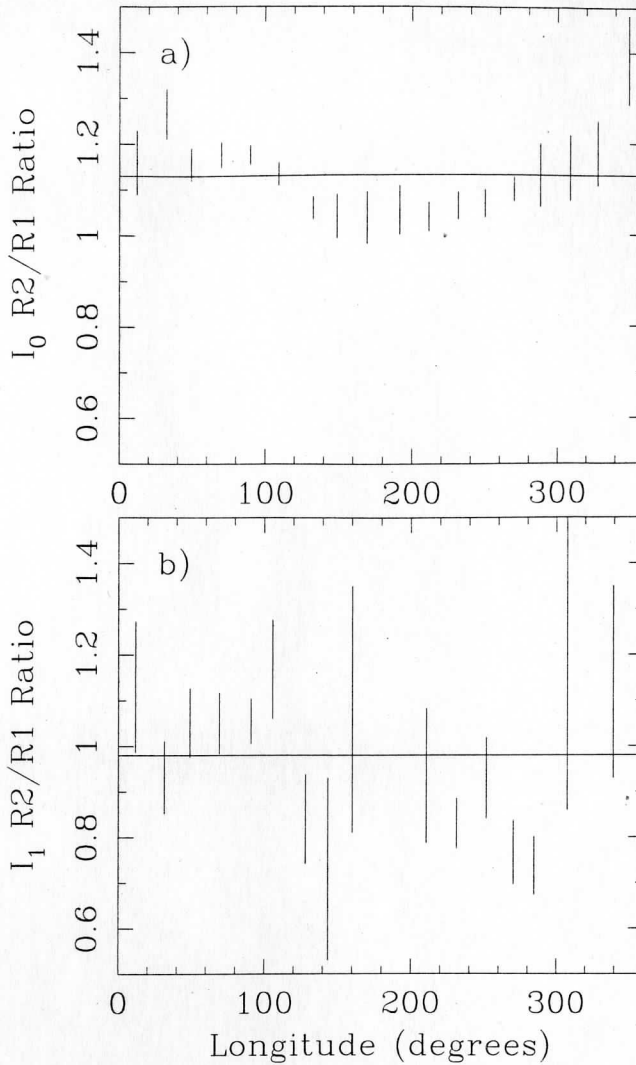
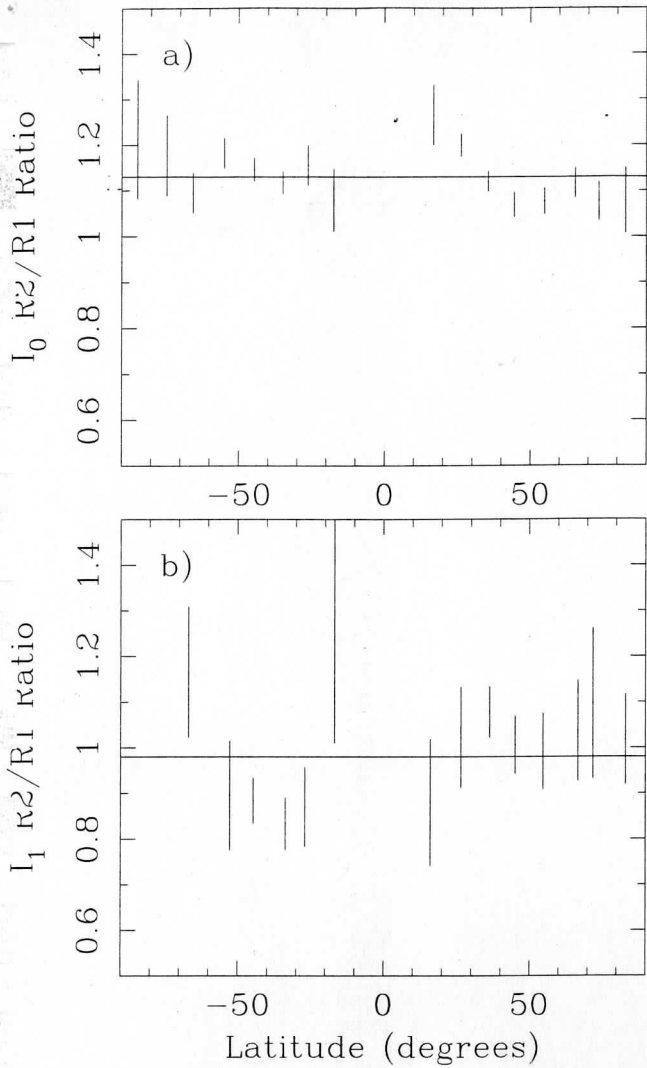
The bimodal temperature distribution may be providing important clues about the physical conditions of the X-ray-emitting plasma, which may be interpreted in terms of diffuse-plasma radiative cooling curves.⁸ Schmutzler &

Tscharnutter (1993) calculated cooling curves for isochorically and isobarically cooling plasmas. The cooling rate per unit density has two minima within the soft X-ray region, at $T \sim 10^{6.0}$ K and $T \sim 10^{6.8}$ K, with the positions of those minima dependant upon the metallicity of the plasma. Curves calculated by R. Shelton (1999, private communication) for isobarically cooling plasmas that had been shocked to $T = 10^{8.0}$ K show similar minima, with the position of the minima also dependant upon the degree of ionization nonequilibrium, and thus upon the power source and thermal history of the plasma.

For a quasi-steady state, isochorically-cooling plasmas will remain longer at temperatures around the local minima in the cooling curve than they will at other, nearby temperatures, leading to an “accumulation” of gas at those temperatures. For the isobarically-cooling case, the density of the plasma increases as the gas cools. Thus, the volumetric luminosity goes as Λn^2 , which in turn goes as ΛT^{-2} , which steepens the cooling curve and may change the local minima into no more than points of inflection.

Whether those accumulations are significant will depend upon the details of the cooling curves, which depend on metallicities, ionization states, and whether the plasma is cooling isochorically or isobarically, or more likely some state in between. Although the cooling rate per unit density

⁸ Cooling curves are traditionally plotted as the cooling coefficient (Λ) vs. gas temperature, where the volumetric luminosity coefficient $\Lambda_{vol} = \Lambda n^2$. Then for the isochoric case, by definition, the density remains constant, and $\Lambda \propto \Lambda_{vol}$, which is also proportional to the luminosity per atom. Thus, the traditional curve can be easily scaled to make a luminosity per atom vs. temperature curve.



90

90

FIG. 11.—(a) Scatter plot of the average R2/R1 band ratio for the foreground component in 10° latitude bins. (b) Scatter plot of the average R2/R1 band ratio for the distant component in 10° latitude bins. In both cases only values for those shadows where the ratio divided by the uncertainty in the ratio is greater than 3.0 were included in the plotted average.

FIG. 12.—(a) Scatter plot of the average R2/R1 band ratio for the foreground component in 20° longitude bins. (b) Scatter plot of the average R2/R1 band ratio for the distant component in 20° longitude bins. In both cases only values for those shadows where the ratio divided by the uncertainty in the ratio is greater than 3.0 were included in the plotted average.

FIG. 14. (I₀) emission intensity as a function of the size of emission shadow. See Fig. 10.

Halo R12 Intensity

0 1000 2000 3000 4000

FIG. 15. Halo R12 intensity as a function of the size of emission shadow. See Fig. 10.

is similar for both cases (Schmutzler & Tscharnuter 1993), the cooling rate per volume as noted above is very different.

The ROSAT PSPC is sensitive to soft X-ray emission through a wide range of plasma temperatures. That there are two dominant observed temperatures, and that those temperatures are near the minima of the (isochoric) cooling curves, suggests that the halo gas may be in some quasi-steady state of cooling. The strong differences in the volumetric cooling curve between isobaric and isochoric cases, as well as the changes in the cooling curves produced by metallicity and thermal history, suggest that we may be able to use the temperature distribution of the X-ray-emitting gas to understand the physical conditions of the Galactic halo.

5. CONCLUSIONS

We have presented a catalog of shadows in the ¼ keV soft X-ray diffuse background including fitted values for the foreground and background emission relative to the shadowing features for the R1, R2, and combined R12 bands. The intensities and hardness ratios for the foreground and

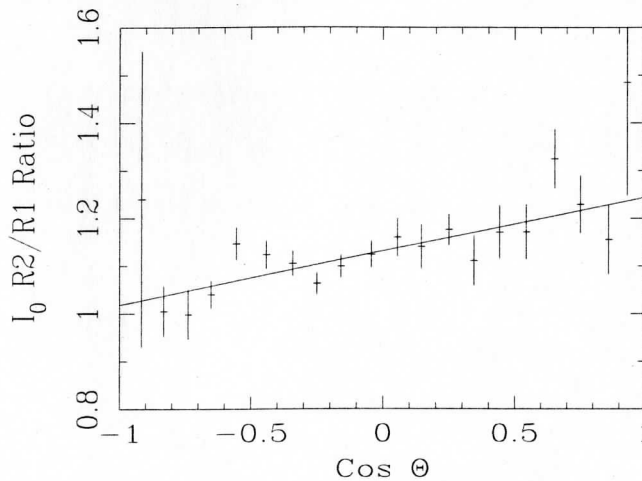


FIG. 13.—Scatter plot of the average R2/R1 band ratio for the foreground component binned by the cosine along the Snowden et al. (1990b) dipole. The line shows the best-fit linear relation between the cosine and the hardness ratio.

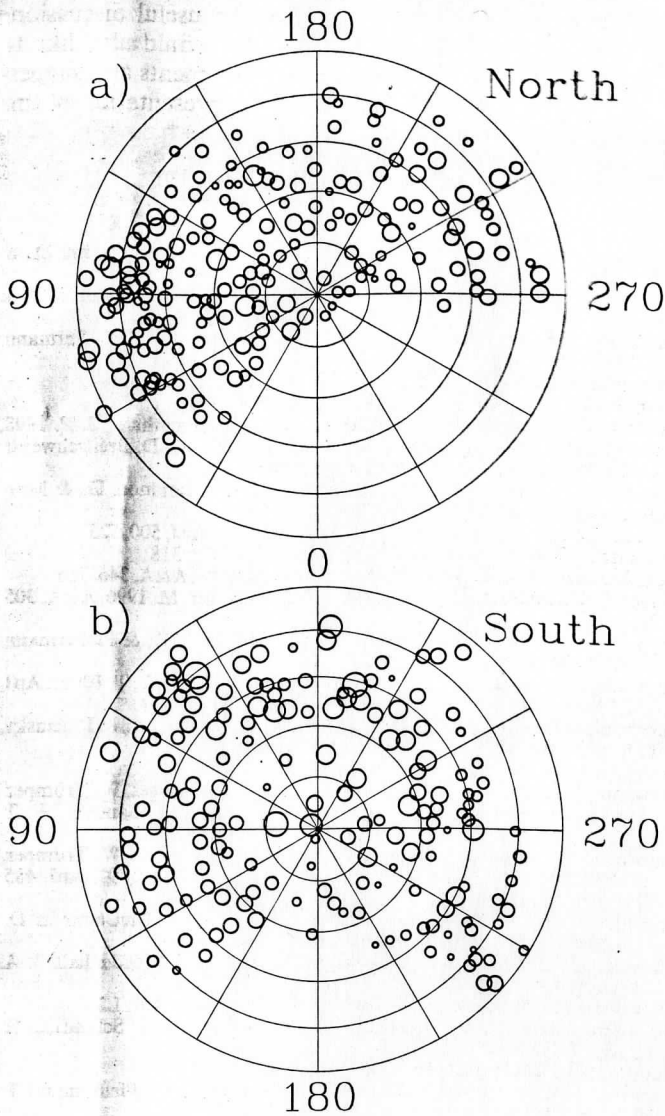


FIG. 14.—Plots showing the hardness ratios of the of the foreground (I_0) emission for the northern (a) and southern (b) Galactic hemispheres. The size of the circles indicates the hardness of the emission, with harder emission shown with larger radii. The coordinate grid is the same as in fig. 10.

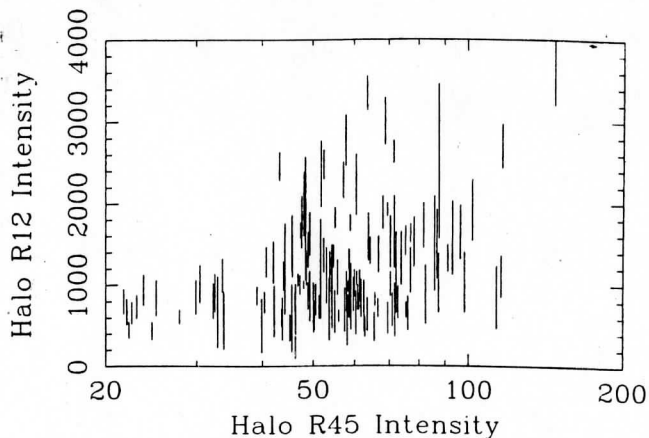


FIG. 15.—Scatter plot of the halo $\frac{3}{4}$ keV intensity vs. the halo $\frac{1}{4}$ keV intensity as determined by this analysis. The units for both axes are 10^{-6} counts s^{-1} arcmin $^{-2}$.

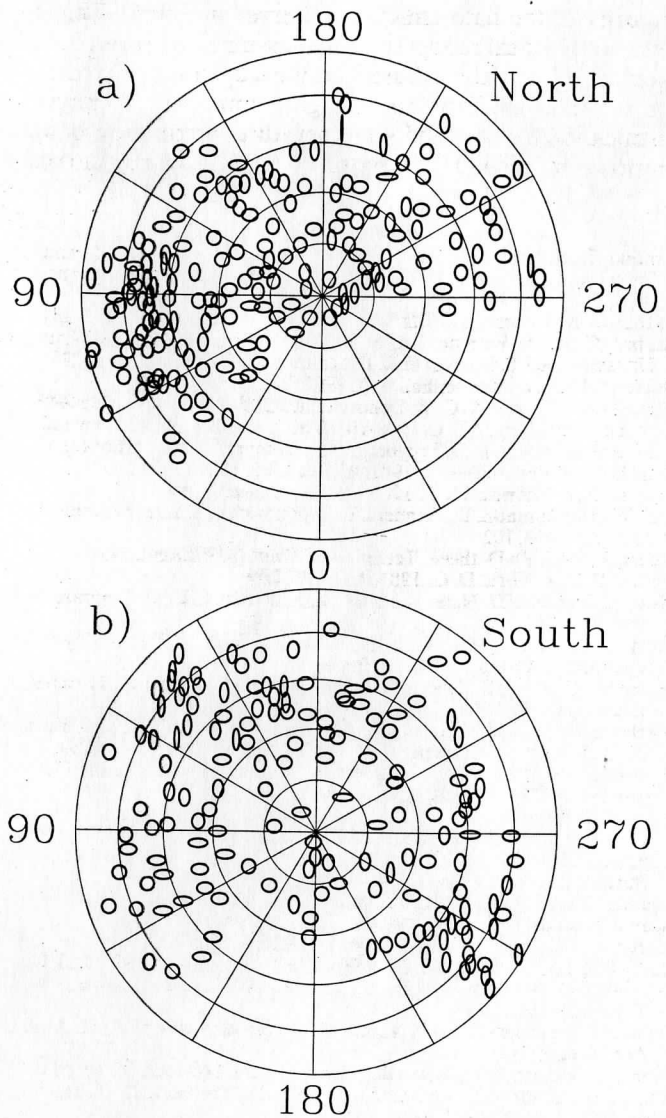


FIG. 16.—Plots of the relative halo emission in the $\frac{1}{4}$ and $\frac{3}{4}$ keV bands in the northern (a) and southern (b) hemispheres. The data are plotted as ellipses where the vertical axis is proportional to the relative emission at $\frac{1}{4}$ keV and the horizontal axis is proportional to the relative emission at $\frac{3}{4}$ keV. The data are the same as in Fig. 15 except for increased sky coverage. The coordinate grid is the same as in Fig. 10.

background components are consistent with the all-sky analysis of Snowden et al. (1998). When combined with distances to the absorbing clouds found by interstellar absorption-line measurements published elsewhere or determined by other studies, these data can aid in the mapping of the relative locations of X-ray-emitting and -absorbing material in the ISM.

The data presented here confirm the existence of a temperature gradient through the LHB first identified in Snowden et al. (1990b). The gradient is consistent with a dipole variation with the harder emission in the direction of the Galactic center. The magnitude of the effect identified here is not as great as that of the earlier paper.

Finally, examination of the Galactic halo emission at $\frac{1}{4}$ and $\frac{3}{4}$ keV strongly suggests the existence of (at least) two emission components. A hotter ($T \sim 10^{6.4}$ K) component is responsible for the bulk of the observed excess $\frac{3}{4}$ keV intensity over the extrapolation of the extragalactic power law, and a cooler ($T \sim 10^{6.0}$ K) component is responsible for the


majority of the halo emission observed at $\frac{1}{4}$ keV. This is a different physical model than that assumed by several other groups studying the diffuse X-ray background, who attribute the halo emission to a single component. A physical justification for a bimodal temperature distribution of halo plasma is provided by the nature of plasma cooling curves.

We wish to thank Robin Shelton for useful discussions concerning plasma cooling curves. We would also like to enthusiastically thank the referee for comments and suggestions, which significantly improved the presentation of this paper.

REFERENCES

- Arnaud, K. A. 1996, in ASP Conf. Ser. 10, *Astronomical Data Analysis Software and Systems V*, ed. G. Jacoby & J. Barnes (San Francisco: ASP), 17
- Barber, C. R., Roberts, T. P., & Warwick, R. S. 1996, *MNRAS*, 282, 157
- Barber, C. R., & Warwick, R. S. 1996, in *Astrophysics in the Extreme Ultraviolet*, ed. S. Bowyer & R. F. Malina (Dordrecht: Kluwer), 295
- Burrows, D. N., & Mendenhall, J. A. 1991, *Nature*, 351, 629
- Chen, L.-W., Fabian, A. C., & Gendreau, K. C. 1997, *MNRAS*, 285, 449
- Cox, D. P. 1997, in *IAU Colloq. 166, The Local Bubble and Beyond*, ed. D. Breitschwerdt, M. J. Freyberg, & J. Trümper (Springer: Berlin), 121
- Cox, D. P., & Reynolds, R. J. 1987, *ARA&A*, 25, 303
- Cox, D. P., & Snowden, S. L. 1986, *Adv. Space Res.*, 6, 97
- Cui, W., McCammon, D., Sanders, W. T., Snowden, S. L., & Womble, D. S. 1996, *ApJ*, 468, 102
- Egger, R. 1993, Ph.D. thesis, Technischen Univ. (MPE Rept. 249)
- Frisch, P. C., & York, D. G. 1983, *ApJ*, 271, L59
- Guo, Z., Burrows, D. N., Sanders, W. T., Snowden, S. L., & Penprase, B. E. 1995, *ApJ*, 453, 256
- Hartmann, D., & Burton, W. B. 1997, *Atlas of Galactic Neutral Hydrogen* (Cambridge: Cambridge Univ. Press)
- Hasinger, G., Burg, R., Giacconi, R., Hartner, G., Schmidt, M., Trümper, J., & Zamorani, G. 1993, *A&A*, 275, 1
- Herbstmeier, U., Mebold, U., Snowden, S. L., Hartmann, D., Burton, W. B., Moritz, P., Kalberla, P. M. W., & Egger, R. 1995, *A&A*, 298, 606
- Kaastra, J. S. 1992, *An X-Ray Spectral Code for Optically Thin Plasmas* (Internal SRON-Leiden Report V2.0)
- Kerp, J., Burton, W. B., Egger, R., Freyberg, M. J., Hartmann, D., Kalberla, P. M. W., Mebold, U., & Pietz, J. 1999, *A&A*, 342, 213
- Kerp, J., Mack, K.-H., Egger, R., Pietz, J., Zimmer, F., Mebold, U., & Burton, W. B. 1996, *A&A*, 312, 67
- Kuntz, K. D., & Snowden, S. L. 2000, *ApJ*, in press
- Kuntz, K. D., Snowden, S. L., & Verter, F. 1997, *ApJ*, 484, 245
- Lampton, M., Margon, B., & Bowyer, S. 1976, *ApJ*, 208, 177
- Liedahl, D. A., Osterheld, A. L., & Goldstein, W. H. 1995, *ApJ*, 438, L115
- McCammon, D., Burrows, D. N., Sanders, W. T., & Kraushaar, W. L. 1983, *ApJ*, 269, 107
- Mewe, R., Gronenschild, E. H. B. M., & van den Oord, G. H. J. 1985, *A&AS*, 62, 197
- Mewe, R., Lemen, J. R., & van den Oord, G. H. J. 1986, *A&AS*, 65, 511
- Miyaji, T., Ishisaki, Y., Ogasaka, Y., Ueda, Y., Freyberg, M. J., Hasinger, G., & Tanaka, Y. 1998, *A&A*, 334, L13
- Moritz, P., Wennmacher, A., Herbstmeier, U., Mebold, U., Egger, R., & Snowden, S. L. 1998, *A&A*, 336, 682
- Morrison, R., & McCammon, D. 1983, *ApJ*, 270, 119
- Nousek, J. A., Fried, P. M., Sanders, W. T., & Kraushaar, W. L. 1982, *ApJ*, 258, 83
- Paresce, F. 1984, *AJ*, 89, 1022
- Parmar, A. N., Guainazzi, M., Oosterbroek, T., Orr, A., Favata, F., Lumb, D., & Malizia, A. 1999, *A&A*, 345, 611
- Pietz, J., Kerp, J., Kalberla, P. M. W., Burton, W. B., Hartmann, D., & Mebold, U. 1998, *A&A*, 332, 55
- Plucinsky, P. P., Snowden, S. L., Aschenbach, B., Egger, R., Edgar, R. J., & McCammon, D. 1996, *ApJ*, 463, 224
- Plucinsky, P. P., Snowden, S. L., Briel, U. G., Hasinger, G., & Pfeffermann, E. 1993, *ApJ*, 418, 519
- Raymond, J. C. 1992, *ApJ*, 384, 502
- Raymond, J. C., & Smith, B. W. 1977, *ApJS*, 35, 419
- Sanders, W. T., Edgar, R. J., Liedahl, D. A., & Morgenthaler, J. P. 1998, *IAU Colloq. 166, The Local Bubble and Beyond*, ed. D. Breitschwerdt, M. J. Freyberg, & J. Trümper (Springer: Berlin), 83
- Sanders, W. T., Edgar, R. J., Kraushaar, W. L., McCammon, D., & Morgenthaler, J. P. 2000, *ApJ*, submitted
- Schlegel, D. J., Finkbeiner, D. P., & Davis, M. 1998, *ApJ*, 500, 525
- Schmutzler, T., & Tscharnuter, W. M. 1993, *A&A*, 273, 318
- Sfeir, D., Lallemand, R., Crifo, F., & Welsh, B. Y. 1999, *A&A*, 346, 785
- Sidher, S. D., Sumner, T. J., Quenby, J. J., & Gambhir, M. 1996, *A&A*, 305, 308
- Snowden, Burrows, D. N., Sanders, S. L., Aschenbach, B., & Pfeffermann, E., W. T. 1995a, *ApJ*, 439, 399
- Snowden, S. L., Cox, D. P., McCammon, D., & Sanders, W. T. 1990a, *ApJ*, 354, 211
- Snowden, S. L., Egger, R., Finkbeiner, D. P., Freyberg, M. J., & Plucinsky, P. P. 1998, *ApJ*, 493, 715 (Paper I)
- Snowden, S. L., & Freyberg, M. J. 1993, *ApJ*, 404, 403
- Snowden, S. L., Freyberg, M. J., Schmitt, J. H. M. M., Voges, W., Trümper, J., Edgar, R. J., McCammon, D., Plucinsky, P. P., & Sanders, W. T. 1995b, *ApJ*, 454, 643
- Snowden, S. L., Freyberg, M. J., Schmitt, J. H. M. M., Voges, W., Trümper, J., McCammon, D., Plucinsky, P. P., & Sanders, W. T. 1997, *ApJ*, 485, 125
- Snowden, S. L., Hasinger, G., Jahoda, K., Lockman, F. J., McCammon, D., & Sanders, W. T. 1994a, *ApJ*, 430, 601
- Snowden, S. L., McCammon, D., Burrows, D. N., & Mendenhall, J. A. 1994b, *ApJ*, 424, 714
- Snowden, S. L., McCammon, D., & Verter, F. 1993, *ApJ*, 409, L21
- Snowden, S. L., Mebold, U., Hirth, W., Herbstmeier, U., & Schmitt, J. H. M. M. 1991, *Science*, 252, 1529
- Snowden, S. L., & Pietsch, W. 1995, *ApJ*, 452, 627
- Snowden, S. L., Plucinsky, P. P., Briel, U., Hasinger, G., & Pfeffermann, E. 1992, *ApJ*, 393, 81
- Snowden, S. L., Schmitt, J. H. M. M., & Edwards, B. E. 1990b, *ApJ*, 364, 118
- Wang, Q. D. 1997, in *IAU Colloq. 166, The Local Bubble and Beyond*, ed. D. Breitschwerdt, M. J. Freyberg, & J. Trümper (Springer: Berlin), 503
- Wang, Q. D., & Yu, K. C. 1995, *AJ*, 109, 698
- Welsh, B. Y., Craig, N., Vedder, P. W., & Vallerga, J. V. 1994, *ApJ*, 437, 638

wisconsin astrophysics



SPECTRA OF THE $\frac{1}{4}$ keV X-RAY DIFFUSE BACKGROUND FROM THE DIFFUSE X-RAY SPECTROMETER EXPERIMENT

NUMBER 771
APRIL 2001

W. T. SANDERS
UNIVERSITY OF WISCONSIN-MADISON

R. J. EDGAR
HARVARD-SMITHSONIAN CENTER FOR ASTROPHYSICS

W. L. KRAUSHAAR
UNIVERSITY OF WISCONSIN-MADISON

D. MCCAMMON
UNIVERSITY OF WISCONSIN-MADISON

J. P. MORGENTHALER
UNIVERSITY OF WISCONSIN-MADISON

Spectra of the $\frac{1}{4}$ keV X-ray Diffuse Background from the Diffuse X-Ray Spectrometer Experiment

W. T. Sanders, Richard J. Edgar¹, W. L. Kraushaar, D. McCammon, J. P. Morgenthaler

Department of Physics, University of Wisconsin-Madison, Madison, WI, 53706

sanders@dxs.ssec.wisc.edu

ABSTRACT

The Diffuse X-ray Spectrometer (*DXS*) flew as an attached payload on the STS-54 mission of the Space Shuttle *Endeavour* in 1993 January, and obtained spectra of the soft X-ray diffuse background in the 148–284 eV (84–44 Å) band using a Bragg-crystal spectrometer. The spectra show strong emission lines, indicating that the emission is primarily thermal. Since the observations were made at low Galactic latitude, this thermal emission must arise from a nearby hot component of the interstellar medium, most likely the Local Hot Bubble, a region within ~ 100 pc of the Sun characterized by an absence of dense neutral gas. The *DXS* spectrum of the hot interstellar medium is not consistent with either collisional equilibrium models or with non-equilibrium ionization models of the X-ray emission from astrophysical plasmas. Models of X-ray emission processes appear not yet adequate for detailed interpretation of these data. The *DXS* data are most nearly consistent with models of thermal emission from a plasma with a temperature of $10^{6.1}$ K and depletions of refractory elements magnesium, silicon, and iron to levels $\sim 30\%$ of solar.

Subject headings: diffuse radiation – galaxies: Milky Way – ISM: X-rays – ISM: lines – X-rays: general – X-rays: ISM – X-rays: galaxies

1. Introduction

The diffuse X-ray background in the $\frac{1}{4}$ keV energy band (roughly 120–284 eV or 100–44 Å) has been studied for over 30 years since the initial observations by Bowyer et al. (1968), Henry et al. (1968), and Bunner et al. (1969). Although great progress has been made in determining the spatial distribution of this emission, knowledge of its spectral characteristics has lagged. An excellent review of the current state of our understanding of the hot phase of the ISM is that of Snowden (2001).

¹current address: Harvard-Smithsonian Center for Astrophysics, 60 Garden St., Cambridge, MA 02138

1.1. Spatial Structure

The angular distribution of the $\frac{1}{4}$ keV X-ray background over the whole sky has been mapped by a series of sounding rocket flights (the C band; McCammon et al. 1983), by the *SAS 3* satellite (Marshall & Clark 1984), by the *HEAO 1* satellite (Garmire et al. 1992), and by the *ROSAT* satellite (the R12 band; Snowden et al. 1995, 1997). When the counting rates of these four $\frac{1}{4}$ keV maps are compared, allowing for the different instrumental responses, they agree with each other to better than a few percent, except that the *ROSAT* count rates are consistently $\sim 10\%$ lower than expected (Snowden et al. 1995).

Three of the surveys (McCammon et al. 1983; Garmire et al. 1992; Snowden et al. 1995, 1997) produced all-sky maps at higher X-ray energies, > 500 eV, that have angular structure similar to one another but very different from that of the $\frac{1}{4}$ keV maps. One of the surveys (McCammon et al. 1983) produced an all-sky map in the lower energy 130 – 188 eV band (95 – 66 Å, the B band) that is very similar in appearance to that of the $\frac{1}{4}$ keV surveys. Sounding rocket observations of the diffuse background over ~ 1.7 sr at even lower energies (Bloch et al. 1986; Juda et al. 1991; Edwards 1990) found that the ratio of intensity in the 70 – 111 eV band (177 – 112 Å, the Be band) to that of the B band was essentially constant. These broad band all-sky data suggest a picture in which a soft component provides almost all of the intensity seen in the Be band and B band, most of the intensity in the $\frac{1}{4}$ keV band, but little of the intensity seen in the higher energy bands, which must be produced by additional components.

Inferences that can be drawn from these maps about the spatial structure of the plasma responsible for the soft X-ray component strongly depend on the absorption of the X-rays by the interstellar medium (ISM). Since the photoelectric absorption cross section varies roughly as E^{-3} , our ability to detect X-rays from a significant distance away diminishes rapidly as the energy of the X-rays decreases (see, e. g., Morrison & McCammon 1983). One absorption optical depth corresponds to a column density of neutral hydrogen, N_{H} , $\sim 10^{20}$ cm $^{-2}$ for X-rays in the $\frac{1}{4}$ keV band, to $N_{\text{H}} \sim 5 \times 10^{19}$ cm $^{-2}$ for B band X-rays, and to $N_{\text{H}} \sim 10^{19}$ cm $^{-2}$ for Be band X-rays.

Thus the ISM is opaque at low Galactic latitudes, $|b| \lesssim 30^\circ$, and the finite intensity of the X-ray background at low latitudes must be Galactic in origin and originate relatively near to the Sun, within the closest $\sim 10^{20}$ cm $^{-2}$ N_{H} . At high Galactic latitudes in the directions of lowest N_{H} , the ISM transmission rises to $\sim 60\%$ for $\frac{1}{4}$ keV X-rays and to $\sim 37\%$ for B band X-rays, but is still $< 1\%$ for Be band X-rays. The total N_{H} is $\lesssim 3 \times 10^{20}$ cm $^{-2}$ over $\sim 25\%$ of the sky, and significant contributions to the $\frac{1}{4}$ keV band from extragalactic or halo sources are possible in addition to the local emission. The detection by the *ROSAT* observatory of “shadows” in the X-ray background, localized negative correlations between the X-ray surface brightness and the ISM column density, indicates that in some high latitude directions one half to two thirds of the observed $\frac{1}{4}$ keV diffuse background X-rays originate in the halo or beyond (Burrows & Mendenhall 1991; Snowden et al. 1991).

The location of the plasma responsible for the local component of the soft X-ray diffuse back-

ground is presumed to be a cavity in the local ISM that contains the Sun. Observations of Lyman- α and neutral sodium absorption lines towards stars within 300 pc reveal that the Sun is located inside a low density interstellar cavity in the Galactic plane surrounded by a denser neutral gas boundary at a distance of roughly 120 pc, plus or minus a factor of 2 (Welsh et al. 1998; Sfeir et al. 1999). The plasma does not necessarily extend to the cavity walls in all directions in the plane, but it may extend into the halo at high Galactic latitudes (Snowden et al. 1998; Welsh et al. 1999).

1.2. Spectral Characteristics

Knowledge of the spectral characteristics of the low energy X-ray background has been limited by the energy resolution ($E/\Delta E \sim 1$) of the proportional counters used in the all-sky surveys and in other attempts to measure the diffuse X-ray background spectrum. Additional spectral information comes from the ratios of the count rates in the energy bands defined by the K-edge filters of Be, B, and C referred to earlier. The observed proportional counter pulse-height distributions and the broad-band count rate ratios of the Be band, B band, and C band are consistent with those predicted from a plasma in ionization equilibrium at a temperature near one million degrees, independent of the particular model used. Since no viable non-thermal mechanisms are apparent (Williamson et al. 1974), and there are reasons to think that the $\frac{1}{4}$ keV diffuse background could have a thermal origin (e. g., fossil supernovae; Cox & Smith 1974), the usual interpretation of the $\frac{1}{4}$ keV diffuse background is that it originates from a million degree plasma, known as the "Local Hot Bubble" (Cox & Reynolds 1987; Snowden et al. 1990, 1998), located in the local cavity in the ISM.

Models of the X-ray emission of such a hot ($10^5 \text{ K} < T < 10^7 \text{ K}$) plasma typically find that almost all of the power is in emission lines. In the $\frac{1}{4}$ keV band, it is expected that most of the emitted power should appear in the lines of highly ionized Si, Mg, and Fe, if the elemental abundances are approximately solar. If refractory elements such as these are depleted in the hot gas (e. g., contained in dust grains), as they often are in cooler regions of the ISM, lines of Ne, S, and Ar should dominate instead. In any case, a spectrometer that is sensitive to diffuse X-ray emission is needed to study the wealth of detail that is accessible in these lines about the state and history of the plasma.

2. Instrument Description

The Diffuse X-ray Spectrometer (*DXS*) experiment consists of a pair of Bragg-crystal spectrometers designed to obtain spectra of the diffuse X-ray background in the 84–44 Å (148–284 eV) range, with spectral resolution $\lesssim 2.2$ Å (4 eV at 148 eV to 14 eV at 284 eV), and angular resolution $\sim 15^\circ$. The primary objective of this experiment was to search for emission lines in the spectra of the diffuse background to verify its thermal origin, and to determine the physical condition of the hot material. Although the spectrum was expected to consist of line blends as well as lines,

comparison with model predictions could provide information about the plasma temperature, elemental abundances, ionization states, and history. The isotropy of these spectral characteristics over a limited region of the sky could also be investigated.

2.1. Physical Description

The *DXS* detector conceptual design was described by Borken & Kraushaar (1976). Detailed descriptions of the flight instrument are given by Sanders et al. (1992), Sanders et al. (1993), Morgenthaler (1998), and references therein. Figure 1 shows a cross-sectional view of a *DXS* detector assembly. Magnets were located at the entrance aperture of each spectrometer to reject low energy ($E < 20$ keV) electrons, both because such electrons can generate extraneous X-rays from surfaces that they hit, and because low energy electrons that enter the proportional counter can generate pulses that mimic low energy X-ray events. The aperture seal/baffle keeps out light, particularly solar ultraviolet, while the instrument is stowed.

The detector has three major components: the 63.3-cm radius X-ray reflecting crystal panel, the collimator, and the one-dimensional position-sensing proportional counter. Each Bragg crystal panel consists of four thin rectangular plastic sheets (0.1 cm \times 15 cm \times 36 cm) mounted next to each other (out of the page in Figure 1) whose surfaces are coated with 200 layers of lead stearate (PbSt), producing a one-dimensional pseudo-crystal with a $2d$ spacing of 101.5 Å. The geometry of the crystal panel and collimator is such that photons Bragg-reflected from the curved crystal panel are directed toward the position-sensing proportional counter with the longer wavelength photons striking it on one side and the shorter wavelength photons on the other, thus providing spectral dispersion across the counter. The collimator limits the photons entering the proportional counter to those traveling within 15° (FWHM) of the line perpendicular to the entrance window of the proportional counter in both the dispersion and cross-dispersion directions, so that there is $15^\circ \times 15^\circ$ angular resolution at each wavelength. While most of the crystal panel area is used at all wavelengths, Bragg reflection does not allow true multiplexing, and photons of different wavelengths enter the instrument from different directions on the sky, as pictured schematically in Figure 1. In order to collect photons of all energies of the instrument bandpass from the same sky direction, the detector assembly must be rotated through an angle of 65° .

The *DXS* experiment flew as an attached payload on the STS-54 mission of the Space Shuttle *Endeavour* in 1993 January. Figure 2 shows the port *DXS* instrument in its stowed position mounted on the side of the Shuttle cargo bay. The starboard instrument was located on the other side of the Orbiter, directly across from the port instrument. When collecting sky data, the instruments rotated back and forth every two minutes, detecting X-ray photons from an arc on the sky 15° (FWHM) wide, defined by the collimator, and 167° long, limited by the sills of the Orbiter cargo bay. This arc was perpendicular to the roll (tail to nose) axis of the Orbiter and was centered near the Orbiter yaw axis (perpendicular to the plane of the Orbiter wings). For all *DXS* data collection intervals during the mission, the Orbiter maintained the same inertial attitude to

within a few degrees, so that each *DXS* detector repeatedly scanned nearly the same arc on the sky. Because the PbSt may be destroyed by solar ultraviolet radiation and also by atmospheric oxygen atoms hitting it at the Shuttle orbital velocity, the *DXS* detectors scanned only during orbit night and then only when the Orbiter attitude was such that residual atmospheric oxygen was blocked by the Orbiter body from hitting the crystal panels directly.

The large area (30 cm × 60 cm) position-sensing proportional counters used in *DXS* are filled with P-10 gas, a mixture of 10% methane and 90% argon, regulated to a constant density corresponding to a pressure of 800 torr at 20 C. A thin (80 – 90 $\mu\text{g cm}^{-2}$) plastic window supported by a 100 lines-per-inch nickel mesh and the collimator structure retains the counter gas while allowing soft X-ray photons to enter the counter. The window is composed of Formvar ($\text{C}_5\text{H}_7\text{O}_2$, the registered trade name of the polyvinyl formal resin produced by Monsanto Chemical Company) with an additive, Cyasorb UV-24 ($\text{C}_{14}\text{H}_{12}\text{O}_4$, a trade name of American Cyanamide), to absorb stellar ultraviolet photons that could otherwise generate a large non-X-ray background. Once past the window, $\frac{1}{4}$ keV X-rays are absorbed photo-electrically in the first few mm of counter gas, producing a small cloud of electrons. The resulting charge cloud drifts toward the plane of 14 main anode wires, which are held at ~ 1700 V with respect to the counter body and run across the narrow dimension of the counter (along the spectrometer dispersion direction), 1.5 cm below the window. The initial charge is accelerated toward the main anodes and causes an electron avalanche when it is within a few microns of a main anode wire. The resulting charge pulse on the main anode is converted to a voltage pulse by a charge-sensitive amplifier. Below and perpendicular to the main anodes are 96 wires held at ground potential, attached to charge-sensitive amplifiers in groups of four. The induced charge distribution on the ground-plane wires is used to determine the position of the electron avalanche in the dispersion direction to ≤ 1 mm. Position determination is independent of main anode pulse height.

One anti-coincidence anode is located at each end of the main anode plane, and a plane of anti-coincidence anodes is located below the ground plane wires. In combination with position-sensing, this provides very efficient 5-sided vetoing of penetrating charged-particle events. Laboratory and flight tests show that the residual non-X-ray background is consistent with cosmic rays converting to γ -rays in the materials surrounding the proportional counter, and these γ -rays Compton scattering in the counter gas where the scattered electron escapes through the window after depositing a small fraction of its energy in the gas. The resulting spectrum is flat across the proportional counter at an average level in the 0.1 – 0.45 keV interval of $1.6 \times 10^{-4} \text{ s}^{-1} \text{ cm}^{-2} \text{ keV}^{-1}$ ($0.068 \pm 0.0007 \text{ s}^{-1}$ per detector), with variations in time of $0.5 \times 10^{-4} \text{ s}^{-1} \text{ cm}^{-2} \text{ keV}^{-1}$ (0.02 s^{-1} per detector) that depend on the Orbiter position relative to the Earth.

2.2. Instrument Calibration

In this section, we describe the *DXS* calibration measurements and estimate the accuracy of the instrument response functions that were created based on those measurements. Before the assembly

of the *DXS* spectrometers, the properties of their components were measured, and a computer ray-tracing model was used to predict the spectrometer output as a function of incident photon energy. Measurements of the instrument response to a diffuse source were made at two wavelengths before the *DXS* flight, and at three wavelengths afterwards. Table 1 gives the particular lines and their nominal energies. These measurements were compared with the predictions of the pre-assembly model. Response matrices were then constructed to enable the prediction of both the measured spectrum and the measured pulse-height distribution for a specified spectrum of incident X-rays. These response functions are logically divided into two separate functions. The photon detection efficiency function predicts how many counts are detected per incident photon $\text{cm}^{-2} \text{sr}^{-1}$, and the count redistribution matrix predicts how those counts are distributed in pulse height and, for a spectrometer, in position. In the nomenclature of the widely used X-ray spectral fitting program, *xspec* (Arnaud 1996), the photon detection efficiency function is the auxiliary response file (*arf*) and the count redistribution matrix is the response matrix file (*rmf*).

2.2.1. Area-Solid Angle Product ($A\Omega$) Calibration

Because the amount of emission from a diffuse source is characterized by its surface brightness (e. g., units of photons $\text{s}^{-1} \text{cm}^{-2} \text{sr}^{-1}$) in a wavelength interval, the appropriate measure of an instrument's response to a diffuse source is its effective area-solid angle product ($A\Omega$, in units of $\text{cm}^2 \text{sr}$ counts photon $^{-1}$, or simply $\text{cm}^2 \text{sr}$). When expressed as a function of incident photon energy, $A\Omega$ is the photon detection efficiency function described above. The calculation of the *DXS* $A\Omega$ function is described in detail by Morgenthaler (1998).

The X-ray reflection properties of lead-stearate crystals similar to those used in *DXS* were studied using a grating monochromator attached to the Tantalus II synchrotron light source at the University of Wisconsin's Physical Sciences Laboratory (PSL). At three energies across the *DXS* bandpass (151, 183, and 277 eV), the X-ray reflectivity of lead stearate was measured as a function of angle and polarization. Reflectivity at 277 eV was also measured in second order, and higher order Bragg reflection from Al K- α and O K- α was studied in our laboratory. The reflectivity of the crystal as function of angle at a particular energy was characterized as the sum of a narrow Gaussian, a wide Gaussian, and a one-sided Lorentzian, plus a specular reflection component. Parameters describing these components were determined as a function of energy and were incorporated into a ray-tracing program that calculated the instrument response up to the proportional counter window.

The proportional counter window transmissions were measured as a function of energy both pre-flight and post-flight. The post-flight window transmission was measured at 21 (port) or 32 (starboard) separate positions on the window to quantify thickness non-uniformities, but the window transmissions were found to be uniform to $\lesssim 4\%$ with no apparent large scale structure. Window transmission was modeled as a function of energy using X-ray absorption coefficients of Henke et al. (1982) and the atomic composition of the constituent window materials, $66 \mu\text{g cm}^{-2}$

Formvar and $20 \mu\text{g cm}^{-2}$ UV-24. The measured and modeled transmissions of the port instrument flight window are shown in Figure 3. The UV-24 thickness was determined independently by weighing and from the X-ray transmission of typical UV-24 layers, and the Formvar thickness was adjusted to fit the measured transmission data. The modeled transmission as a function of energy is not at all sensitive to the relative thicknesses of Formvar and UV-24, since their atomic compositions are so similar.

Using the proportional counter pulse-height model of Jahoda & McCammon (1988), the efficiency of the *DXS* proportional counters in detecting pulses corresponding to photons of a particular energy was calculated. For the analysis of the *DXS* port flight data, the lower level discriminator setting was 104 eV and the upper level discriminator was 405 eV. Figure 4 shows the pulse-height detection efficiency function for the port instrument determined with these discriminator settings. The low efficiency at low energies is due to the broad proportional counter pulse-height response distributing counts below the lower level discriminator, while the falloff at high energies is due to counts being similarly distributed above the upper level discriminator. The efficiency decreases at 50.6 \AA and at 43.7 \AA are caused by discontinuous changes in the shape and mean energy of the pulse-height distributions at the argon-L edge and the carbon-K edge, respectively, of the absorbing P-10 gas (Jahoda & McCammon 1988).

End-to-end measurements of the effective $A\Omega$ of *DXS* were made in the laboratory pre-flight at two energies and post-flight at three energies using diffuse X-ray sources produced by α -particle fluorescence from carbon, boron, and zirconium targets. Table 1 gives the particular lines and their nominal energies. As discussed in §2.2.2, the chemical environment of the target atom can broaden and shift the actual spectrum from the fluorescent target. A sheet of each target material large enough ($35 \text{ cm} \times 50 \text{ cm}$) to intercept all lines of sight to the detector in the dispersion plane over a limited range of cross-dispersion positions was used. It was exposed to an array of ^{210}Po α -particle sources positioned so as to produce a fairly uniform surface brightness of fluorescent X-rays from the target. To simulate illumination of the full *DXS* aperture with this diffuse X-ray source, exposures of it were taken at sixteen positions spanning the *DXS* detector aperture. From these exposures, the total *DXS* count rate that would be measured by the entire counter from a diffuse source filling the *DXS* aperture was determined.

The absolute calibration of the diffuse sources was performed using a small proportional counter with a well-defined area and a well-measured window. This counter was used to measure the surface brightness of the targets from 4 or 5 different strips across the target at typically 5 angles in either of two orthogonal directions from the normal. Corrections were made for the decrease of the ^{210}Po source strength over the course of these measurements due to its 138-day radioactive half life. The ratio of the *DXS* count rate over the full wavelength range of the instrument to the target surface brightness is the *DXS* $A\Omega$ measurement for a given energy of fluorescent line.

Figure 5 shows the *DXS* port instrument $A\Omega$ measurements, pre-flight at two energies (open circles) and post-flight at three energies (filled circles). The post-flight values are 5 - 6% lower

than the pre-flight values, differences that are within the $1-\sigma$ uncertainties of the measurements. Where more than one value is displayed at the same energy, the most recent value is plotted at the nominal energy and the earlier values are offset to the left for clarity.

The dashed line in Figure 5 shows the model $A\Omega$ function calculated using the pre-assembly measurements of the window thickness and of the reflectivity of the individual port instrument Bragg-crystal sheets (measured at one place on each sheet), the ray-tracing model of the instrument geometry, and the proportional counter pulse-height model (Jahoda & McCammon 1988). There are no free parameters in this model. The error bar at 68 Å attached to the "x" data point indicates the 10% uncertainty estimated for the integrated reflectivity measurements of the sheets. The solid line shows the post-flight port model $A\Omega$ function, where the crystal integrated reflectivity has been reduced by $\sim 12\%$ to better fit the measured data. The energy dependence of the crystal reflectivity was also adjusted slightly so that the net effect of both adjustments was to decrease the integrated reflectivity by a factor that varied from 10% at 42 Å to 14% at 85 Å. For the post-flight model then, two adjustable parameters were varied to fit three data points, resulting in a fit with one degree of freedom. The crystal second and third order reflectivities are incorporated in the model $A\Omega$ functions, although the data upon which they are based are not very extensive (see §2.2.4). The post-flight $A\Omega$ model is used for the scientific analysis presented here.

2.2.2. Wavelength Calibration

The $A\Omega$ measurements yielded not only a determination of the efficiency of the instrument, the number of counts per photon $\text{cm}^{-2} \text{sr}^{-1}$, but also a high statistical-precision record of the distribution of those counts in position. In combination with the ray-tracing program and the lead-stearate rocking curves measured at PSL, these data were used to create the response matrix that describes the count distribution in position. The count distribution has two main characteristics: the shape of the distribution and the location of the centroid of the counts for a given photon energy. The wavelength calibration is concerned with the latter.

The ray-tracing program in conjunction with the PSL rocking curve data was used to calculate the expected position profile on the detector for each wavelength. The position of the peak for a given wavelength is determined by the $2d$ spacing of the lead stearate and the geometry of the *DXS* instrument, which is known to within the mechanical tolerances of a few tenths of a mm. Henke et al. (1982) give the $2d$ spacing of lead stearate as 100 Å, but our PSL rocking curve measurements are better fit by 101 Å, and measurements of the spectrum of higher order Bragg reflection peaks of Al K- α give a $2d$ value of 101.5 Å. Comparison of the spectra measured in the $A\Omega$ determinations to the predictions of the calculated response matrix with different assumed values of $2d$ showed that $2d = 101.5$ Å gave the best agreement.

Comparison of the measured spectrum to that predicted by the detector model is complicated because the photon spectra arising from the α -particle-excited sources of Table 1 depend on the

chemical environments of the excited atoms and are not precisely known. Several examples of such spectra measured at high resolution are found in the literature (e. g., Bastin & Heijligers 1992; Holliday 1967; Skinner 1940) and were used as trial input photon model spectra for comparison to the measured data. Using a response matrix based on a value of $2d = 101.5 \text{ \AA}$, we find that the central peak of our measured carbon K- α line is well fit by the TiC spectrum from Holliday (1967) if the latter is shifted 0.4% to shorter wavelengths. It is also well fit by a Gaussian line with a mean of 44.6 \AA (278 eV) and $\sigma = 0.5 \text{ \AA}$ (3 eV), which is 0.16 \AA shorter wavelength (1 eV higher energy) than the nominal value (44.76 \AA , 277 eV) for the carbon K- α line (Henke et al. 1982). Our data show a long wavelength tail, extending to $\sim 60 \text{ \AA}$, that is not seen in the Holliday (1967) TiC spectrum, and is not present in our monochromator measurements at PSL.

Our measured boron K- α line also has a long wavelength tail extending to $\sim 75 \text{ \AA}$, similar to those seen in other boron K- α spectra (e. g., Bastin & Heijligers 1992; Holliday 1967; Skinner 1940), but the central peak appears to be intrinsically narrower than that of Holliday (1967), which is the narrowest elemental boron K- α line profile of those found in the literature. Using the same $2d = 101.5 \text{ \AA}$ response matrix and allowing for the shape differences, we find that the centroid of our measured boron profile is shifted 0.4% toward shorter wavelengths compared to that of Holliday (1967). In addition, the central core and short wavelength side of our boron profile can be reasonably fit by a Gaussian line with a mean of 67.84 \AA (182.8 eV) and $\sigma = 0.6 \text{ \AA}$ (1.5 eV), which is 0.2 \AA longer wavelength (0.5 eV lower energy) than the nominal value (67.64 \AA , 183.3 eV) for the B K- α line (Henke et al. 1982).

The zirconium M- ζ line profile was not found in the literature, but the main peak of our measured spectrum is quite narrow and is consistent with a Gaussian line shape with a mean of 82.1 \AA (151 eV) and $\sigma \leq 0.3 \text{ \AA}$ (0.6 eV). Our zirconium M- ζ spectrum also shows a short wavelength tail extending to $< 70 \text{ \AA}$, with some structure possibly due to weaker zirconium M lines. The value of $2d = 101.5 \text{ \AA}$ was adopted for the *DXS* response matrix because it fit the higher order Bragg reflection peaks of the Al K- α line and it gave the correct position for the Zr-M line, which was intrinsically narrow enough that uncertainty in the line profile as excited from a solid could not affect the peak position.

The solid line of Figure 6 is the product of the *DXS* response matrix and the sum of the three input functions, TiC (Holliday 1967), B (Holliday 1967), and an 82.1 \AA (151 eV) zero-width Gaussian. The data points are the three *DXS* post-flight calibration spectra from the carbon, boron, and zirconium targets, and illustrate well the tails discussed above that are associated with the lines. For this figure, the normalizations of the three input model functions were independently varied to obtain the fits to the data, but the wavelengths were not shifted. If these input functions are fit to the measured data with the normalization factors *and* wavelengths as variable parameters, the maximum wavelength adjustment required for the best fit for any of the three input models is 0.2 \AA . We therefore adopt 0.2 \AA as the accuracy of our wavelength scale.

2.2.3. Resolving Power

Using the *DXS* spectral response function, we can calculate the resolving power, $\lambda/\Delta\lambda$ (FWHM), as a function of wavelength. The results of this calculation are shown in Figure 7. The measured resolving powers of the instrument from the laboratory calibration sources are also plotted on this figure. The boron and carbon points are shown as lower limits because these lines are resolved by *DXS*. The *DXS* resolving power of 25 – 40 is a factor of 10 – 20 better than the resolving power of the proportional counters used in the *ROSAT* and Wisconsin all-sky surveys at these energies.

2.2.4. Higher Order Reflections

A dispersive spectrometer has the problem that high-order spectra fall on the same places on the detector as the first-order spectrum, and may confuse the interpretation. Although the higher-order calibration is less certain, the *DXS* $A\Omega$ function includes sensitivity for second and third order reflections, based on the PSL measurement of the 44.8 Å (277 eV) line in second order, and on our measurements of second and third order reflectivity for the O K- α and Al K- α lines. The contribution from higher orders is reduced both by the rejection of counts with pulse heights outside the 104 – 405 eV interval defined by level discriminators (see Figure 4), and by the increased photoelectric absorption in the proportional counter window of photons in the 43.7 – 20 Å (284 – 600 eV) range. These effects are accounted for in the $A\Omega$ function. Models of the diffuse X-ray background combined with the *DXS* response predict that the higher orders produce less than 2% of the total counts observed in the spectrum, and less than 7% of the counts in any position bin (see §4.6).

3. Data Collection and Reduction

3.1. Flight Operations

DXS observed a swath of the sky $\sim 15^\circ$ (FWHM) wide and $\sim 167^\circ$ long roughly aligned with the Galactic plane and centered at a Galactic longitude of $\sim 225^\circ$. This scan path covers regions of the sky typical of the diffuse X-ray background as well as the Vela and Monogem supernova remnants. Figure 8 shows the *DXS* port instrument exposure pattern superimposed on the $\frac{1}{4}$ keV map of the *ROSAT* all-sky survey (Snowden et al. 1997).

During each shuttle night-time pass, the *DXS* detectors were rotated from their stowed positions and scanned 8 to 10 times across the region of the sky shown in Figure 8. The proportional counter high voltage was turned on a few minutes before each scan period and left on for a few minutes afterwards for instrument background measurement. Before and after each scan, the proportional counter gas gains were measured using an on-board aluminum-anode X-ray tube. A charge pulser was used to measure the amplifier electronic gains and offsets several times during

the mission.

The amplifier gains and offsets remained steady to within 0.5% throughout the flight, but the proportional counter gas gain decreased by about 20% over the course of the mission. The pulse heights were gain-corrected by multiplying the measured pulse height by the ratio of the nominal aluminum K- α pulse height to the average aluminum K- α calibration pulse height for that orbit. The pulse heights were also corrected for position-dependent gain variations across the counter. Software upper and lower discriminator levels were applied to select a fixed range of corrected pulse heights, so that the detection efficiency was independent of gain. This required choosing a software lower discriminator level high enough in corrected pulse height, 104 eV, that it never was less than the value of the corrected hardware lower discriminator, which was 70 eV at the nominal gain.

Breakdown in the starboard proportional counter has made extraction and interpretation of usable data from the starboard instrument difficult (Morgenthaler 1998). The amount of usable data from the starboard counter is less than half that from the port counter, and although the starboard data are consistent with the port data, their inclusion in these analyses would introduce systematic uncertainties greater than the decrease in statistical uncertainties. For these analyses we consider only data from the port instrument. Figure 9 shows a plot of the total count rate as a function of time in the port instrument. The count rate of orbits 51 – 90 is 17% less than the count rate of orbits 7 – 50, an effect that is not understood. After eliminating other possible causes (cosmic rays, soft electrons, gas amplification gain, pulse-height distribution shape, electronics dead time correction, occultation of the instrument aperture, atmospheric absorption, or change in instrument sensitivity), Morgenthaler (1998) suggests that a long term enhancement (LTE, see Snowden et al. 1995), similar to those observed during the *ROSAT* All-Sky Survey may be responsible. LTEs appear to be due to X-rays that originate between the Earth and the Moon, that can occasionally be as strong as the cosmic background in the $\frac{1}{4}$ keV band, that may last for days, that are uncorrelated with orbital or geographic parameters, and for which no physical mechanism has been determined. The only *DXS* parameter that shows a behavior similar to the count rate decrease is the port detector gas gain, which shows a 13% drop after orbit 41 compared to prior orbits, but this gas gain is only slightly correlated with the count rate. Regardless of the cause of the changing count rate, the average count rate was used for the analysis presented here.

3.2. Data Reduction

Although an arc of the sky 167° long was visible from the locations of the *DXS* detectors, the 15° (FWHM) field of view was partially occulted by the upper part of the Orbiter cargo bay wall at either end of that arc, so that only 137° of the *DXS* scan, $297^\circ > l > 160^\circ$, was fully exposed. The 30° arcs at either end of the scan path, $327^\circ > l > 297^\circ$ and $160^\circ > l > 130^\circ$ are partially occulted, and the data from these directions are not used in the spectral analysis here. Since a *DXS* detector must execute a complete 65° scan across a sky direction to obtain full wavelength

coverage from that direction, the ends of the scan path have only partial wavelength coverage. Thus, the wavelength coverage increases from no coverage at $l \approx 336^\circ$ to full coverage at $l \approx 271^\circ$, and decreases from full coverage at $l \approx 175^\circ$ to no coverage at $l \approx 110^\circ$. Since the detector is already fully occulted for $l < 130^\circ$ and $l > 327^\circ$, the scanning data in these ranges provide an independent measurement of the detector background.

For the *DXS* data analysis, counts were selected whose corrected pulse heights were in the range 104–405 eV with spectral positions in the 84–42 Å (148–295 eV) range, and whose charge distributions across the position-sensing ground plane wires were consistent with the expected shape. To create a one-dimensional map of the sky brightness measured by *DXS*, the data satisfying these criteria were projected onto the sky. For each of 200 spectral positions across the position-sensitive proportional counter, detected counts and exposure times were accumulated into one-dimensional arrays of bins along the *DXS* scan path. For each 1-second time interval, for each position along the counter, the appropriate direction on the sky was determined, and the detected counts and the live time were added to the 1° wide bin containing the center of the field of view at the middle of the time interval. For this display, spectral information was not retained. The count array was divided by the exposure array to give counts s^{-1} position $^{-1}$, and this was multiplied by the 200 positions per detector to yield a one-dimensional map of count rate, including background. This count rate is really an “equivalent” count rate, since ignoring spectral information results in non-uniform spectral weighting where the wavelength coverage is not complete at Galactic longitudes greater than 271° and at Galactic longitudes less than 175° . The data points on the lower plot in Figure 10 show the equivalent count rate as a function of Galactic longitude, and the solid line of the upper plot gives the Galactic latitude of the center of the field of view as a function of Galactic longitude.

The *DXS* data were divided into sets defined by intervals along the scan path that correspond to five different regions on the sky. Figure 10 indicates the boundaries of those regions. The residual instrument background rate of 0.068 s^{-1} ($1.6 \times 10^{-4} \text{ s}^{-1} \text{ cm}^{-2} \text{ keV}^{-1}$), caused mainly by cosmic rays, is indicated as the dotted line in Figure 10. This background level was measured when the instrument was in its stowed position with the aperture completely covered. When the instrument scanned beyond the Crux or Auriga regions, where the shuttle cargo bay occulted the instrument field of view but the aperture was still open, the count rate fell to the same background level. This indicates that additional sources of background, such as low energy electrons, are not present in the scanning data. The arrows in Figure 10 indicate the Galactic longitudes where the field of view was fully occulted by the Orbiter.

A model of the *DXS* angular sensitivity was approximated by propagating the $15^\circ \times 15^\circ$ collimated field of view of each position on the counter through the same 38° Bragg reflection off the curved crystal panel onto the sky. This sensitivity function was scanned across the *ROSAT* $\frac{1}{4}$ keV band map (Snowden et al. 1995) according to the *DXS* flight aspect data. The Snowden et al. (1995) map was used for this scan instead of the Snowden et al. (1997) map because point sources were removed from the latter map but not from the former. The resulting *ROSAT* count

rates were scaled to produce a predicted *DXS* count rate using the ratio of the calculated count rate in the *ROSAT* $\frac{1}{4}$ keV band to that in the *DXS* 84 – 42 Å (148 – 295 eV) spectral range. This ratio, 1318, was determined using the model spectra of equilibrium plasma emission described in §4.2, and varies only a few percent depending on the thermal spectral model type or its assumed elemental abundances. The solid curve on the lower plot in Figure 10 shows the sum of the *ROSAT*-predicted *DXS* count rate and the measured *DXS* non-X-ray background rate. Excluding the Crux and Vela regions, the *ROSAT*-predicted *DXS* count rate averages 10% lower than the measured *DXS* count rate, consistent with the suggestion of Snowden et al. (1995) that the published effective area of the *ROSAT* $\frac{1}{4}$ keV band response function is about 10% high, although LTEs may contribute some excess *DXS* counts. The difference between the two rates in Vela appears to be due to the rather different X-ray spectrum of the Vela region, while in the Crux region it appears to be due to the incomplete spectral coverage and non-uniform spectral weighting at the ends of the *DXS* scans.

3.3. Region-by-Region Spectra

Spectra were extracted from each of the five regions indicated in Figure 10. These are shown in Figure 11 after non-X-ray background has been subtracted and flat-field corrections have been made. The partial wavelength coverage at the ends of the scans has negligible impact on the Auriga and Vela spectra, but results in the Crux spectrum having no spectral coverage longward of 76 Å. The Vela spectrum is clearly quite different from the others, and will be discussed in a subsequent paper (Morgenthaler et al. 2001, in preparation), along with the Monogem spectrum. Of the other spectra, Crux and Auriga are statistically indistinguishable, as indicated by a χ^2 test with no free parameters. When the Puppis spectrum is scaled to the same total count rate, no statistically significant difference in shape is found between it and the Crux and Auriga spectra. In order to simplify subsequent analysis and increase our statistical precision, we have combined the data from the Crux, Puppis, and Auriga regions to form a Hot Interstellar Medium (HISM) spectrum, shown in Figure 12.

4. Data Analysis

We have attempted to fit a range of simple and moderately sophisticated standard models to the *DXS* port instrument HISM spectrum, and find no model that satisfactorily fits the data. Since this spectrum is a combination of the Crux, Puppis, and Auriga regions, and excludes the Puppis and Vela supernova remnants and the Monogem Ring (also a supernova remnant), the spectrum obtained is presumed to be typical of the low Galactic latitude diffuse background, dominated by X-ray emission from the Local Hot Bubble. We consider several classes of models. First we look at continuum spectra, then collisional equilibrium thermal spectra, and then we consider a class of non-equilibrium thermal models. We explore the reasons why such efforts fail, examining differences between X-ray emission codes.

4.1. Maximum Flux Fraction due to a Smooth Continuum

Although X-rays from the Local Hot Bubble are thought to arise from a million-degree plasma whose emission consists almost totally of a large number of lines, this may not be true. As the *DXS* resolution is not sufficient to resolve all the lines that standard models suggest are present in its bandpass, it is possible that the spectrum consists of a smooth continuum underlying a few isolated lines. In order to assess the fraction of the observed flux that must come from spectral emission lines or other sharp spectral features, we have fit a power law to the *DXS* HISM spectrum. We then decreased the normalization of this power law until the modeled spectrum no longer exceeded the data at any point, giving $0.75 E^{-3.2}$ photons $\text{s}^{-1} \text{cm}^{-2} \text{sr}^{-1} \text{keV}^{-1}$, where E is the energy in keV. The modeled flux equals that of the measured spectrum at several widely separated wavelengths, and is a good approximation to the greatest smooth continuum that may underlie the line spectrum. We find that this greatest smooth continuum can account for about 68% of the flux observed by *DXS*. Although there is no reason to think that it is not all thermal, as a very conservative lower limit, at least 32% of the 84 – 44 Å flux comes from sharp spectral features such as lines.

Another possible variety of continuum, from recombination processes, may contain step discontinuities at the ionization energies of the ions in the gas. Breitschwerdt & Schmutzler (1994) suggest that much of the diffuse X-ray background flux may come from recombination radiation. We therefore constructed a model consisting of recombination edges from ions present in plasmas at temperatures $\lesssim 10^7$ K. No combination of electron temperatures and recombination time scales produced a fit as good as the equilibrium thermal model fits discussed in the next section.

4.2. Collisional Equilibrium Plasma Models

Because X-rays from the Local Hot Bubble are thought to arise from a million-degree plasma, collisional equilibrium thermal plasma models appear to be the natural models to fit to the *DXS* data. The appropriate elemental abundances for those plasma models are not obvious, however. Smith et al. (1996) show that dust-bearing gas heated to temperatures $\lesssim 10^6$ K will cool before most of the dust is sputtered. It is therefore possible that some dust survives in the hot gas responsible for the X-ray emission, which would result in depletion of refractory elements. This is in accord with the observations of Bloch (1988), Bloch et al. (1990), and Jelinsky et al. (1995), which suggest depletions of refractory elements within the X-ray emitting gas, and with the fact that many supernova remnants, which emit strongly in X-rays, also emit strongly in the infrared due to hot electrons interacting with dust grains (Dwek 1987). For the fits presented in this section, we consider three different sets of elemental abundances.

The intent of this section is to present fits of single temperature collisional-equilibrium ionization (CEI) plasma models to the *DXS* data. We found, however, that if we fit single temperature CEI models to the *DXS* spectral data alone, we can obtain good fits with models that violate observational constraints at energies outside the *DXS* band. Typically, they make too many X-rays in

the 0.5 – 1 keV band. To address this difficulty, we instead fit a more complete model of the diffuse X-ray background to the *DXS* data and simultaneously to the Wisconsin sky survey data (seven broad bands covering 0.13 – 6 keV; McCammon et al. 1983) to constrain the X-ray fluxes at higher energies. A three-component model has been used previously to fit the diffuse background at X-ray energies up to several keV: an unabsorbed thermal equilibrium model where $T \approx 1 \times 10^6$ K; an absorbed thermal equilibrium model with a temperature higher by a factor of 2 – 3; and an absorbed power law of the form $11 E^{-1.4}$ photons $s^{-1} \text{ cm}^{-2} \text{ sr}^{-1} \text{ keV}^{-1}$, where E is in keV (Burstein et al. 1977; Burrows 1982; Garmire et al. 1992; Kuntz & Snowden 2000). Accordingly, we simultaneously fit the *DXS* HISM spectrum, the *DXS* pulse-height distribution, and the Wisconsin sky-survey band count rates (McCammon et al. 1983) with a model of the form

$$M = E_{m,1}\Lambda(T_1) + e^{-\sigma N_H}(E_{m,2}\Lambda(T_2) + 11 E^{-1.4}), \quad (1)$$

where $\Lambda(T_i)$ is a thermal plasma emission model in coronal equilibrium at temperature T_i , $E_{m,i} \equiv \int n_e^2 dl$ is the emission measure for gas with temperature T_i , N_H is the column density of neutral hydrogen (here assumed to be $1 \times 10^{21} \text{ cm}^{-2}$), and σ is the energy-dependent interstellar medium cross section (Morrison & McCammon 1983). The fitting was done with the *xspec* program (Arnaud 1996) using two different thermal plasma emission model codes, that of Raymond & Smith (1977, as updated in 1993; hereafter RS) and that of Mewe et al. (1995, with $\frac{3}{4}$ keV band iron emission computed by Liedahl; hereafter MEKAL). The energy resolution of the RS model was increased by recomputing it on 0.5 eV energy bins across the *DXS* bandpass (including high orders). These models are discussed further in §4.4.

In our fits, we studied three cases of elemental depletions for the unabsorbed (local) component: [1] solar abundances of Anders & Grevesse (1989) with no depletions; [2] solar except for Mg, Si, and Fe, whose relative depletion was kept the same but allowed to float freely (labeled MgSiFe in Table 2); and [3] solar except for Mg, Si, and Fe, whose relative depletions were allowed to independently float freely (labeled “variable” in Table 2). These three elements were selected because they are refractory, abundant, and have many lines in the 84 – 44 Å band. We summarize the results of our fits of the model described by equation (1) to the *DXS* and Wisconsin sky survey data in Table 2 and Figures 13 and 14. In no case is the reduced χ^2 statistic less than 2.7, so none of the fits is formally acceptable, but visual inspection of Figure 14 indicates that the variable abundance MEKAL model is a good approximation. For any of the fits, the unabsorbed lower temperature model component provides > 95% of the observed counts in the *DXS* band, and is effectively the best fit of a single-temperature collisional-equilibrium model to the *DXS* data.

Since collisional equilibrium thermal plasma models fail to account for the HISM spectrum, we proceed to consider other types of models and comparisons.

4.3. Non-Equilibrium Plasma Models

Section 4.1 indicates that the *DXS* HISM spectrum shows strong emission lines. Section 4.2 shows that current single-temperature collisional equilibrium plasma models do not fit the *DXS* data well, even if elemental abundances are allowed to vary. In principle, non-equilibrium ionization (NEI) model spectra can be quite different from equilibrium ones, as a different set of spectral lines are produced due to the presence of ions different from those common in equilibrium at a given temperature and due to a different balance between the collisional and recombination processes that populate excited states. Such models allow for greater variety at the expense of additional parameters. However, we find similar results from both equilibrium and NEI models with temperatures $\sim 10^6$ K: if they meet the constraints from the broad band fluxes (especially in the $\frac{3}{4}$ keV band), they cannot fit the *DXS* spectrum. This section presents the fits of a particular set of non-equilibrium models to the *DXS* data.

The picture of the diffuse X-ray background discussed in §1 supposes that the Sun is inside a cavity that has been formed by one or more supernova explosions. Each supernova explosion shock heats the ambient gas in the interstellar medium and enlarges the boundary of the bubble. The equilibration time for the kinetic temperature in the gas is short compared to the ionization time, so the ionization state of the gas lags the kinetic temperature, and the gas is under-ionized. Edgar & Cox (1993) model the details of X-ray production in the single supernova explosion case and find that it is difficult to match even broad band observational parameters. Smith (1996) and Smith & Cox (2001, hereafter SC01) have modeled emission from multiple older co-located supernova explosions. The supernova explosions are separated by $1 - 2 \times 10^6$ years and the current epoch is $4 - 8 \times 10^6$ years after the first explosion. As the gas expands, and cools both adiabatically and by thermal conduction, it becomes over-ionized and then approaches equilibrium. The models include thermal conduction in the gas, the effects of dust cooling and sputtering, and the possibility of spatially varying abundances. SC01 find that models consisting of two or three supernova explosions fit the Wisconsin all-sky survey B and C band rates (McCammon et al. 1983) and other observational parameters reasonably well. However, comparison with the *DXS* HISM spectrum produces $\chi^2_\nu \gtrsim 7.9$.

The appearance and goodness-of-fit of the SC01 models are similar to those of the equilibrium solar-abundance RS model shown in Figure 13, particularly in the lack of emission at $64 \lesssim \lambda \lesssim 68$ Å. This is because the atomic physics calculations used in the SC01 models are the same as those used in RS. Also, several million years after the last explosion, the gas in the SC01 model is near equilibrium.

Thus, it is possible that the poor fit of the SC01 models to the *DXS* data is due to inadequate atomic physics data and models used to generate the X-ray spectra and not to any intrinsic shortfalls in the SC01 astrophysical model. Because the *DXS* calibration data fit the instrument model with good accuracy, we attribute the lack of a good fit by both equilibrium and non-equilibrium models to the astrophysics or to the atomic physics data, and not to the *DXS* instrument model.

4.4. The Atomic Data and Models

Since we are unable to fit straightforward models from the existing plasma emission model codes to the *DXS* HISM spectrum, we proceed to examine the contents of the models. We do this for two reasons: an attempt to identify features in the spectrum, and an attempt to derive a synthetic spectrum that is consistent with the data (and that perhaps will suggest new types of astrophysical models).

Current models of emission spectra from coronal plasmas such as the RS model and those of Mewe et al. (1985, 1986), Kaastra (1992), and MEKAL indicate that the expected lines in the $\frac{1}{4}$ keV band are predominantly of two categories. The first category consists of L-shell lines of elements from neon to argon. These lines are the analogs of the Fe L-shell lines in the 0.7 – 1.2 keV energy band, *i. e.*, $n = 3 \rightarrow 2$, $n = 4 \rightarrow 2$, and higher transitions. The second category of expected lines are M-shell lines of Fe ions and the ions of other iron-group elements.

To see which ions contribute lines in what parts of the spectrum, we extracted from the RS and MEKAL codes model spectra of single ions of the elements Ne, Mg, Si, S, Ar, Ca, Fe, and Ni that have lines in the *DXS* band. In many cases, the line ratios within the 84 – 44 Å band are not very temperature sensitive (although the absolute emissivity is). If these theoretical spectra are representative of coronal spectra from nature, they represent a set of approximate basis functions from which astrophysical spectra must be built. That is, a model with minimal astrophysical prejudice can be constructed from a linear combination of these spectral basis functions. Tradeoffs between various ions with nearly coincident lines can then be assessed, and astrophysical conclusions can be drawn from the relative normalization factors for the spectra of the ions of each element.

As an example of what is learned by comparing these spectra to the *DXS* data, we discuss the attempt to identify the strong emission feature that appears at 67.4 Å in the *DXS* HISM spectrum. The MEKAL spectrum of Ne VIII has one very strong line blend in the *DXS* band, which occurs at 67.4 Å, plus a few weaker lines. To explore the conjecture that the 67.4 Å feature in the HISM spectrum might be produced by this Ne VIII line, we also looked at the RS spectrum of Ne VIII, and found that there the strongest line falls at 70 Å, and that there are also lines with a large fraction of the intensity of the 67.4 Å line at 61 Å and at 74 Å. To try to resolve these differences, new computations were obtained of the spectrum of Ne VIII (and a few other ions) at temperatures near 10^6 K from D. A. Liedahl (private communication), who used the HULLAC code (Klapisch 1971). The RS and MEKAL models of Ne VIII each have four lines in the 84 – 44 Å band, the compilation of Kelly (1987) lists 23 lines, and Liedahl finds that 13 of the 17 lines included in his calculation contribute significantly in the *DXS* band. The Liedahl calculation shows a strong blend of lines ($4p \rightarrow 2s$ transitions) at the proper wavelength to match our 67.4 Å feature, but it also shows, twice as strong, a line blend near 74 Å ($4d \rightarrow 2p$ and $4s \rightarrow 2p$ transitions). The ratio of these lines is not very sensitive to the temperature. If these computations are accurate, it is highly unlikely that Ne VIII is the source of the 67.4 Å feature in the *DXS* HISM spectrum, since a stronger line blend around 74 Å should be present, but is not observed.

Liedahl (1999) suggests that the Fe IX $5d \rightarrow 3p$ transitions also occur very close to this wavelength, and should be considered. However, there are much stronger Fe IX lines ($4d \rightarrow 3p$ transitions) elsewhere in the band, near 82.5 and 83.5 Å in the Liedahl/HULLAC model. Unless the wavelengths of these lines are in error by several Å and are beyond the soft end of the *DXS* band, or their intensity relative to that of the 67.4 Å line is in error by more than a factor of 5, Fe IX cannot be responsible for a significant fraction of this spectral feature.

Similar considerations have ruled out a great many other possible line identifications, with candidates being taken from Kelly (1987). The solar spectra of Acton et al. (1985) and Malinovsky & Heroux (1973) both have features near this wavelength (see §4.5). Acton et al. (1985) identify the feature as a blend of Ne VIII $\lambda 67.38$ and Mg IX $\lambda 67.24$, while Malinovsky & Heroux (1973) give Fe XVI $\lambda\lambda 66.2, 66.3$ for their slightly shorter wavelength feature. The Mg IX candidate is ruled out because stronger lines from the same ion at 73.0 Å are not seen in the *DXS* spectrum. The presence of Fe XVI in general implies the existence of large amounts of Fe XVII, whose strong lines in the $\frac{3}{4}$ keV band are several times brighter than the total flux detected in this direction by the Wisconsin, *HEAO 1*, or *ROSAT* all-sky surveys. The 67.4 Å feature remains unidentified at this time.

Given the wide variation between different computations of the spectra of the same ions under the same conditions for most of the ions that have strong lines in this band, it appears that new, more accurate, calculations of the spectra of relevant ions are needed to make sense of the 84–44 Å band spectra of the diffuse X-ray background (or any other astrophysical source). This effort will be aided by the *Chandra X-ray Observatory* Emission Line Project, which has taken deep grating spectra of relatively well-understood bright stars in an attempt to benchmark the astrophysical plasma emission codes. In a subsequent paper (Edgar et al. 2001, in preparation), we will use new calculations by Liedahl of the spectra of these ions to make astrophysical inferences about the *DXS* spectra.

Similar discrepancies between the models and astrophysical and laboratory spectra have been noted before, especially in the $\frac{3}{4}$ keV band. For example *EUVE* spectra of *Capella* allow one to model the distribution of emission measure *vs.* temperature (Brickhouse et al. 2000). Using this emission measure distribution and existing spectral models to synthesize a model X-ray spectrum for comparison with the simultaneous *ASCA* observation, it is clear that the accuracy and completeness of the Fe L-shell lines in the existing plasma X-ray emission codes (RS or MEKAL) is not adequate for interpreting modest resolution X-ray spectra ($E/\Delta E \lesssim 30$), as obtained for example with CCDs having resolution in the $\frac{3}{4}$ keV energy band similar to that of *DXS* in the 84–44 Å band. Many weak lines resulting from transitions up to $n = 7 \rightarrow 2$ must be included to obtain an adequate fit. The situation is being improved for the Fe L-shell lines (Liedahl et al. 1995), but similar work needs to be done on the lines of Ne, Mg, Si, S, and Ar in order to interpret spectra of astrophysical objects in the $\frac{1}{4}$ keV band. The discrepancies in the Fe L-shell lines are also observed under laboratory conditions. Liedahl (1999) points out differences between existing predictions and measurements made with the Electron Beam Ion Trap (EBIT) at Lawrence Livermore National Laboratory.

Not only are the currently available atomic data inadequate, but in many instances the treatment of the data within the existing plasma X-ray emission codes is also not adequate. The existing models were designed with lower energy resolution in mind, in part to accommodate the limitations of the computers available at the time the codes were conceived. For example, in many cases a multiplet of lines was grouped into a single "line," in the RS code as well as in the MEKAL code, in an effort to get the right flux at about the right energy, an approach that was entirely adequate for instruments with proportional counter resolution ($E/\Delta E \lesssim 5$).

4.5. Comparison to Solar X-Ray Spectra

We have compared the measured *DXS* spectra to solar spectra in the same wave band with similar or higher spectral resolution to see if the line identifications of the solar spectra could help with those of the *DXS* spectrum, as was attempted for the 67.4 Å feature discussed in §4.4. Figure 15 presents three spectra of the solar corona, a plasma with $T \sim 10^6$ K, folded through the *DXS* response, and plotted along with the *DXS* HISM spectrum. The solar spectra are normalized such that the strength of the strongest line in the spectrum is similar to that of the strongest line of the *DXS* spectrum. The spectra of Malinovsky & Heroux (1973) and Acton et al. (1985) have only partial spectral coverage, $\lambda > 60$ Å and $\lambda \lesssim 80$ Å, respectively. The differences among the solar spectra may be explained by the fact that the Sun is not a quiescent object. The Malinovsky & Heroux (1973) spectrum is of the full disk, while that of Acton et al. (1985) is of a solar flare. The Doschek & Cowan (1984) spectrum is a composite line list, drawn from many measurements and theoretical calculations. It seems clear from these figures that the solar spectra are not that similar to the *DXS* spectra, which is not very surprising since the physical conditions in the hot interstellar medium are rather different from those in the Sun. As a result, the solar spectra were not helpful in the identification of features in the *DXS* spectrum.

4.6. Fit to Multiple δ -Functions

Since no straightforward astrophysical models computed with existing plasma emission codes can be made to fit the *DXS* HISM spectrum, we have fit it with an artificial spectrum consisting of a number of narrow spectral lines of selected wavelengths. Lines were added to the model one at a time, at the wavelength where the residual between the data and the model was greatest, until the reduced χ^2 fell below 1. The model was fit simultaneously to the position and pulse-height spectra from the *DXS* HISM region, and to the Wisconsin sky survey broad band data from the same region of the sky. By this procedure we demonstrate that it is possible to fit this data set with this response matrix and obtain a formally acceptable χ^2 . It also provides a mechanism for determining the intensities of the lines or line blends of the *DXS* spectrum.

In addition to 23 δ -function components in the 84 – 42 Å *DXS* first-order band, we included

two δ -function components in the $\frac{3}{4}$ keV band with freely floating energies, and the same absorbed power law component, $e^{-\sigma N_{\text{H}}} 11E^{-1.4}$, as in the thermal models discussed above (§4.2). These last three components supply the necessary flux in the higher energy 0.44–6 keV bands of the Wisconsin survey, but they provide less than 1.5% of the total flux in the *DXS* 84–42 Å band, and less than 7% of the flux in any bin in the *DXS* position spectrum. The resulting model fits the *DXS* HISM position spectrum with a $\chi^2_{\nu} = 0.77$ for $\nu = 33$ degrees of freedom. We then obtained 1- σ confidence limits for the intensity parameters in this model, using the `error` command of `xspec` version 10.0 with one parameter at a time free to vary. This follows the prescription of Lampton et al. (1976), investigating how the fit statistic varies as each line intensity parameter is varied in turn (holding the rest fixed). We take as 68.3% confidence limits those parameter values at which $\chi^2 = \chi^2_{\text{min}} + 1.00$.

In Table 3, we list the energies, wavelengths, intensities, and 1- σ confidence limits of the 23 lines in the 84–42 Å band. For completeness, we also include the two lines in the $\frac{3}{4}$ keV band, but without confidence limits. These two lines are present in the model only to provide X-ray flux in the 0.5–1 keV band. The solid line of Figure 16 shows the spectral fit in the 84–42 Å first-order band, and the dashed line shows the contribution of the higher energy photons to the spectrum. This is the contribution in second and third orders of the two high energy δ -function components and the absorbed power law continuum component. When this spectrum is used to calculate *ROSAT* count rates, the $\frac{1}{4}$ keV band rate is 3% lower than the observed rate, the $\frac{3}{4}$ keV band rate is $\sim 20\%$ higher than the observed rate, and the 1.5 keV band rate is $\sim 7\%$ lower than the observed rate.

The energies of these lines in the 84–42 Å band are somewhat arbitrary, and the spectrum of the diffuse soft X-ray background is certainly more complex than this simple model of 23 narrow emission lines, but this spectrum is the best description we have currently for the low Galactic latitude spectrum of the X-ray background in the 84–42 Å band.

5. Conclusions

We have presented spectra of the diffuse X-ray background in the 84–44 Å (148–284 eV) range, with spectral resolution $\lesssim 2.2$ Å (4 eV at 148 eV to 14 eV at 284 eV). The spectra show strong emission lines, implying a thermal origin for a significant fraction, if not all, of the diffuse background in the 84–44 Å (148–284 eV) range. As a very conservative absolute lower limit, lines contribute at least 32% of the measured flux. We also observed the Vela and Monogem Ring supernova remnants. The Monogem spectrum is similar in shape to the general diffuse X-ray background spectrum, but the Vela spectrum is noticeably different.

We find that the measured spectra are entirely consistent with previous broad-band measurements of the same part of the sky by the Wisconsin sounding rocket survey, *SAS 3*, *HEAO 1*, and *ROSAT*.

We find that the existing atomic emission data for this energy band are not adequate to fit the measured spectrum of the hot interstellar medium. We will continue to work with atomic physicists to calculate new theoretical spectra of relevant ions, and to benchmark these spectra against astrophysical spectra of bright, relatively well-understood stars that have been obtained with the *Chandra X-ray Observatory*. When we have adequate atomic data for the lines of important ions at temperatures of order 10^6 K, we can proceed to answer questions such as whether the gas is in coronal equilibrium, and if not, what kind of non-equilibrium ionization is required to fit the spectra, and whether the elemental abundances are solar or depleted. The young, hot Vela supernova remnant is likely to exhibit non-equilibrium ionization. However, it remains to be seen whether this is also true of the older Monogem Ring remnant or the diffuse background. When good single-ion spectra are available, we can set upper limits to the emission measure of each ion $E_{m,ion} = \int n_{ion}n_e dl$ by requiring that the theoretical spectrum for each ion not exceed our observed spectrum at any wavelength. These constraints can then be compared with detections or upper limits of other instruments in other wavelength bands, and with models.

It is with great pleasure that we acknowledge much work contributed by the Space Flight Hardware Group at the Space Science and Engineering Center of the University of Wisconsin–Madison, especially Robert Paulos, Fred Best, Gene Buchholtz, Dean Dionesotes, Nikola Ciganovich, Michael Dean, Timothy Dirx, Robert Herbsleb, William Hibbard, W. Warren Miller, Scott Mindock, Mark Mulligan, Brian Paul, Dave Petre, Evan Richards, Jerry Sitzman, John Short, Mark Werner, and W. Walter Wolf.

We thank Kurt Jaehnig, who built the flight proportional counters, and several generations of other scientists, postdocs, graduate students, and undergraduate students in the Space Physics Laboratory of the University of Wisconsin–Madison, especially Jeff Bloch, Richard J. Borke, David N. Burrows, Jiahong Zhang, Mike Juda, Julie Mills, Anisong Pathamavong, Mark Skinner, and Steve Snowden.

We are pleased to acknowledge help with quick-look data analysis from Keith Jahoda, Rich Kelley, Alan Smale, Carolyn Stahle, and Andy Szymkowiak of the Goddard Space Flight Center Laboratory for High Energy Astrophysics, and we thank Duane Liedahl for providing his atomic physics calculations in advance of publication.

We thank the referee, Steve Snowden, for the many helpful suggestions arising from his thorough reading of the manuscript.

This work has been supported under NASA contract NAS5-26078 and grants NAG5-3080, NAG5-3524 and NAG5-629 to the University of Wisconsin–Madison. RJE acknowledges support from NASA contracts NAS8-40224 and NAS8-39073 with the Smithsonian Astrophysical Observatory.

REFERENCES

- Acton, L. W., Bruner, M. E., Brown, W. A., Fawcett, B. C., Schweizer, W., & Speer, R. J. 1985, *ApJ*, 291, 865
- Anders, E. & Grevesse, N. 1989, *Geochim. Cosmochim. Acta*, 53, 197
- Arnaud, K. 1996, in ASP Conf. Ser. 101, *Astronomical Data Analysis Software and Systems V*, ed. G. Jacoby & J. Barnes (San Francisco: ASP), 17
- Bastin, G. F. & Heijligers, H. J. M. 1992, *Microbeam Anal.*, 1, 61
- Bloch, J. J. 1988, PhD thesis, University of Wisconsin, Madison
- Bloch, J. J., Jahoda, K., Juda, M., McCammon, D., Sanders, W. T., & Snowden, S. L. 1986, *ApJ*, 308, L59
- Bloch, J. J., Priedhorsky, W. C., & Smith, B. W. 1990, in IAU colloquium 115, *High Resolution X-ray Spectroscopy of Cosmic Plasmas*, ed. P. Gorenstein & M. Zombeck (Cambridge, UK: Cambridge University Press), 160
- Borken, R. J. & Kraushaar, W. L. 1976, *Space Science and Instrumentation*, 2, 277
- Bowyer, C. S., Field, G. B., & Mack, J. E. 1968, *Nature*, 217, 32
- Breitschwerdt, D. & Schmutzler, T. 1994, *Nature*, 371, 774
- Brickhouse, N. S., Dupree, A. K., Edgar, R. J., Liedahl, D. A., Drake, S. A., White, N. E., & Singh, K. P. 2000, *ApJ*, 530, 387
- Bunner, A. N., Coleman, P. L., Kraushaar, W. L., McCammon, D., Palmieri, T. M., Shilepsky, A., & Ulmer, M. 1969, *Nature*, 223, 1222
- Burrows, D. N. 1982, PhD thesis, University of Wisconsin-Madison
- Burrows, D. N. & Mendenhall, J. A. 1991, *Nature*, 351, 629
- Burstein, P., Borken, R. J., Kraushaar, W. L., & Sanders, W. T. 1977, *ApJ*, 213, 405
- Cox, D. P. & Reynolds, R. J. 1987, *ARA&A*, 25, 303
- Cox, D. P. & Smith, B. W. 1974, *ApJ*, 189, L105
- Doschek, G. A. & Cowan, R. D. 1984, *ApJS*, 56, 67
- Dwek, E. 1987, *ApJ*, 322, 817
- Edgar, R. J. & Cox, D. P. 1993, *ApJ*, 413, 190

- Edwards, B. C. 1990, PhD thesis, University of Wisconsin-Madison
- Garmire, G., Nousek, J. A., Apparao, K. M. V., Burrows, D. N., Fink, R. L., & Kraft, R. P. 1992, *ApJ*, 399, 694
- Henke, B. L., Lee, P., Tanaka, T. J., Shimabukuro, R. L., & Fujikawa, B. K. 1982, *Atomic Data and Nuclear Data Tables*, 27, 1
- Henry, R. C., Fritz, G., Meekins, J. F., Friedman, H., & Byram, E. T. 1968, *ApJ*, 153, 11
- Holliday, J. E. 1967, *The Norelco Reporter*, XIV, 84
- Jahoda, K. & McCammon, D. 1988, *Nucl. Instrum. Methods Phys. Res., Sect. A*, A272, 800
- Jelinsky, P., Vallergera, J. V., & Edelstein, J. 1995, *ApJ*, 442, 653
- Juda, M., Bloch, J. J., Edwards, B. C., McCammon, D., Sanders, W. T., Snowden, S. L., & Zhang, J. 1991, *ApJ*, 367, 182
- Kaastra, J. 1992, *An X-Ray Spectral Code for Optically Thin Plasmas*, Tech. Rep. 2.0, SRON-Leiden
- Kelly, R. L. 1987, *J. Phys. and Chem. Ref. Data*, 16, 1
- Klapisch, M. 1971, *Comput. Phys. Commun.*, 2, 239
- Kuntz, K. D. & Snowden, S. L. 2000, *ApJ*, 543, 195
- Lampton, M., Margon, B., & Bowyer, S. 1976, *ApJ*, 208, 177
- Liedahl, D. 1999, *Phys. Scr*, T83, 110
- Liedahl, D. A., Osterheld, A. L., & Goldstein, W. H. 1995, *ApJ*, 438, L115
- Malinovsky, L. & Heroux, M. 1973, *ApJ*, 181, 1009
- Marshall, F. J. & Clark, G. W. 1984, *ApJ*, 287, 633
- McCammon, D., Burrows, D. N., Sanders, W. T., & Kraushaar, W. L. 1983, *ApJ*, 269, 107
- Mewe, R., Gronenschild, E. H. B. M., & van den Oord, G. H. J. 1985, *A&AS*, 62, 197
- Mewe, R., Kaastra, J. S., & Liedahl, D. A. 1995, *Legacy*, 6, 16
- Mewe, R., Lemen, J. R., & van den Oord, G. H. J. 1986, *A&AS*, 65, 511
- Morgenthaler, J. P. 1998, PhD thesis, University of Wisconsin-Madison
- Morrison, R. & McCammon, D. 1983, *ApJ*, 270, 119

- Raymond, J. C. & Smith, B. W. 1977, *ApJS*, 35, 419
- Sanders, W. T., Edgar, R. J., Juda, M., Kraushaar, W. L., McCammon, D., Snowden, S. L., Zhang, J., & Skinner, M. A. 1992, *Proc. SPIE*, 1743, 60
- Sanders, W. T., Edgar, R. J., Juda, M., Kraushaar, W. L., McCammon, D., Snowden, S. L., Zhang, J., Skinner, M. A., Jahoda, J., Kelley, R., Smale, A., Stahle, C., & Szymkowiak, A. 1993, *Proc. SPIE*, 2006, 221
- Sfeir, D. M., Lallement, R., Crifo, F., & Welsh, B. Y. 1999, *A&A*, 346, 785
- Skinner, H. W. B. 1940, *Proc. R. Soc. London, Ser. A*, 239, 95
- Smith, R. K. 1996, PhD thesis, University of Wisconsin-Madison
- Smith, R. K. & Cox, D. P. 2001, *ApJS*, submitted
- Smith, R. K., Krzewina, L. G., Cox, D. P., Edgar, R. J., & Miller, W. W. 1996, *ApJ*, 473, 864
- Snowden, S. L. 2001, in *The Century of Space Science*, ed. J. Bleeker, J. Geiss, & M. Huber (Dordrecht: Kluwer Academic Publishers), in press
- Snowden, S. L., Cox, D. P., McCammon, D., & Sanders, W. T. 1990, *ApJ*, 354, 211
- Snowden, S. L., Egger, R., Finkbeiner, D. P., Freyberg, M. J., & Plucinsky, P. P. 1998, *ApJ*, 493, 715
- Snowden, S. L., Egger, R., Freyberg, M. J., Mccammon, D., Plucinsky, P. P., Sanders, W. T., Schmitt, J. H. M. M., Truemper, J., & Voges, W. 1997, *ApJ*, 485, 125
- Snowden, S. L., Freyberg, M. J., Plucinsky, P. P., Schmitt, J. H. M. M., Trümper, J., Voges, W., Edgar, R. J., McCammon, D., & Sanders, W. T. 1995, *ApJ*, 454, 643
- Snowden, S. L., Mebold, U., Hirth, W., & Herbstmeier, U. and Schmitt, J. H. M. M. 1991, *Sci*, 252, 1529
- Welsh, B. Y., Crifo, F., & Lallement, R. 1998, *A&A*, 333, 101
- Welsh, B. Y., Sfeir, D. M., Sirk, M. M., & Lallement, R. 1999, *A&A*, 352, 308
- Williamson, F. O., Sanders, W. T., Kraushaar, W. L., McCammon, D., Borken, R., & Bunner, A. 1974, *ApJ*, 193, L133

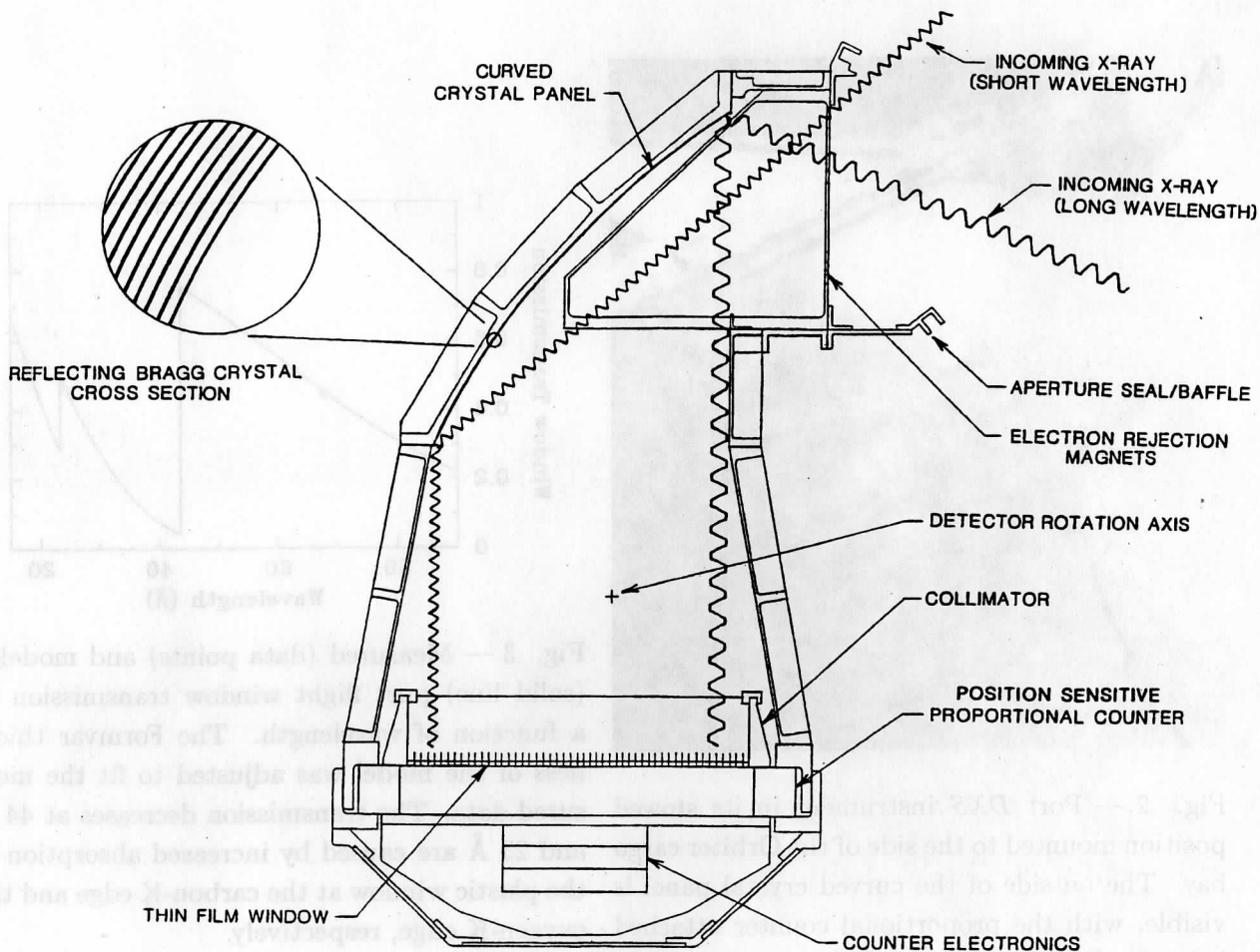


Fig. 1.— Cross-sectional view of a *DXS* detector showing photon paths and some of the detector's major parts. The X-ray reflecting crystal panel is made of 200 layers of lead stearate.

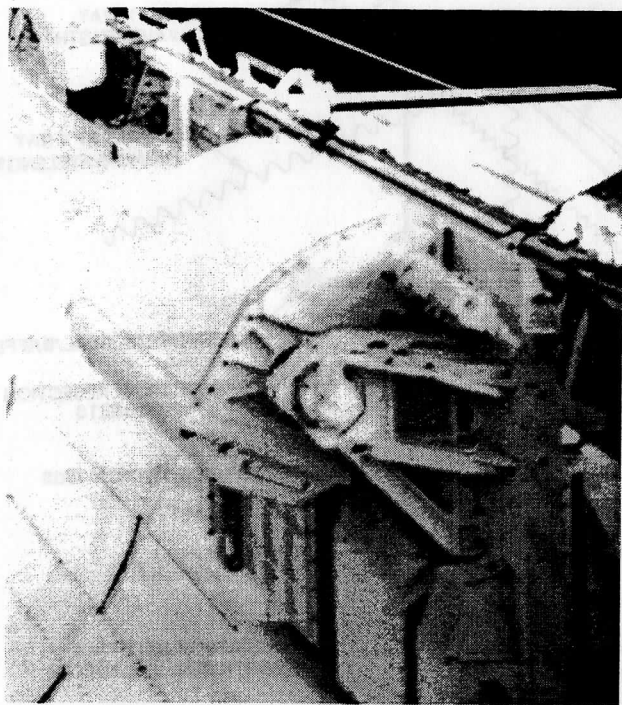


Fig. 2.— Port *DXS* instrument in its stowed position mounted to the side of the Orbiter cargo bay. The outside of the curved crystal panel is visible, with the proportional counter attached below it. The Orbiter port wing is visible in the background.

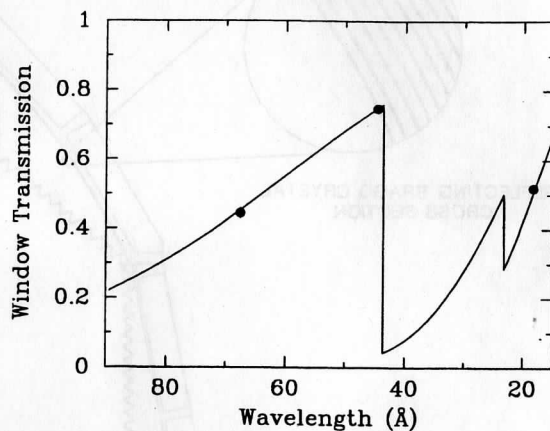


Fig. 3.— Measured (data points) and modeled (solid line) port flight window transmission as a function of wavelength. The Formvar thickness of the model was adjusted to fit the measured data. The transmission decreases at 44 Å and 23 Å are caused by increased absorption of the plastic window at the carbon-K edge and the oxygen-K edge, respectively.

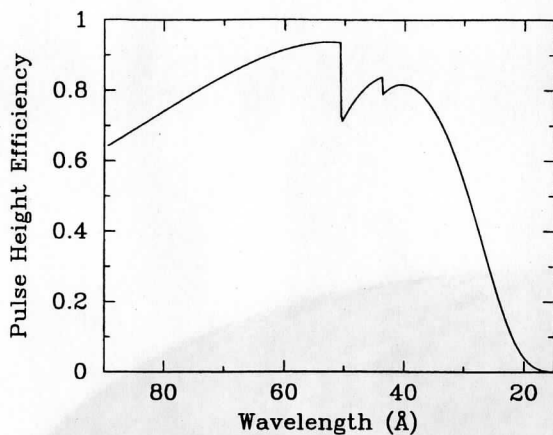


Fig. 4.— Port proportional counter pulse-height detection efficiency resulting from the pulse-height limits used for the analysis of the flight data. The efficiency decreases at 51 Å and at 44 Å are caused by changes in the pulse height distributions at the argon-L edge and the carbon-K edge, respectively, of the absorbing P-10 gas.

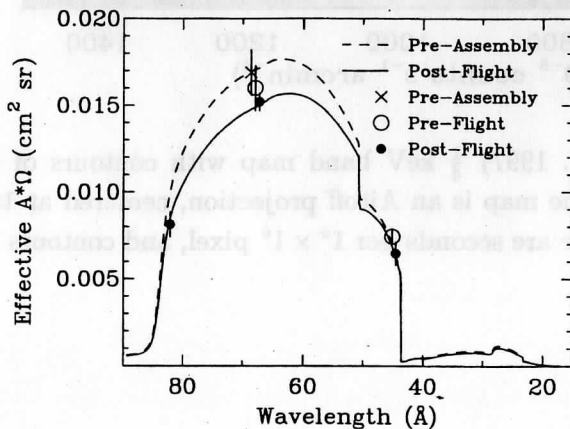


Fig. 5.— *DXS* port instrument $A\Omega$ measurements (data points) and model $A\Omega$ functions (lines).

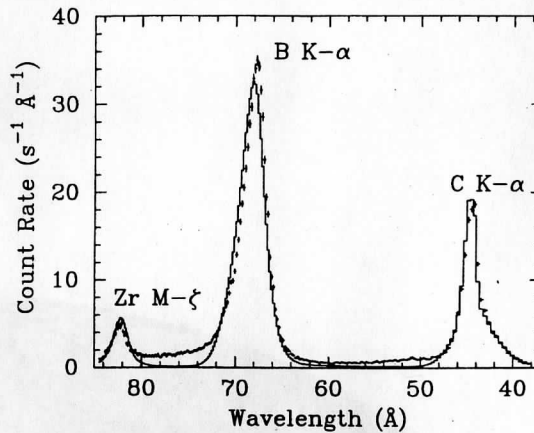


Fig. 6.— Spectral model comparisons (solid line) with three *DXS* post-flight calibration spectra (data points with error bars). The zirconium M- ζ input model function is a 151-eV delta function. The carbon K- α and boron K- α input functions are the unshifted spectra from Holliday (1967). The Holliday boron line profile appears to be broader than the boron source used in the *DXS* calibration.

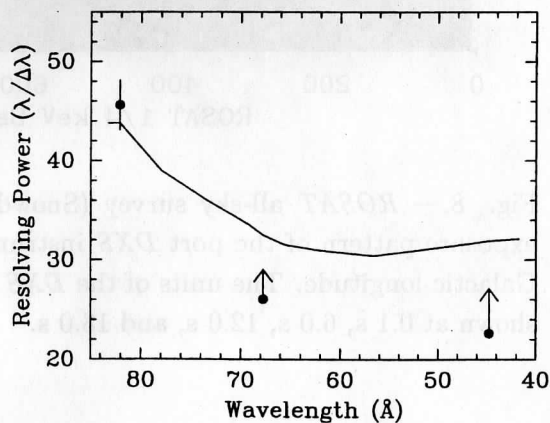


Fig. 7.— Calculated resolving power $\lambda/\Delta\lambda$ (FWHM) with measured points. The boron (67.6 Å) and carbon (44.8 Å) points are shown as lower limits, because the lines are clearly resolved by the instrument.

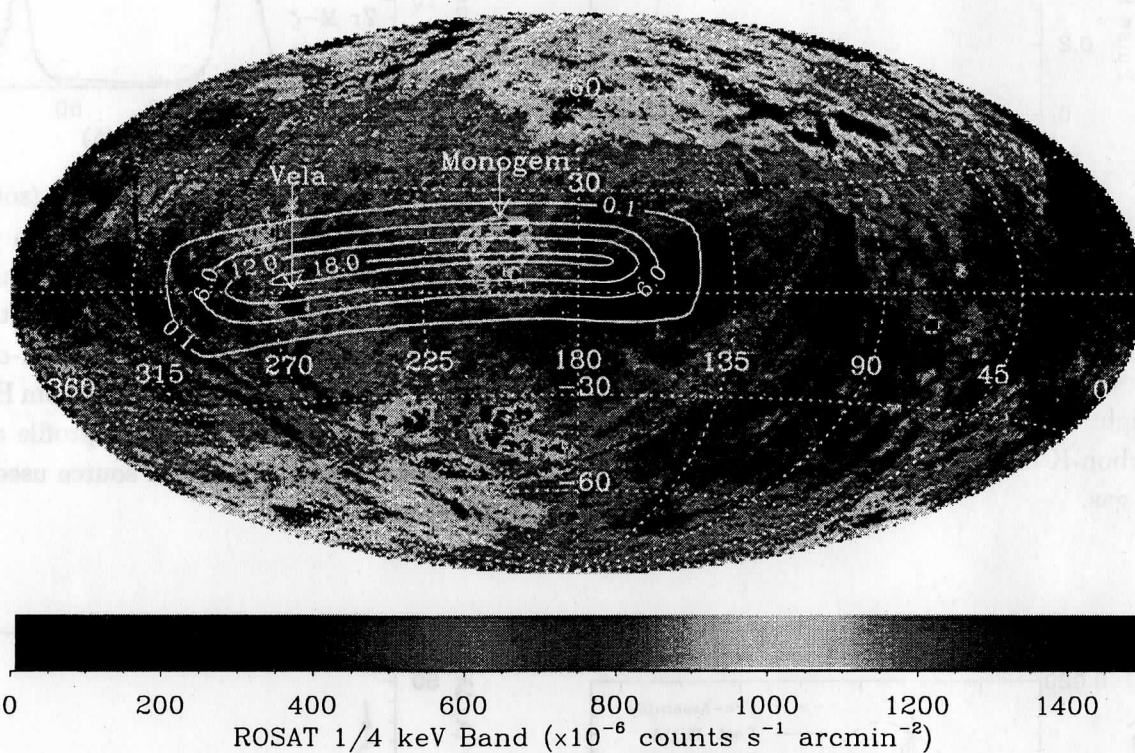


Fig. 8.— *ROSAT* all-sky survey (Snowden et al. 1997) $\frac{1}{4}$ keV band map with contours of the exposure pattern of the port *DXS* instrument. The map is an Aitoff projection, centered at 180° Galactic longitude. The units of the *DXS* exposure are seconds per $1^\circ \times 1^\circ$ pixel, and contours are shown at 0.1 s, 6.0 s, 12.0 s, and 18.0 s.

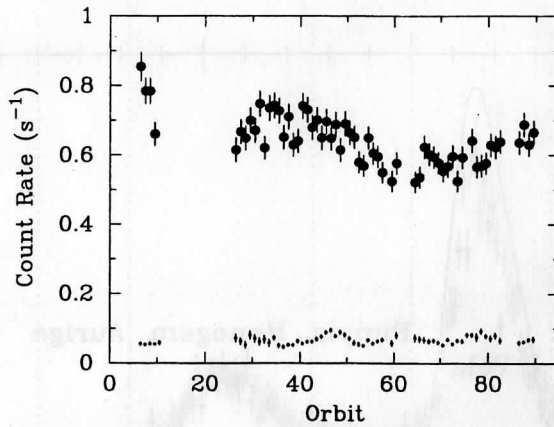


Fig. 9.— Time history of the total count rate, including background, in the port instrument (upper set of points). The instrument background rate, which was measured when the instrument was stowed, is shown separately by the lower set of points, and averages 0.068 s^{-1} ($1.6 \times 10^{-4} \text{ s}^{-1} \text{ cm}^{-2} \text{ keV}^{-1}$). Each orbit is approximately 91 minutes.

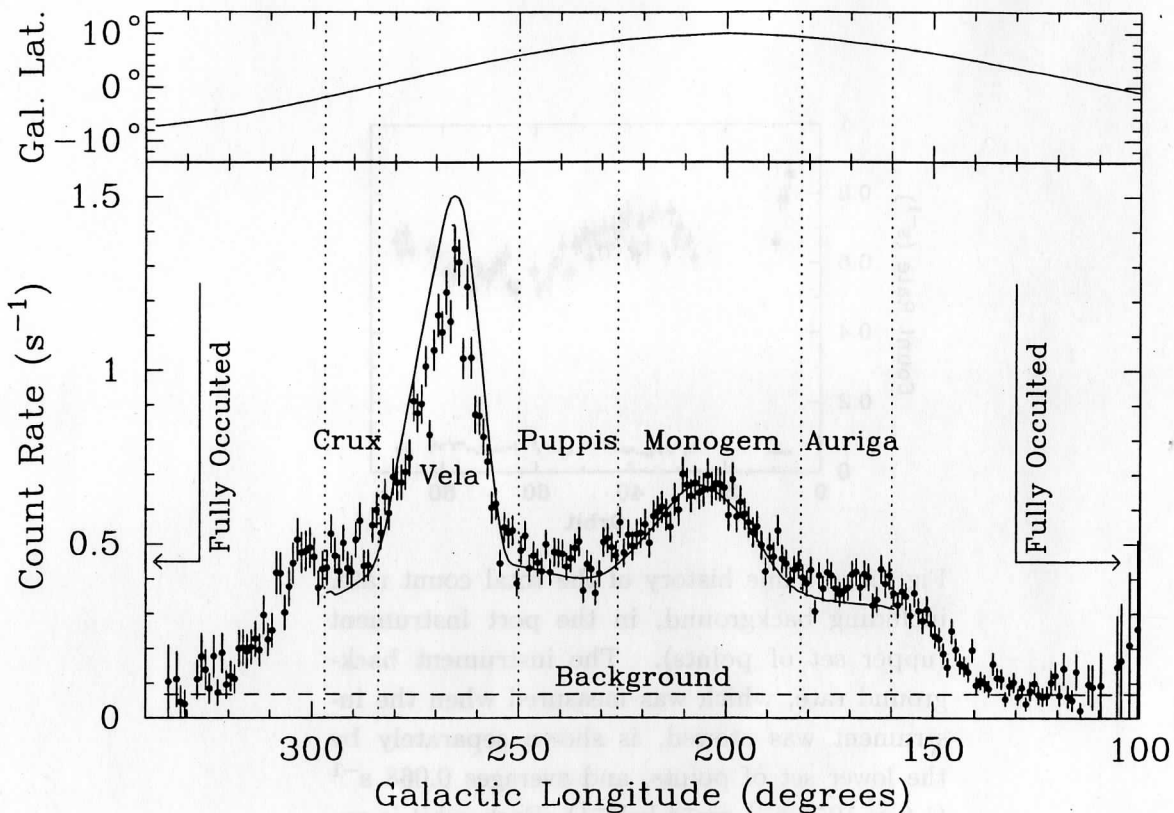


Fig. 10.— The effective count rate measured in the port *DXS* instrument as a function of Galactic longitude in one-degree bins. Instrument background is included, and the background rate inferred from instrument-closed measurements is indicated by the dashed line. The solid line is a prediction of the *DXS* count rate based on the *ROSAT* $\frac{1}{4}$ keV band map (Snowden et al. 1995). The vertical dotted lines indicate the boundaries of the five regions selected for spectral extraction. Spectral coverage is incomplete for $l > 271^\circ$ and $l < 175^\circ$. The upper plot gives the Galactic latitude of the center of the field of view.

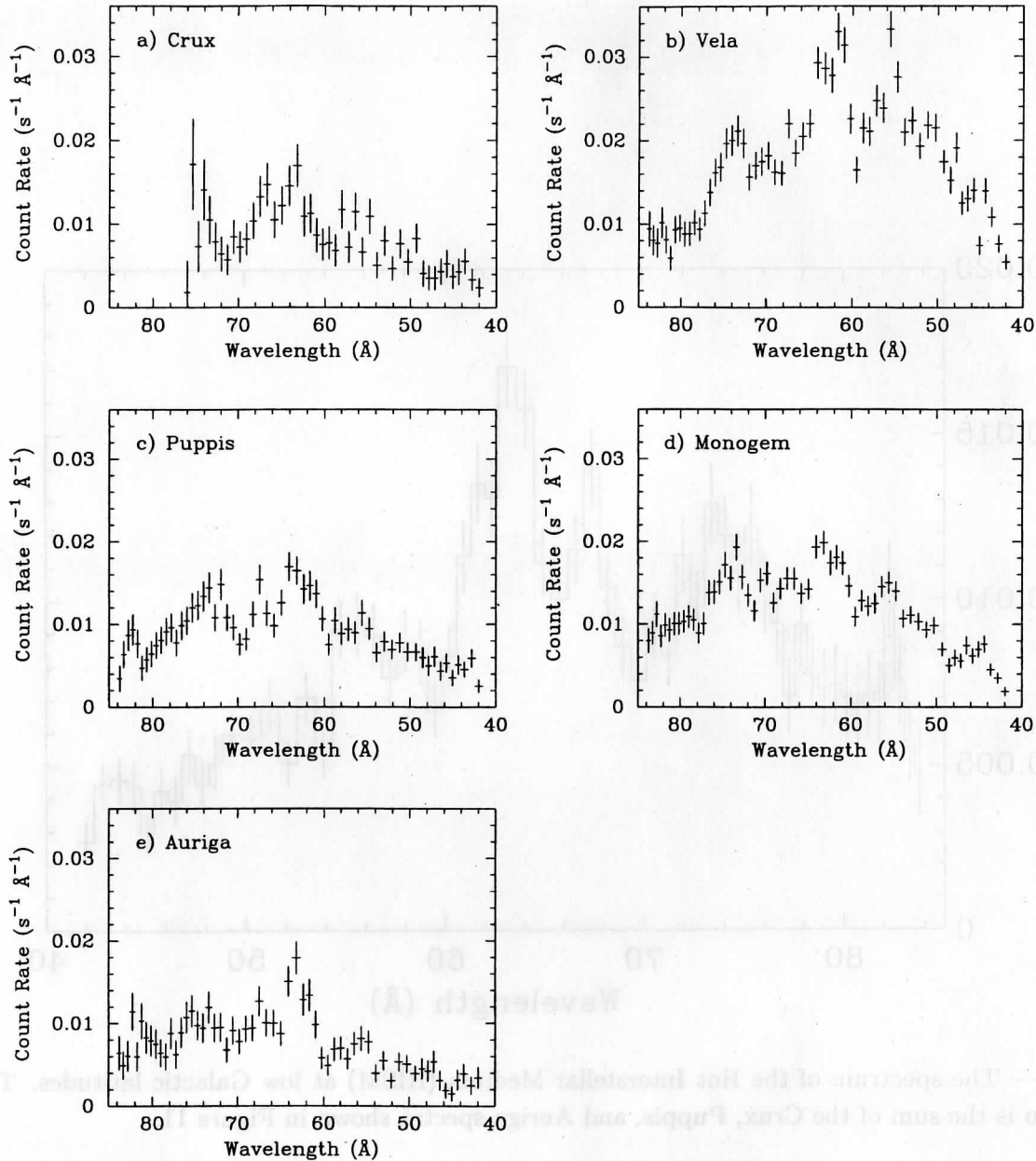


Fig. 11.— a) – e) The *DXS* spectra from the five regions of the sky defined in Figure 10. The Crux region was not observed by the port instrument at long wavelengths because the instrument was not rotated far enough to obtain that spectral coverage. The Vela and Auriga spectra have slightly reduced exposure at the longest and shortest wavelengths, respectively, for the same reason.

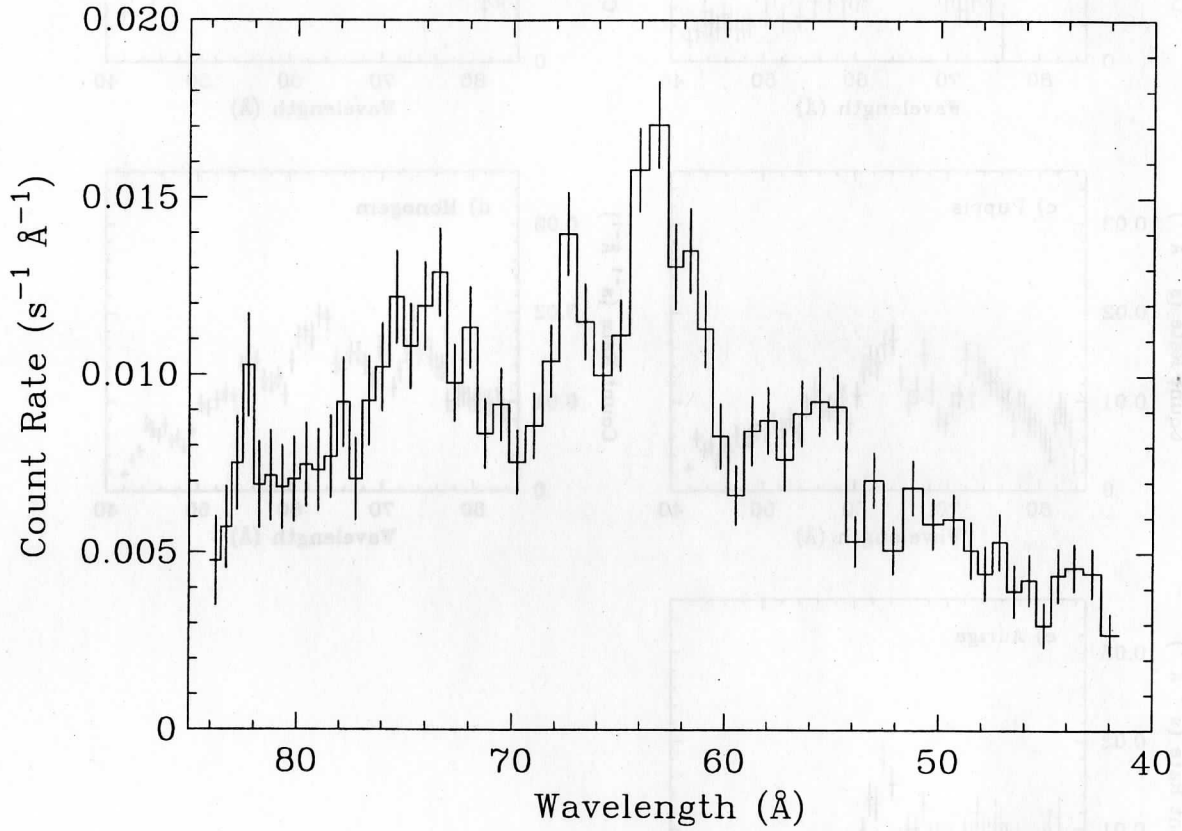


Fig. 12.— The spectrum of the Hot Interstellar Medium (HISM) at low Galactic latitudes. This spectrum is the sum of the Crux, Puppis, and Auriga spectra shown in Figure 11.

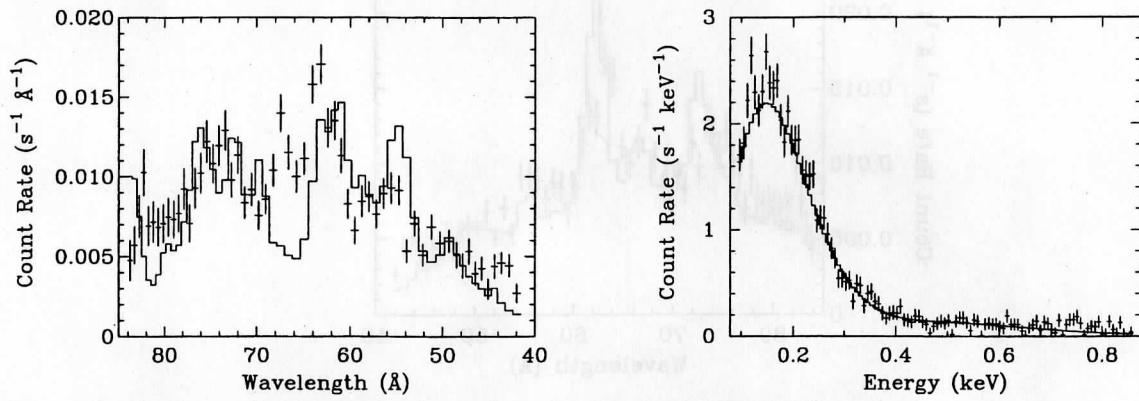


Fig. 13.— *DXS* HISM dispersed spectrum (left) and pulse-height spectrum (right) fit by the solar abundance RS model described by equation (1). Non-X-ray background has been subtracted from each spectrum.

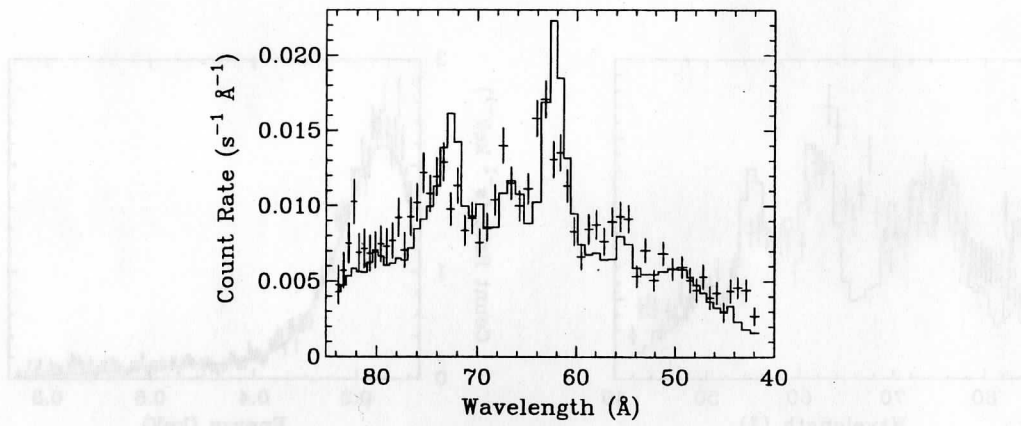


Fig. 14.— *DXS* HISM spectrum fit by the variable abundance MEKAL model described by equation (1) with individually adjustable abundances for Mg, Si, and Fe. The pulse-height spectral fit is similar to that of Figure 13.

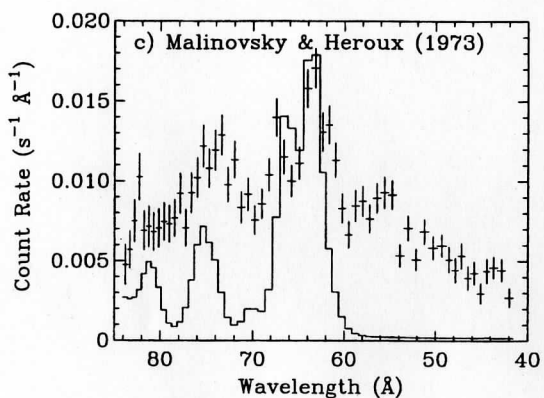
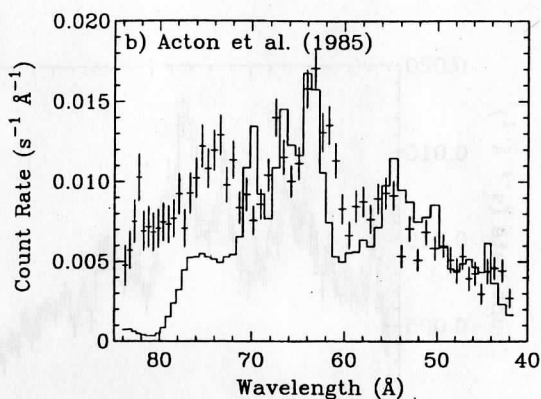
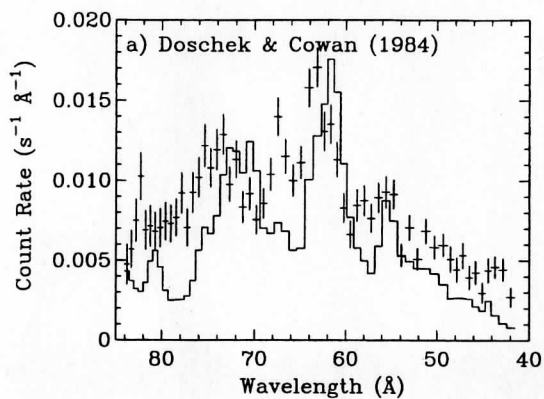


Fig. 15.— *DXS* HISM region spectrum (data points) compared to solar spectra (solid lines) of (a) Doschek & Cowan (1984), (b) Acton et al. (1985), and (c) Malinovsky & Heroux (1973).

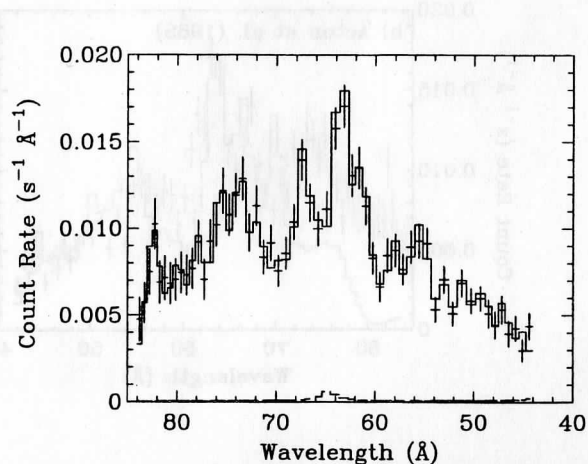


Fig. 16.— *DXS* HISM spectrum fit with δ functions. The *DXS* pulse-height distribution and the Wisconsin sky survey broad band count rates were fit simultaneously. There are 23 δ -function lines in the 84 – 44 Å band with energies chosen by eye, two δ -function lines in the $\frac{3}{4}$ keV band with best-fit energies, and an absorbed power law component. The contribution of the $\frac{3}{4}$ keV δ -function lines and the power law to the 84 – 42 Å band is shown by the dashed line at the bottom.

Table 1. Alpha-Particle-Excited X-ray Calibration Sources

| Target | Line | E (eV) | λ (Å) | Pre-Assembly | Pre-flight | Post-flight |
|-----------|-------------|--------|---------------|--------------|------------|-------------|
| Zirconium | M- ζ | 151 | 82.1 | no | no | yes |
| Boron | K- α | 183 | 67.6 | yes | yes | yes |
| Carbon | K- α | 277 | 44.8 | no | yes | yes |

Table 2. Equilibrium plasma emission model fit parameters

| model ^a | kT_1^b | $E_{m,1}^c$ | kT_2^b | $E_{m,2}^c$ | χ_ν^2 | Mg ^d | Si ^d | Fe ^d |
|--------------------|----------|-------------|----------|-------------|--------------|-----------------|-----------------|-----------------|
| RS/solar | 0.094 | 2.93 | 0.156 | 17.6 | 4.01 | 1.0 | 1.0 | 1.0 |
| RS/MgSiFe | 0.089 | 3.78 | 0.189 | 12.1 | 3.97 | ... | 0.63 | ... |
| RS/variable | 0.103 | 3.40 | 0.203 | 10.1 | 2.98 | 2.8 | 0.27 | 0.72 |
| MEKAL/solar | 0.112 | 3.51 | 0.231 | 9.11 | 3.75 | 1.0 | 1.0 | 1.0 |
| MEKAL/MgSiFe | 0.118 | 8.59 | 0.366 | 4.02 | 3.08 | ... | 0.29 | ... |
| MEKAL/variable | 0.115 | 9.10 | 0.332 | 4.56 | 2.71 | 0.24 | 0.13 | 0.34 |

^aEquilibrium plasma emission models (see text)

^bkeV

^c $10^{-3} \text{ cm}^{-6} \text{ pc}$

^dElemental abundances relative to solar (Anders & Grevesse 1989)

Table 3. Line Strengths^a

| E (eV) | λ (Å) | intensity ^{b,c} |
|----------|---------------|--------------------------|
| 150.5 | 82.39 | 2.42 ± 0.22 |
| 153.1 | 80.99 | 0.42 ± 0.19 |
| 155.3 | 79.84 | 1.25 ± 0.17 |
| 159.3 | 77.83 | 1.48 ± 0.16 |
| 164.0 | 75.60 | 1.88 ± 0.16 |
| 168.5 | 73.58 | 1.89 ± 0.15 |
| 172.8 | 71.75 | 1.27 ± 0.13 |
| 176.8 | 70.13 | 0.72 ± 0.12 |
| 183.0 | 67.75 | 0.55 ± 0.13 |
| 179.3 | 69.15 | 0.44 ± 0.11 |
| 184.0 | 67.39 | 1.45 ± 0.14 |
| 188.4 | 65.81 | 0.84 ± 0.13 |
| 195.0 | 63.58 | 2.75 ± 0.15 |
| 202.0 | 61.38 | 1.50 ± 0.13 |
| 206.6 | 60.01 | 0.32 ± 0.11 |
| 213.4 | 58.10 | 1.17 ± 0.12 |
| 220.5 | 56.23 | 0.63 ± 0.12 |
| 224.2 | 55.30 | 1.10 ± 0.12 |
| 233.9 | 53.01 | 0.76 ± 0.11 |
| 243.0 | 51.02 | 1.02 ± 0.12 |
| 253.0 | 49.01 | 1.14 ± 0.16 |
| 264.0 | 46.97 | 1.02 ± 0.17 |
| 264.0 | 46.97 | 1.02 ± 0.17 |
| 569.0 | 21.79 | 13.46^d |
| 842.7 | 14.71 | 6.00^d |

^aFrom the multiple δ -function fit to the HISM spectrum.

^bphoton $s^{-1} cm^{-2} sr^{-1}$

^c68.3% (1σ) confidence limits

^dsee text